Development of calibration and noise characterization methods for a CMB telescope, GroundBIRD, using its commissioning observation data

Department of Physics, Graduate School of Science,
Kyoto University

Yoshinori Sueno

February 6, 2024

Abstract

Cosmic Microwave Background radiation (CMB) is a promising probe for understanding the history of the universe. Precise measurements of the anisotropy in the CMB polarization at larger than degree-scale provide information about the primordial gravitational waves which are evidence for the cosmic inflation. The CMB polarization at more than 10° scale also contains information about the optical depth (τ) at the reionization era. The optical depth is important for determining the sum of the neutrino masses precisely.

GroundBIRD is a ground-based CMB experiment. The GroundBIRD telescope rotates continuously at a speed of 20 revolutions per minute. This rapid scan modulation mitigates effects of atmospheric fluctuation and allows us to measure the CMB at a large angular scale. We aim for the above science targets based on this unique observation strategy.

In data analysis, we reconstruct CMB maps from time-ordered data which are responses from each focal plane detector as a function of time. Information about pointing (i.e., line of sight) and polarization angle (i.e., antenna orientation at the sky coordinate) is necessary for the map making. Therefore, their calibrations are important. The data contains various noises as well as the CMB. We make efforts to filter out the noise effects. The filtering process also tends to smear the CMB anisotropy in general. It is important to develop good filtering methods which keep efficiency for the CMB whereas significantly suppressing the noise effects. We developed calibration and filtering methods based on our commissioning observation data taken from February to April in 2022.

We used the Moon observation data for the pointing calibration. Comparing to planets such as Jupiter, frequent change of observation every month with high signal-to-noise ratio is the biggest advantage of the Moon. We established the calibration method using the Moon although its visible size is larger than that of planets. We successfully achieved a pointing accuracy of $3.3'$, which competes with past achievements by using the planets. For the polarization angle calibration, we proposed a new calibration method based on the pointing information. We obtained a rotation angle of the detector wafer from the calibrated pointing. Using this angle, we calibrated the polarization angles of each detector on the wafer. Achieved precision is 0.27°, which also competes with past achievements.

We developed our data analysis pipeline and characterized the noise. We adopted three processes for suppressing the noise effects. Using the analysis pipeline, we confirmed these processes maintain the efficiency for the CMB ($\geq 85\%$). Thus far, we have not achieved sufficient noise suppression yet. Additional development for the filtering is necessary, which is a future work. We also evaluated the scientific impacts with respect to our calibrations. For the optical depth, the calibration uncertainty corresponds to uncertainty of 1%. For the primordial gravitational waves, the impact of the calibration uncertainty is at most 1/30 of the current upper limit for the tensor-to-scalar ratio ($r < 0.032$).

In 2023 May, we upgraded our focal plane detectors, and started scientific observations. The new detectors were optimized based on knowledge from the commissioning data. Our forecast for the τ measurement is also based on the commissioning. In this thesis, we newly established calibration methods which can be applied to the new detectors too. We confirmed our prospects to achieve the sensitivity of $\sigma(\tau) = 0.01$ using three years data.

Acknowledgements

My research life for 5 years at Kyoto University was really fun and fulfilling. A lot of people supported my research. I would like to express my appreciation to all those people.

I would like to express my sincere gratitude to my supervisor, Prof. Osamu Tajima. He gave me an opportunity to do very exciting research topics such as the GroundBIRD experiment. He always watched over my research. At the turning point, he gave me a lot of insightful advice and guided me to the correct way. I learned various things from him: how to think and proceed with the research, how to present my research, etc... Without his support for my thesis and application, especially JSPS fellowship, my research life as well as my private life would not become such fruitful. I am convinced that my choice to join the High Energy Physics group and work under his supervision is not a mistake. And I hope to be a scientist like him someday. I would like to express my gratitude to my another supervisor, Dr. Junya Suzuki. When I faced some problems, he taught me everything smartly and essentially. I was always surprised by his insights. I would like to progress the research with like logical thinking and management like him someday. A special gratitude I give to Dr. Shunsuke Honda who led the GroundBIRD experiment during my research life. He hugely supported my research in Tenerife as well as at Kyoto University. He always kept me positive and gave me useful advice. During my stay at Tenerife, he and his wife (Mizuki-san) greatly supported me. Visiting the CTA in La Palmas is one of the greatest memories in my Tenerife life.

I would like to express my appreciation to the GroundBIRD collaborator. I am deeply grateful to Dr. Hiroki Kutsuma. He taught me a lot of things about superconducting detectors. He also progressed the GroundBIRD experiment with his grant. I could not have started my research in this thesis without his work. I also thank Mr. Tanaka and Ms. Tsujii for their cooperation to my work. There is no graduate student except them in GroundBIRD. Working and talking with them was really fun. I would like to express my gratitude to Prof. Chiko Ohtani, Prof. Makoto Hattori, Prof. Ricardo Tanausú Génova-Santos, and Prof. Eunil Won. They warmly watched over my research and gave me a lot of faithful comments. Their management and grant for the GroundBIRD experiment allowed me to do my research. I would also like to express gratitude to Dr. Shugo Oguri, Dr. Taketo Nagasaki, and Dr. Kyungmin Lee for their excellent work on the GroundBIRD experiment.

I would like to express my appreciation to Dr. Kenichi Karatsu, Prof. J.J.A. Baselmans, and other people supported to fabrication of the GroundBIRD MKIDs in the Netherlands. My research is based on the MKID which is fabricated by them at SRON / TU Delft.

I would like to express my gratitude to members of the CMB group at Kyoto University. Dr. Shunsuke Adachi always helped my research at Kyoto University. His research attitude is one of the ideal attitudes for me. Dr. Satoru Takakura taught me a lot of things about CMB analysis. I also thank Dr. Yudai Seino, Nakata-kun, Takeuchi-kun, Muto-kun, Kasai-kun, Hanimura-kun, Hoshino-kun, Kataoka-kun. I really enjoyed the discussion in the seminar as well as in the weekly meeting.

I would like to express gratitude to all the past and current members of the Kyoto

High Energy Physics group. Prof. Tsuyoshi Nakaya helped with my paperwork and gave me useful comments on my paper review. Dr. Tatsuya Kikawa gave me advice to write this thesis. Sekiguchi-san, Sasaki-san, and Tsuzuki-san always help me with office work. I thank Sugashima-kun, Tsujikawa-kun, Feng-kun, and Yohan as my colleagues in the same school year. I really enjoyed talking at the drinking party as well as in the laboratory. I would like to express my appreciation to Prof. Enoto Teruaki for providing me useful comments on my paper review.

This work is supported by JSPS KAKENHI under grant numbers JP21J20290, JP21H04485, JP20KK0065 and JP21H04485, JSPS Core-to-Core Program number JPJSCCA20200003, and JSPS Bilateral Program numbers JPJSBP120219943 and JPJSBP120239919.

I would like to acknowledge "ESA and the Planck Collaboration" for their great plots which are used in chapter 1. Some of the results in this paper have been derived using the healpy and HEALPix packages.

I also appreciate my family, Mai Sueno, Yuito Sueno, Shuji Sueno, Yukiko Sueno, Toshinori Sueno, Akinori Sueno, Fukiko Sueno, Hisami Tachibana. They always watched over me warmly and supported me a lot. Yuito made me very happy with your smile every day. I hope you grow up to be healthy and happy. Mai encouraged and believed me every day. She was also responsible for most of the childcare. I could not have completed this thesis without your huge support.

Contents

Chapter 1

Introduction

1.1 History of the universe

1.1.1 The Big Bang theory

How was the Universe created? This is the most curious question for us. The Big Bang theory provides us with a definitive answer to how the early universe evolved. The idea of the Big Bang theory was introduced by Georges Lemaître in 1927 [1]. Discoveries in the early 20th century supported the Big Bang theory, and it became a solid theory for describing the early universe.

One of the discoveries is the expansion of the universe. In 1929 Edwin Hubble found that galaxies farther from the Milky Way were moving away at faster velocity, which is known as Hubble's low [2]. This law is interpreted as evidence of the expanding universe and it supports the Big Bang theory. Another evidence is the Big Bang Nucleosynthesis (BBN), a phenomenon to generate light nuclei, which occurred during the first several minutes of the universe [3]. BBN predicts the abundances of the light elements: D, ^{3}He, ^{4}He, and ^{7}Li. The predictions are consistent with the primordial abundances inferred from the observational data [4]. The most conclusive evidence for the Big Bang theory is the existence of uniform background radiation, cosmic microwave background (CMB), caused by the initial state of high density and temperature.

1.1.2 Cosmic Microwave Background radiation

Arno Penzias and Robert Wilson happened to find the CMB as an irreducible radiation noise with cryogenic microwave receivers for radio astronomy observations in 1965 [5]. The CMB discovered was uniform across the sky. However, anisotropy of the CMB was thought to exist in order to enable the formation of large-scale structures. In addition, whether the CMB follows the blackbody spectrum or not was an important topic.

In 1989, COsmic Background Explorer (COBE) satellite was launched to observe CMB more precisely. Three types of detectors were implemented on the COBE satellite: Far-Infrared Absolute Spectrometer (FIRAS), Differential Microwave Radiometer (DMR), and Diffuse Infrared Background Experiment (DIRBE). FIRAS precisely measured the CMB spectrum in the frequency region of 30–660 GHz. The obtained spectrum is well consistent

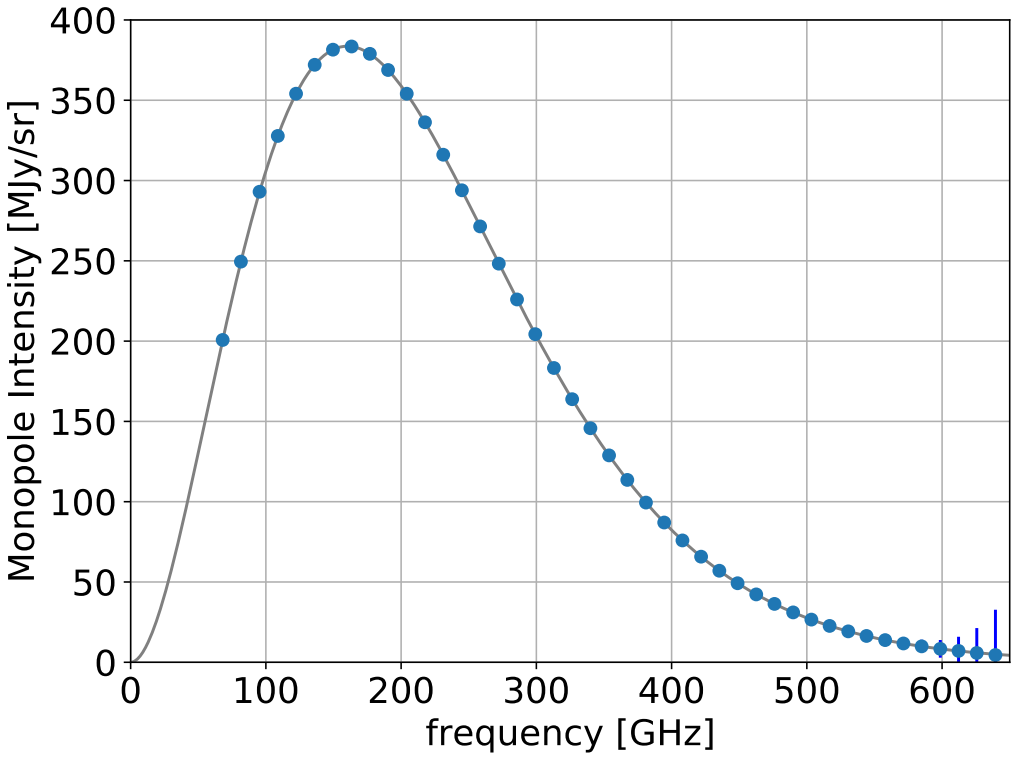

Figure 1.1: Monopole intensity spectra of CMB measured by FIRAS. The blue dots are data with 100 times uncertainties. The solid is the theoretical spectra of the Planck low of blackbody radiation with a temperature of 2.725 K.

with the Planck low, formula of blackbody radiation,

$$B_\nu(\nu, T) = \frac{2h\nu^3}{c^2} \frac{1}{\exp\left(\frac{h\nu}{k_B T} - 1\right)}, \tag{1.1}$$

where ν is a frequency, T is a thermodynamics temperature, c is the speed of light, h is the Planck constant, k_B is the Boltzmann constant. This is the evidence that CMB was in thermodynamic equilibrium in the early universe, strongly supporting the Big Bang theory. FIRAS determined the temperature of 2.725 ± 0.002 K (95 % confidence interval) from the CMB spectrum as shown in Figure 1.1 [6].

Another important discovery by COBE is anisotropy of the CMB, which was measured by DMR. The magnitude of the fluctuation is five orders of magnitude fainter than the average value of the CMB temperature. Multi-frequency observation with DMR (i.e., 31.4, 53, and 90 GHz) allowed to remove galactic signals (hereafter foregrounds) as well as the CMB monopole and dipole. The discovered anisotropy also provides knowledge about the initial conditions of the formation of large-scale structures in the universe. The discoveries by COBE established a new experimental research field in cosmology focusing on CMB measurements. The "Lambda-Cold Dark Matter" cosmological model called ΛCDM is the standard model to describe the evolution of the universe. This model predicts the CMB anisotropy at a small angular scale. Because the angular resolution of COBE is

large (i.e. 7°), measurements with higher angular resolution were needed to determine the cosmological parameters of the ΛCDM model.

In 1998, the BOOMERanG (balloon observations of millimetric extragalactic radiation and geomagnetics) experiment observed the CMB anisotropy at a small angular scale. BOOMERanG observed with three frequency bands (90, 150, 220 GHz) at altitude of ~ 38 km by a balloon. Its angular resolution is $\sim 0.4°$, which is 20 times better than that of COBE. The obtained CMB anisotropy at a small scale was consistent with the ΛCDM model in a flat universe[7]. It was the first experiment to observe the CMB anisotropy at a small scale and demonstrate the flat universe.

Wilkinson Microwave Anisotropy Probe (WMAP) satellite was launched in 2001. WMAP observed the CMB as well as foregrounds at the full sky with five frequency bands from 23 to 94 GHz. WMAP also had a higher resolution ($\sim 0.3°$) than COBE ($\sim 10°$). WMAP determined that the universe is consistent with being flat, with higher sensitivity than that of BOOMERanG. The ΛCDM has been constructed with the WMAP results.

The Planck satellite was launched in 2009. The angular resolution of Planck is 2.5 times better than that of WMAP. Planck observed with nine separate frequency bands from 30 GHz to 857 GHz for intensity. Seven bands of them (30 GHz to 353 GHz) are polarization sensitive. Placnk produced a lot of precise scientific results. Some of these are still the most precise results. Intensity and polarization maps of the CMB taken by Planck are shown in Figure 1.2 and Figure 1.3, respectively.

In addition to the satellite observation, ground-based CMB telescopes also observed the CMB more precisely [9, 10, 11, 12, 13, 14, 15]. An advantage of ground-based telescopes is that it is easy to upgrade instruments. A lot of detectors can be installed on the large focal plane structure. BICEP array [16] and Simons Observatory[17] are going to achieve more precise observation than Planck. CMB-S4 (Stage 4) [18], the next generation of ground-based CMB experiment, will take over these experiments for ultimately precise observation. The next generation of CMB satellite, LiteBIRD, plans to be launched in the early 2030s to observe the full sky with separated frequency bands from 34 to 448 GHz with higher sensitivity and resolution than Planck [19].

1.1.3 ΛCDM model and Cosmic inflation

ΛCDM model, a standard cosmological model, describes the evolution of the universe. This model comprises six cosmological parameters which have to be measured. The latest measurements are summarized in Table 1.1.

The current universe consists of three components: Dark energy (or the cosmological constant), Cold Dark Matter, and ordinally matter (e.g., Hydrogen, Helium). Each energy budget is approximately 70%, 25%, and 5%, respectively. This is mainly determined by the measurements of CMB anisotropy. To understand the evolution of the universe, we have to identify time evolution of each component in the history of the universe.

In a homogeneous and isotropic universe, Robertson-Walker (RW) metric, a metric of

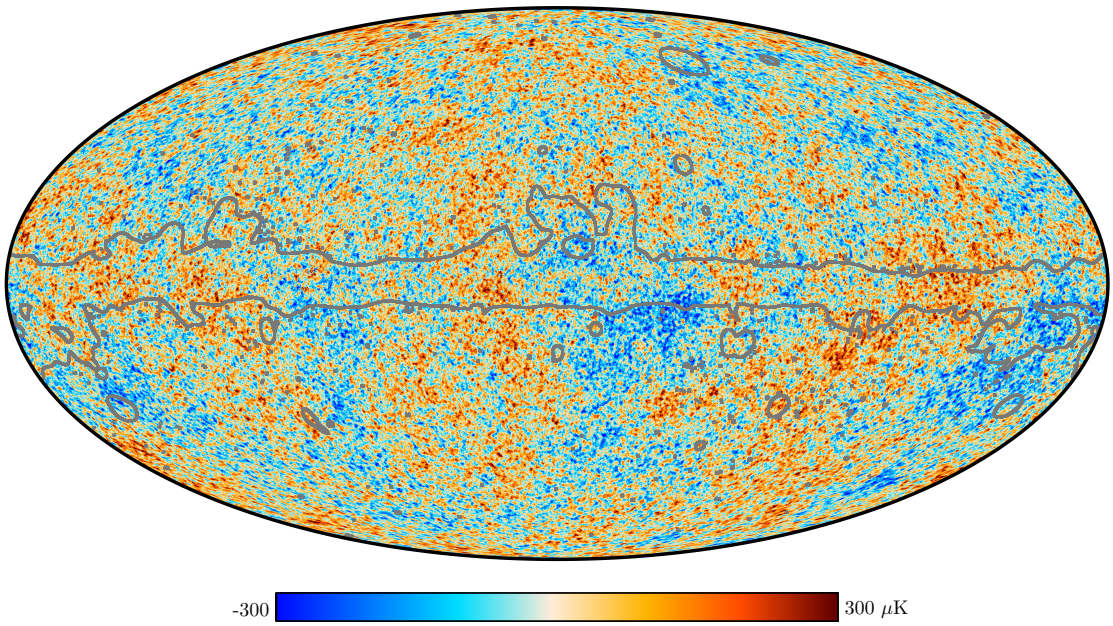

Figure 1.2: Map of temperature anisotropy of the CMB measured by Planck [8]. A resolution of this map is $0.5'$. The color shows the intensity of the temperature anisotropy. The gray line shows the extent of the confidence mask. In this plot, the Galactic foregrounds were already subtracted based on multi-frequency observations. The CMB temperature has anisotropy of ~ 100 μK.

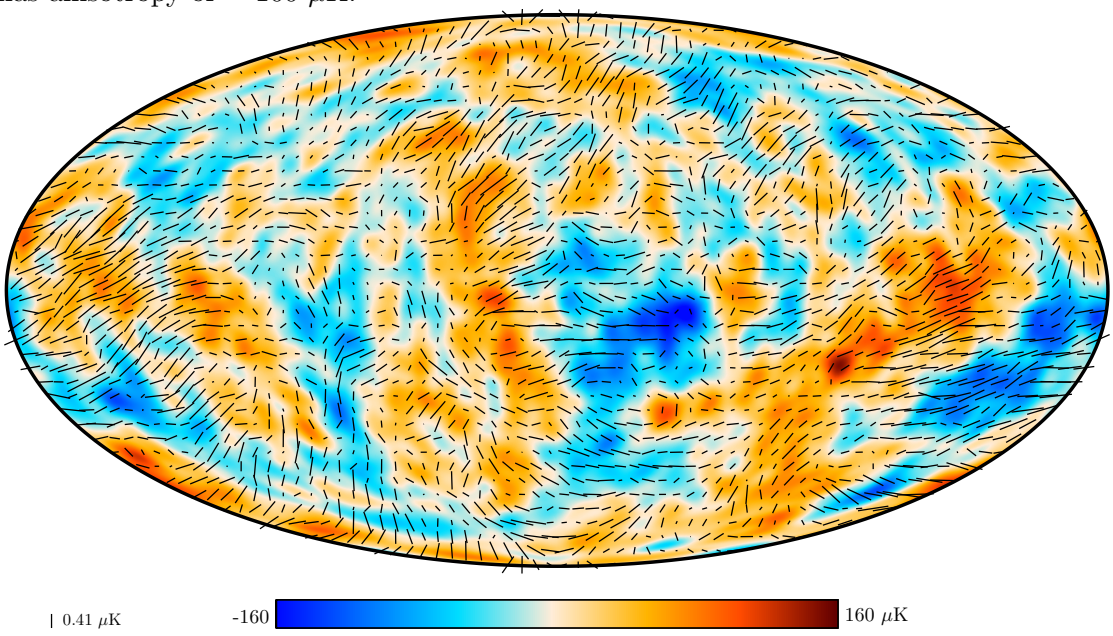

Figure 1.3: This plot shows polarization intensities which are overlaid on the smoothed temperature map at 5°. The direction and length of rods show the polarization direction and amplitude of polarized CMB, respectively. They are Planck results [8]. The intensity of the polarized signal ($\approx \mu$K) is approximately two orders of magnitude lower than that of the temperature anisotropy.

Table 1.1: The latest cosmological parameters of ΛCDM model from Plank [8]. These results are determined in combination with CMB lensing reconstruction and baryon acoustic oscillations (BAO) measurements

$\Omega_b h^2$ (Baryon density)	0.02242 ± 0.00014
$\Omega_c h^2$ (Cold Dark Matter density)	0.11933 ± 0.00091
$100\theta_{MC}$ (angular scale of sound horizon at last scattering)	1.04101 ± 0.00029
τ (Optical depth at reionization era)	0.0561 ± 0.0071
$ln(10^{10}A_s)$ (Amplitude of scalar primordial fluctuation)	3.047 ± 0.014
n_s (index of scalar primordial fluctuation)	0.9665 ± 0.0038

the spacetime, is written[1] in a polar coordinate system.

$$ds^2 = -dt^2 + a^2(t)\left[\frac{dr^2}{1-Kr^2} + r^2(d\theta^2 + \sin^2\theta d\phi^2)\right], \tag{1.2}$$

where $a(t)$ is a scale factor that describes the expansion scale of the universe, K is a spatial curvature.

The metric and a distribution of matter follow the Einstein's equation,

$$G^{\nu}_{\ \mu} = 8\pi G T^{\nu}_{\ \mu} - \Lambda\delta^{\nu}_{\ \mu}, \tag{1.3}$$

where $G^{\nu}_{\ \mu}$ is the Einstein tensor, G is the Newtonian constant of gravitation, and Λ is the cosmological constant. $T^{\nu}_{\ \mu}$ is the energy-momentum tensor, which is described as,

$$T^{\nu}_{\ \mu} = \begin{pmatrix} -\rho & 0 & 0 & 0 \\ 0 & P & 0 & 0 \\ 0 & 0 & P & 0 \\ 0 & 0 & 0 & P \end{pmatrix}, \tag{1.4}$$

where ρ is an energy density and P is a pressure by assuming a perfect fluid.

By combining the RW metric and the Einstein's equation, we can derive the Friedmann equations as follows,

$$\left(\frac{\dot{a}}{a}\right)^2 = \frac{8\pi G}{3}\rho - \frac{K}{a^2} + \frac{\Lambda}{3}, \tag{1.5}$$

$$\frac{\ddot{a}}{a} = -\frac{4\pi G}{3}(3P+\rho) + \frac{\Lambda}{3}. \tag{1.6}$$

These equations describe the expansion of the universe.

We can also derive the energy conservation from Eq. 1.5 and Eq. 1.6,

$$\frac{d}{dt}(\rho a^3) = -P\frac{d}{dt}a^3. \tag{1.7}$$

From this equation, we found the time evolution of the scale factor depends on the energy density and the pressure at the moment. The relation between the energy density and the pressure is written as the equation of state ($w \equiv P/\rho$). It depends on the energy component. We can classify the energy components into three components (i.e., Radiation,

[1] In this paper, we basically use the system of natural units.

Matter, and Dark energy) with respect to the equation of state. The time dependence of the scale factor for each energy component is listed in Table 1.2. $d(t)$ is a distance where the photon can be correlated (also called as "horizon"). It is defined as follows,

$$d(t) = a(t) \int_0^t \frac{1}{a(t')} dt'. \tag{1.8}$$

$d(t)/a(t)$ is a comoving distance which is the independent distance with respect to the expansion of the universe.

Table 1.2: Time dependences of the scale factor for each energy component: Radiation, Matter, and Dark energy. w is equation of state, the ρ is the energy density, $a(t)$ is the scale factor, $d(t)$ is the distance (horizon)、$d(t)/a(t)$ is the comoving distance (horizon).

Energy component	w	ρ	$a(t)$	$d(t)$	$d(t)/a(t)$
Radiation	1/3	a^{-4}	$t^{\frac{1}{2}}$	$2t$	$2t^{\frac{3}{2}}$
Matter	0	a^{-3}	$t^{\frac{2}{3}}$	$3t$	$3t^{\frac{5}{3}}$
Dark energy	-1	Constant	e^t	Constant	e^{-t}

One of the important points of their dependence is that the comoving distance became larger compared to the expansion rate of the universe when the universe is the radiation or the matter dominant era. This predicts the "Horizon Problem" which is described in section 1.2.4.

In the early universe, the radiation was the dominant component according to Table 1.2. In the radiation dominant era, photons and other particles were continuously scattering because the temperature and density were extremely high. As the universe expanded, its temperature gradually cooled down. Free electrons began to be captured by protons to form neutral hydrogen approximately 100,000 years after the Big Bang. At around 350,000 years after the Big Bang, the mean free path of photons and the expansion rate became equivalent. After that period, the photons were able to move freely without the scattering of free electrons. This process is called recombination, and we observe these photons as the CMB. The spherical shell at the recombination era is called as "last scattering surface". After the recombination, the CMB did not scatter until the age of reionization, which is described in section 1.4.1.

Although the ΛCDM model successfully explains the evolution of the early universe, there are still unexplained problems as described in section 1.2.4. A hypothesis of the inflationary universe, "Inflation", is the most influential hypothesis to solve the problems. The inflation theory predicts that specific and weak signal is imprinted on the CMB. Therefore, we can validate the inflation theory by precise measurements of the CMB.

1.2 Probing the universe by using CMB

Both of intensity and polarization of CMB anisotropies gave us a lot of information about the history of the universe. We can understand the different aspects of the universe from the intensity and polarization anisotropies because of the differences about their generation processes.

1.2.1 Power spectrum of CMB anisotropy

The anisotropy as shown in Figures 1.2 and 1.3 can be characterized by the spherical harmonics $Y_\ell^m(\hat{n})$.

$$\Delta T(\hat{n}) = \sum_{\ell=1}^{\infty} \sum_{m=-\ell}^{\ell} a_{\ell m} Y_\ell^m(\hat{n}), \tag{1.9}$$

where $\hat{n} \equiv (\sin\theta\cos\phi, \sin\theta\sin\phi, \cos\theta)$ is a unit vector of line-of-sight (called as pointing hereafter) from the observer, ℓ is a multipole of the spherical harmonics, and m is a magnetic quantum number ($-\ell \leq m \leq \ell$). The multipole ℓ represents the angular scale ($\delta\theta$) of the anisotropy. Their relationship is,

$$\delta\theta = 180^\circ/\ell. \tag{1.10}$$

Because a coefficient of $a_{\ell m}$ is a coordinate dependent variable, it is better to convert to a coordinate independent variable. A variance of the map is a coordinate independent variable. Therefore, the angular power spectrum is introduced as follows,

$$C_l \equiv \frac{1}{2l+1} \sum_{m=-\ell}^{\ell} a_{\ell m} a_{\ell m}^*. \tag{1.11}$$

Theoretical auto-correlated angular power spectra of TT, EE, and BB are shown in Figure 1.4. The TT power spectrum is an auto-correlation spectrum of the temperature map. On the other hand, EE, and BB power spectra are auto-correlation spectra for the polarization maps of E-modes (parity-even pattern) and B-modes (parity-odd pattern), respectively. These spectra are calculated with the best-fit parameters from Planck [21] by using camb [20] software.

1.2.2 Temperature anisotropy

The intensity anisotropy gives us cosmological parameters of the ΛCDM model as listed in Table 1.1.

At low multipole regions ($\ell \leq 20$), the TT power spectrum represents gravitational redshift at the last scattering surface called as Sachs-Wolfe effect. This is because primordial fluctuation generates difference of gravitational potential for each pointing at the last scattering surface. The amplitude (A_s) and the index of scalar primordial fluctuation (n_s) are also determined from these spectra.

On the other hand, at high multipole region ($\ell \geq 100$), the dumping structure in the TT power spectrum represents fluctuation between the CMB and the baryon before the recombination, which is called as Baryon acoustic oscillations. This spectrum depends on the distance which the acoustic waves could travel (i.e., the sound horizon), the energy density of Baryon and Cold Dark Matter as well as the optical depth. The lower optical depth increases the amplitude of the dump.

1.2.3 Polarization anisotropy

The polarized CMB was generated by Thomson scattering due to the quadrupole temperature anisotropy as explained in Figure 1.5. Polarization patterns can be divided into

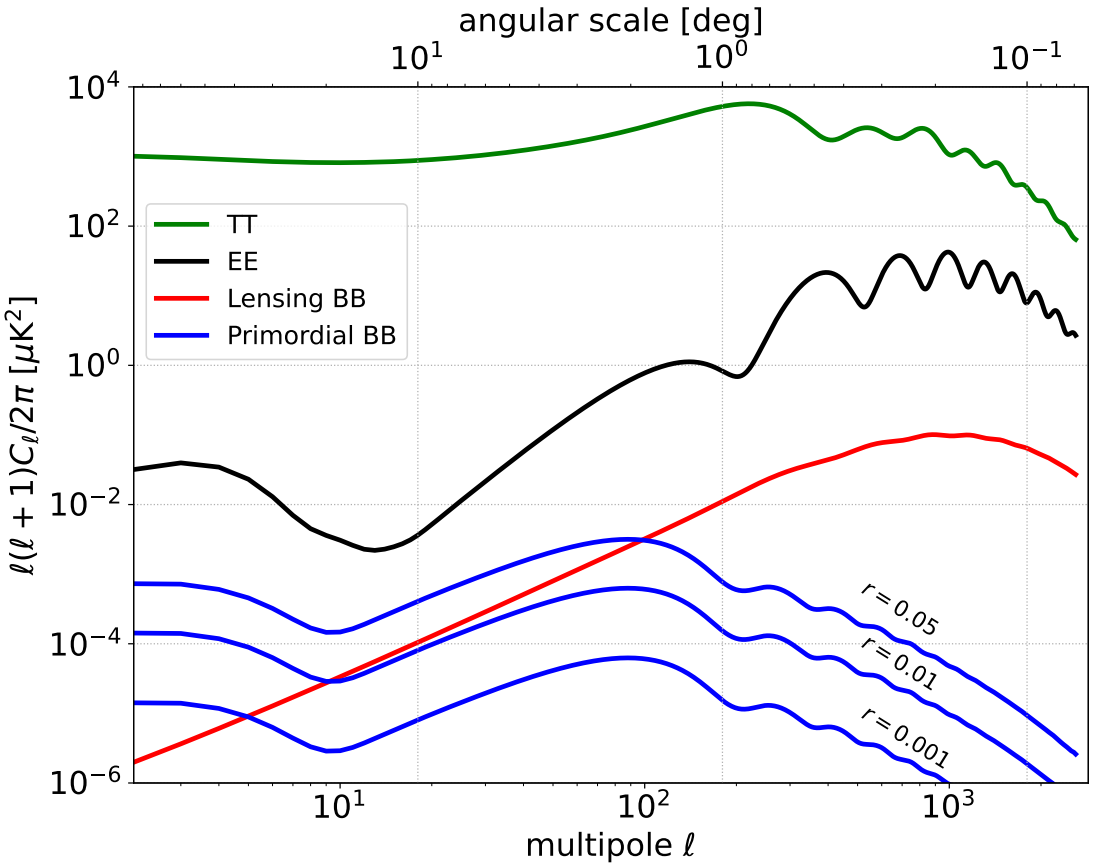

Figure 1.4: Theoretical power spectra for TT, EE, and BB originated from the lensing effect (lensing BB). These are calculated by camb [20] with best-fit parameters from Planck [22, 21]. Power spectra for BB originated from the primordial gravitational waves with the tensor-to-scalar ratio $r = [0.05, 0.01, 0.001]$. At higher multipole (i.e. small angular scale), the power spectra for EE and BB are sensitive to the gravitational lens effect of galaxy clusters. On the other hand, at lower multipole (i.e. large angular scale), the power spectra for EE and BB are sensitive to the primordial gravitational wave and optical depth at the reionization era.

two types: E-modes and B-modes as shown in Figure 1.6. A polarization direction of E-modes is parallel or perpendicular to a wave vector of fluctuation (k). On the other hand, a polarization direction of B-modes is tilted to the wave vector by $\pm 45^\circ$. Thus, E-modes are a parity even, while B-modes are parity odd. Both E-modes and B-modes are independent of coordinate systems. This is because both the wave vector and the polarization direction change if we change coordinate systems.

E-modes is mainly generated by the quadrupole temperature anisotropy as illustrated in Figure 1.5. There are two eras when the CMB was scattered by free electrons: the recombination era and the reionization era. The baryon acoustic oscillations in the recombination era generated an oscillation shape of EE power spectrum at high multipole regions. On the other hand, the Thomson scattering in the reionization era generated a bump of EE power spectrum at low multipole regions ($\ell \leq 20$).

B-modes can be generated from two origins: the gravitational lensing and a tensor

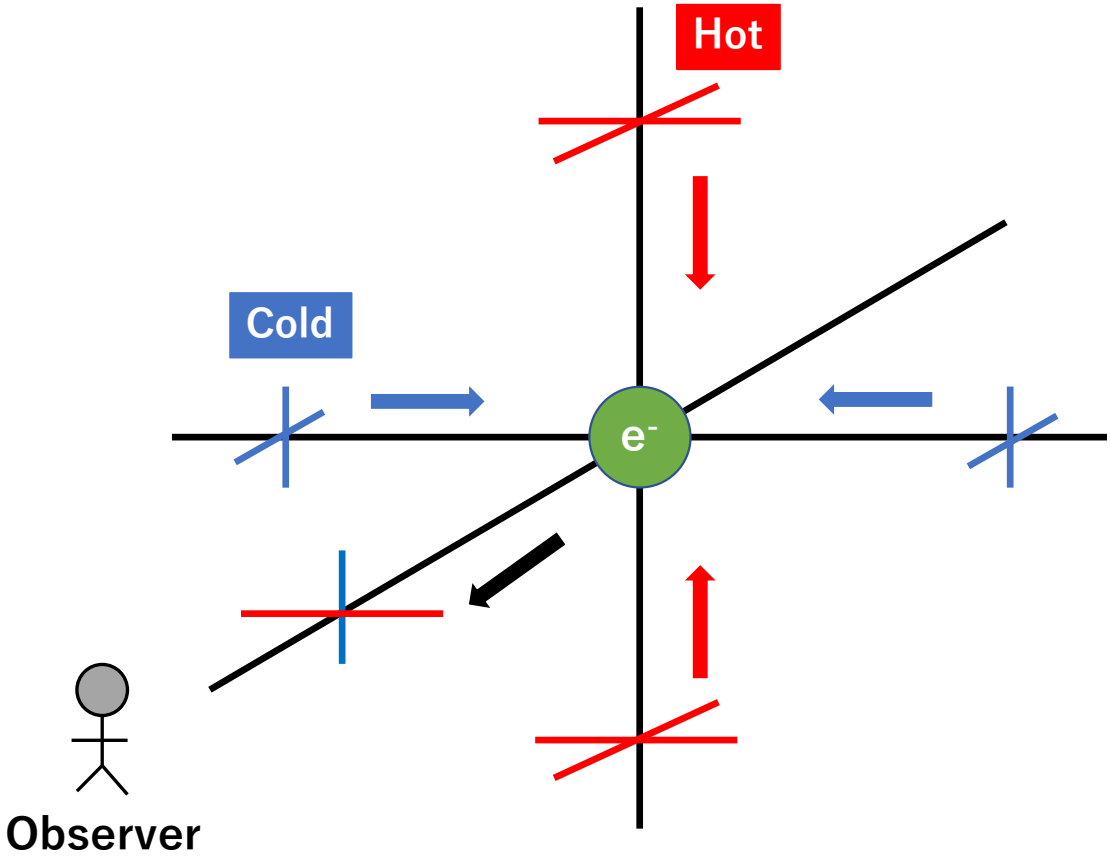

Figure 1.5: Principle of generating polarized CMB due to the quadrupole thermal anisotropy. The CMB has random polarization directions before scattering to free electrons. After scattering, the CMB only has a polarization direction perpendicular to the traveling direction before the scattering. Thus, if there is quadrupole thermal anisotropy around the free electron, scattered CMB by the electron is polarized along the direction to the cold region. This is because the intensity of CMB from the cold region is weaker than that from the hot region [23]

.

perturbation of the primordial gravitational waves. The gravitational lensing effect is caused by matter perturbations along the pointing to the last scattering surface. The gravitational potential distorts the polarization pattern of E-modes to that of B-modes. This is called as lensing B-modes. The gravitational potential depends on the structure formation. Lensing B-modes also depends on the sum of neutrino masses because it affects the structure formation. The tensor perturbation can generate B-modes. This is called as primordial B-modes. Its amplitude depends on the amplitude of the primordial gravitational wave. It is characterized by the tensor-to-scalar ratio r as shown by blue lines in Figure 1.4.

1.2.4 Remaining subjects

Although the ΛCDM model explains the evolution of the universe well, there are still unexplained phenomena.

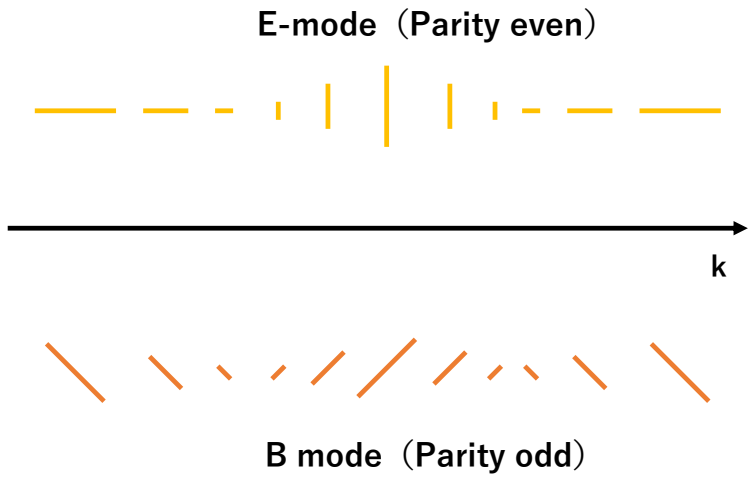

Figure 1.6: Examples of E-modes and B-modes. The direction and length of rods show a polarization direction and an amplitude of polarized CMB. E-modes whose polarization direction is perpendicular or parallel to a wave vector (k) is a parity even. On the other hand, B-modes whose polarization direction is tilted to the wave vector by 45° is a parity odd[22].

- Horizon Problem : Because the speed of light and the age of the universe are limited, a region where the CMB can be correlated with each other is limited. It corresponds to an angular scale of $\sim 2^\circ$ at the recombination era. Although there is no reason that the CMB is correlated outside that scale, the observed CMB has uniform temperature with an accuracy of 10^{-5} K everywhere. This is known as the horizon problem.

- Flatness Problem : By using the critical density ($\rho_c \equiv \frac{3H^2}{8\pi G}$) and the ratio of the critical density to the energy density ($\Omega \equiv \rho/\rho_c$), we can rewrite Eq. (1.5) at the early universe,

$$\frac{\Omega - 1}{\Omega} \approx \frac{K}{\rho a^2}. \tag{1.12}$$

  The current Ω value is consistent with one (i.e., the universe is spatially flat) as described in section 1.1.2. The right-hand side in Eq. (1.12) was small at the early universe because of $\rho \propto a^{-4}$ at the radiation dominant era. Thus, Ω needs to be quite close to one at the beginning of the universe. This situation cannot be realized from the Big Bang theory without parameter fine-tuning. This is called as the flatness problem.

1.3 Inflationary universe

A hypothesis of the inflationary universe called as “Inflation” is built to explain these problems [24, 25]. This hypothesis is that the universe underwent exponential expansion at the beginning of the universe. The exponential growth of the universe expands the length scale over which different regions can have correlations with each other. The CMB can be correlated with each other everywhere if the exponential growth is kept for sufficient time.

In addition, the universe became flat even if the universe was not flat at the beginning of the universe. The inflation can leave the quantum fluctuation of the inflaton as the primordial fluctuation. It is considered as a seed of the density fluctuation in the early universe. Therefore, the inflation is the most influential hypothesis at the current moment. An important predictor of the inflation is the existence of the primordial gravitational waves [26]. The primordial gravitational waves are predicted to generate weak B-modes in the CMB polarization [27, 28, 29, 30, 31, 32, 33].

1.3.1 Slow-roll inflation

The exponential expansion is realized under the constant expansion rate (i.e., Hubble parameter $H = \frac{\dot{a}}{a}$). The inflation is described as a real scalar field called as inflaton. Lagrangian density and Hamiltonian of the inflaton are written with its potential energy ($V(\phi)$) as follows,

$$\mathcal{L} = a(t)^3 \left[\frac{\dot{\phi}^2}{2} - V(\phi) \right], \tag{1.13}$$

$$\mathcal{H} = \frac{\dot{\phi}^2}{2} + V(\phi). \tag{1.14}$$

If the Euler-Lagrange equation is applied to this Lagrangian density, the equation of motion of the inflaton is obtained as follows,

$$\ddot{\phi} + 3H\dot{\phi} + V'(\phi) = 0, \tag{1.15}$$

where, $\dot{\phi} = \frac{d\phi}{dt}$、$V'(\phi) = \frac{dV}{d\phi}$.

Based on the Eq (1.7), Eq (1.14), and Eq (1.15), the energy density and the pressure of the inflaton in case of a perfect fluid are written as,

$$\rho_\phi = \frac{\dot{\phi}^2}{2} + V(\phi), \tag{1.16}$$

$$P_\phi = \frac{\dot{\phi}^2}{2} - V(\phi). \tag{1.17}$$

If the time derivative of the inflaton is much smaller than its potential energy (i.e., $\dot{\phi}^2 \ll V(\phi)$), the energy density is approximately the same as the pressure. This condition realizes the exponential expansion.

In particular, the exponential expansion can be kept for a long time if $\dot{\phi}^2 \ll V(\phi), \ddot{\phi} \ll 3H\dot{\phi}$. The inflation for a long time is required to solve the horizon problem and the flatness problem. This inflation is known as "slow-roll inflation". Figure 1.7 shows one of the examples of the potential energy in the slow-roll inflation model. The slow-roll inflation is one of the most simple models.

1.3.2 Imprint in the CMB anisotropy

The inflation generated two types of perturbations: scalar and tensor perturbations[2]. Their origin was quantum fluctuations. The scalar perturbation was caused by the fluctuation of the inflaton. Its amplitude depends on the energy scale and time derivative of the

[2]Vector perturbation can be eliminated by using Einstein constraint equations [34]

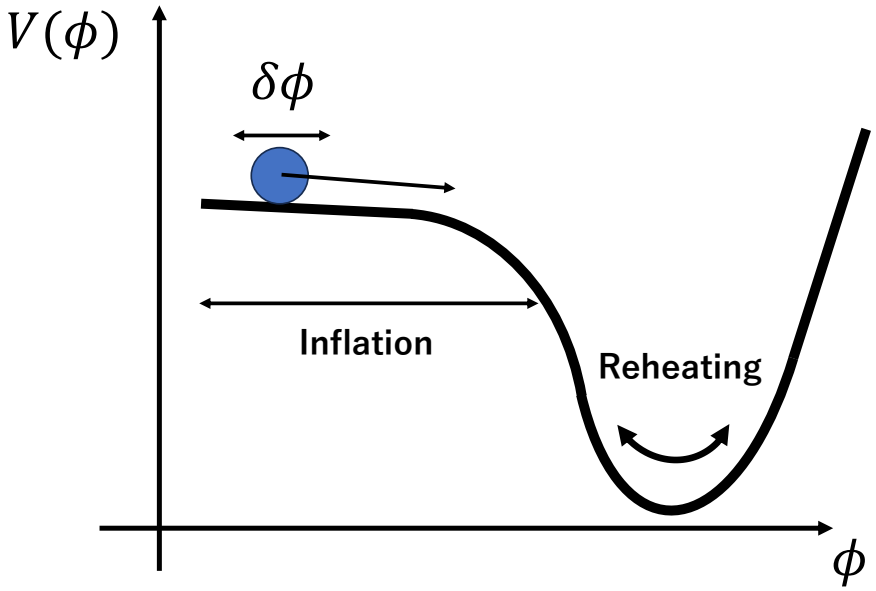

Figure 1.7: Example of the potential energy of the inflaton (real scaler field) in slow-roll inflation model. Inflation happened at the time when the potential energy ($V(\phi)$) was much lower than the kinetic energy of the inflaton ($\dot{\phi}/2$). The primordial gravitational waves were generated due to the fluctuation of the inflaton ($\delta\phi$). This fluctuation was created by quantum fluctuations. Reheating process converted the energy of the inflation to the universe after inflation.

inflaton. On the other hand, the tensor perturbation was caused by the fluctuation of the metric during the inflation. Compared to the scalar perturbation, its amplitude depends only on the energy scale of inflation.

Angular power spectra for the scalar perturbation (P_s) and the tensor perturbation (P_t) are characterized by following formulae [34],

$$P_s(k) = \frac{4\pi}{\epsilon M_p^2}\left(\frac{k}{2\pi a}\right)^2, \tag{1.18}$$

$$P_t(k) = \frac{64\pi}{M_p^2}\left(\frac{k}{2\pi a}\right)^2, \tag{1.19}$$

where M_p is the Planck mass ($M_p \equiv G^{-1/2} = 1.2209 \times 10^{19}$GeV), ϵ is a time derivative of the Hubble parameter divided by the square of it ($\epsilon \equiv -\frac{\dot{H}}{H^2}$).

The scalar power spectrum left an imprint mainly in the TT power spectrum. On the other hand, the tensor power spectrum left an imprint in the primordial BB power spectrum as well as the EE power spectrum. In particular, an amplitude of the primordial BB power spectrum is characterized by the tensor-to-scalar ratio ($r = \frac{P_t}{P_s}$). One of the milestones of the measurement of r is $r \sim 0.002$ known as "Lyth bound" which is the expected minimum value of a simple inflation model.

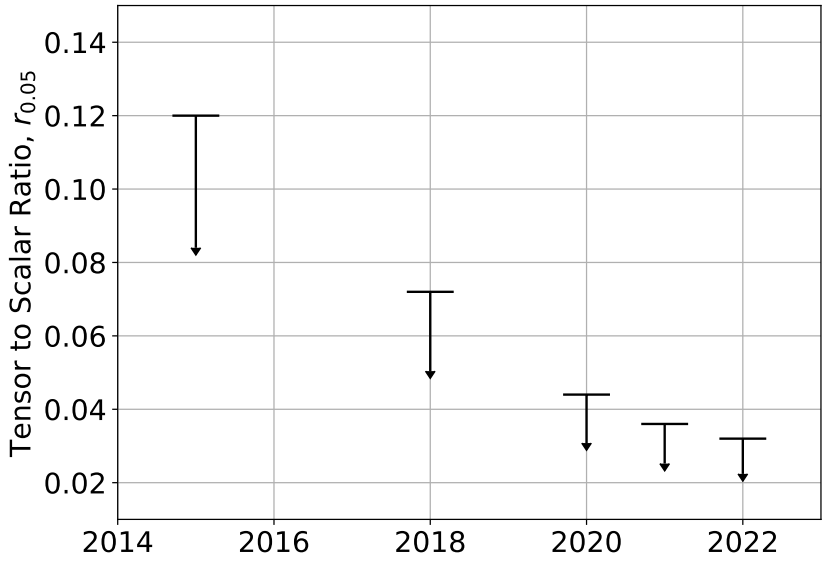

Figure 1.8: Upper limit of the tensor-to-scalar ratio r at a pivot scale of 0.05 Mpc^{-1} with 95% confidence levels [35, 36, 37, 10, 38].

1.3.3 Status of experimental constraints

Although a lot of CMB experiments searched for the primordial B-modes, it has not been discovered yet. They set upper limits on r as shown in Figure 1.8. WMAP and Planck led the setting of upper limits of r in 2010s [35], and BICEP/Keck, which are ground-based CMB experiments, set the most stringent upper limit $r < 0.032$ at the current time [38]. For ground-based experiments, fluctuation of observed signal is dominated by photon noise of the atmospheric radiation. It is much larger than CMB signals. The current upper limit is driven by this statistical uncertainty. In addition, we need to characterize the foregrounds precisely. The multi-frequency observations enable us to characterize the foregrounds. Therefore, recent CMB experiments install a lot of detectors with multi-frequency bands.

1.4 Optical depth in reionization era

1.4.1 Reionizaiton and CMB

After the recombination era, the CMB had not been scattered until the era of star generation ($\sim$ 1 billion years). Ultraviolet radiations from the stars have re-ionized neutral hydrogens. Then, CMB photons have been scatted by free electrons again.

Optical depth τ is a parameter which characterizes the reionization era, and it is defined as follows,

$$\tau \equiv \int_{t_{rs}}^{t_0} dt \bar{n}_e \sigma_\tau, \tag{1.20}$$

where t_{rs} is starting time of reionization, t_0 is the present time, $\bar{n}_e$ is mean number density

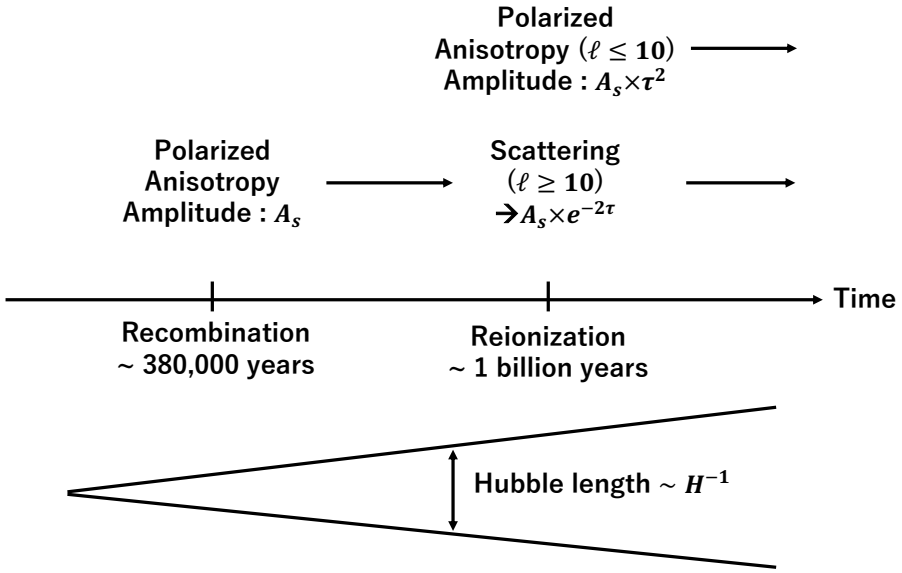

Figure 1.9: Imprint from the scattering during the reionization era to the anisotropy of the CMB polarization. Thomson scattering during the reionization era made two effects. One is to suppress power spectra ($\ell \geq 10$) generated at the recombination era by $e^{-2\tau}$. The other is to generate new polarized anisotropy at a large angular scale ($\ell \leq 10$). Its amplitude is proportional to $(1 - e^{-\tau})^2 \sim \tau^2$. Their multipole dependence depends on the Hubble length ($\sim H^{-1}$) at that time [39]. The Hubble length is approximately a range where the CMB can correlate with each other.

of free electrons, σ_τ is cross section between CMB and free electron. This value provides a measure of the opacity of free electrons to the CMB.

As shown in Figure 1.9, Thomson scattering during the reionization era made two effects in the CMB anisotropy: generating new polarized CMB and eliminating the anisotropy generated during the reionization era. The generation of new polarized CMB increased the EE power spectrum at low multipole region ($\ell \leq 10$). On the other hand, the elimination of the CMB anisotropy generated during the recombination era reduced the power spectra at higher multipole regions ($\ell \geq 10$). These effects to the power spectra are degenerated with other physics phenomena, such as amplitude of the primordial fluctuation and the sum of neutrino masses.

1.4.2 Degeneracy between Optical depth and Sum of neutrino masses in weak–lensing spectrum

The optical depth (τ) and the sum of the neutrino masses (Σm_ν) can be extracted by lensing power spectrum. As shown in Figure 1.10, the higher τ provides the lower amplitude of the power. The higher Σm_ν provides the lower amplitude of the power. Thus, they are degenerated variables. Figure 1.11 shows the degeneracy between τ and Σm_ν. The precise measurements of τ individually allow us to determine Σm_ν.

The TT power spectrum at high multipole regions is affected by the optical depth. It also has degeneracy with the amplitude of the primordial power spectrum (A_s). On the other hand, EE has different τ dependence at $\ell \leq 10$. Thus, we can precisely determine τ by comparing TT and EE at $\ell \leq 10$. Thus far, EE at $\ell \leq 10$ has large statistical

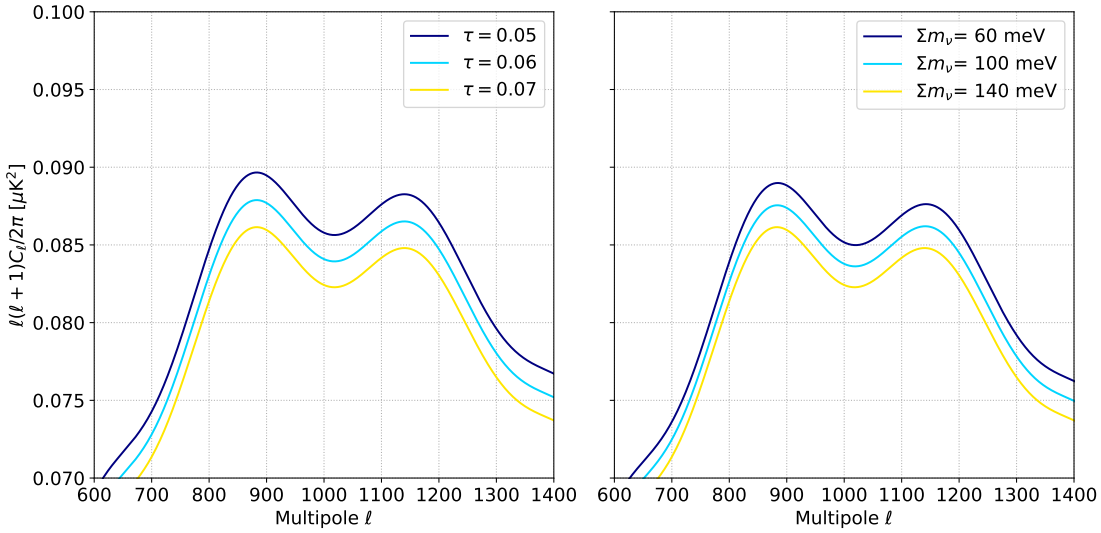

Figure 1.10: Both the optical depth (τ) and the sum of the neutrino masses (Σm_ν) vary the amplitude of the lensing power [20]. They are degenerated because they affect the lensing BB power spectra at high multipole region ($\ell \sim 1000$) in the same manner. Therefore, independent measurement of τ is important to determine Σm_ν precisely.

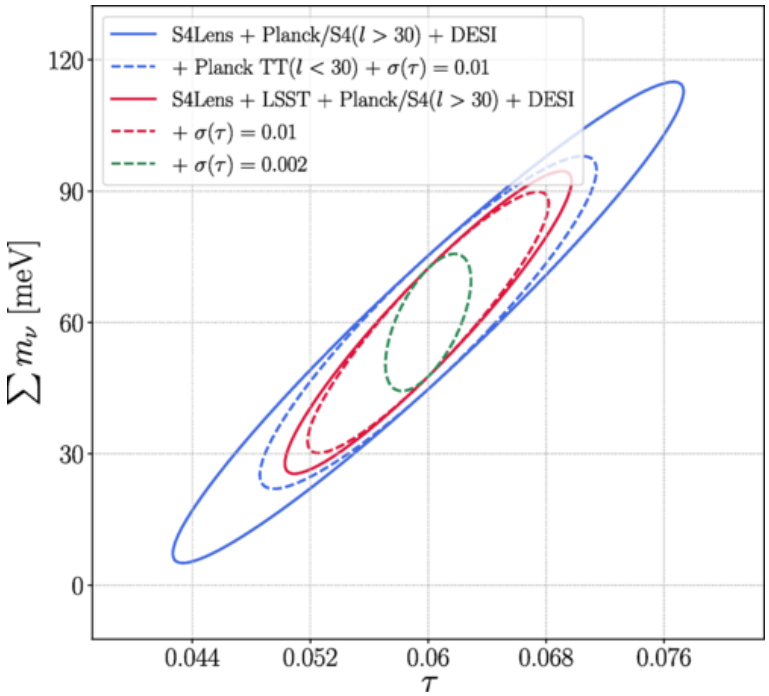

Figure 1.11: Degeneracy between the optical depth (τ) and the sum of the neutrino masses (Σm_ν). If we can determine the τ (green dashed line), Σm_ν can be determined precisely. This figure is taken from [40].

uncertainties, while the TT is precise. Therefore, it is important to observe EE at low multipole regions to determine τ. This is also important to measure Σm_ν precisely by unfolding degeneracy with τ.

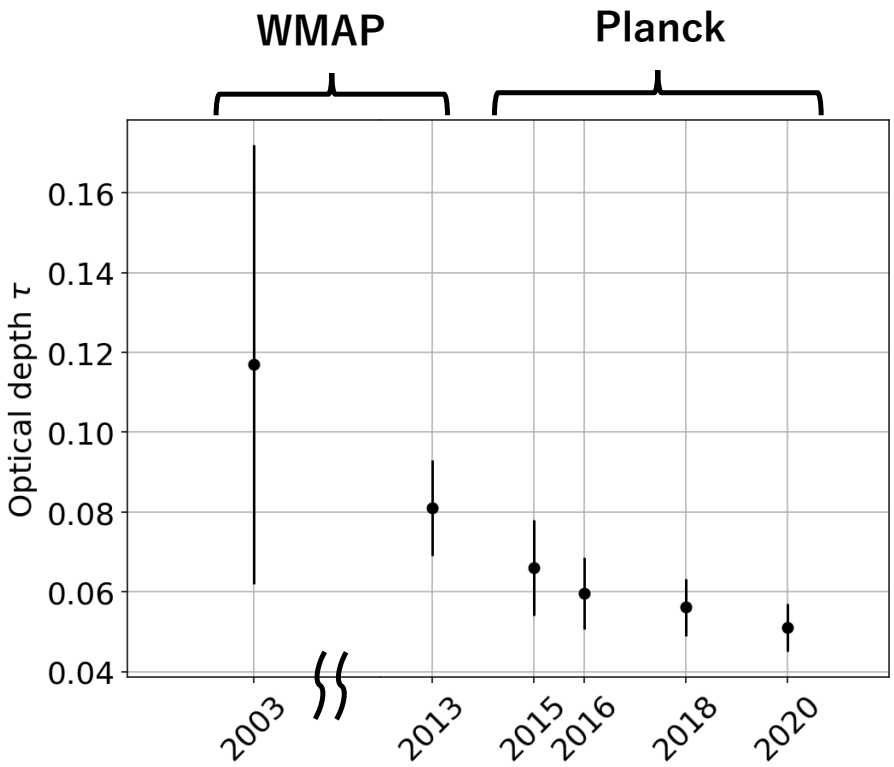

Figure 1.12: Best fit values with 68% confidence levels for optical depth τ measured by WMAP and Planck [41, 35, 42, 43, 21, 44]. The latest uncertaintiy of τ is $\sim 10\%$.

1.4.3 Measurement of τ from CMB experiments

Thus far, observation of the optical depth has been done by WMAP and Planck. Figure 1.12 shows history of the τ measurements. Its error became smaller. The latest uncertaintiy is $\sim 10\%$. However, the mean value systematically became to be smaller. Although this tendency is consistent within the uncertainties, independent observations is important to validate the optical depth with higher sensitive observations. Therefore, GroundBIRD [45] and other experiments such as CLASS [13], SPIDER [46], and QUIJOTE [12] aim to measure τ as well as other science topics such as B-modes from the inflation.

1.5 Joint study for τ by GroundBIRD and QUIJOTE

GroundBIRD is a ground-based CMB polarization experiment for observing the polarization of the CMB at a large angular scale. The GroundBIRD telescope is located at the Teide Observatory at an altitude of 2,400 m in the Canary Islands, Spain. Our science targets are detection of the primordial B-modes and measurement of the optical depth as shown in Figure 1.13. In order to achieve these targets, we have to separate the CMB and the foregrounds. They have different frequency dependencies as shown in Figure 1.14. Multipole-frequency observations allow us to separate them. Therefore, GroundBIRD observes two frequency bands of 145 GHz and 220 GHz with 138 and 23 single polarization-sensitive detectors, respectively. We plan to use low-frequency data taken

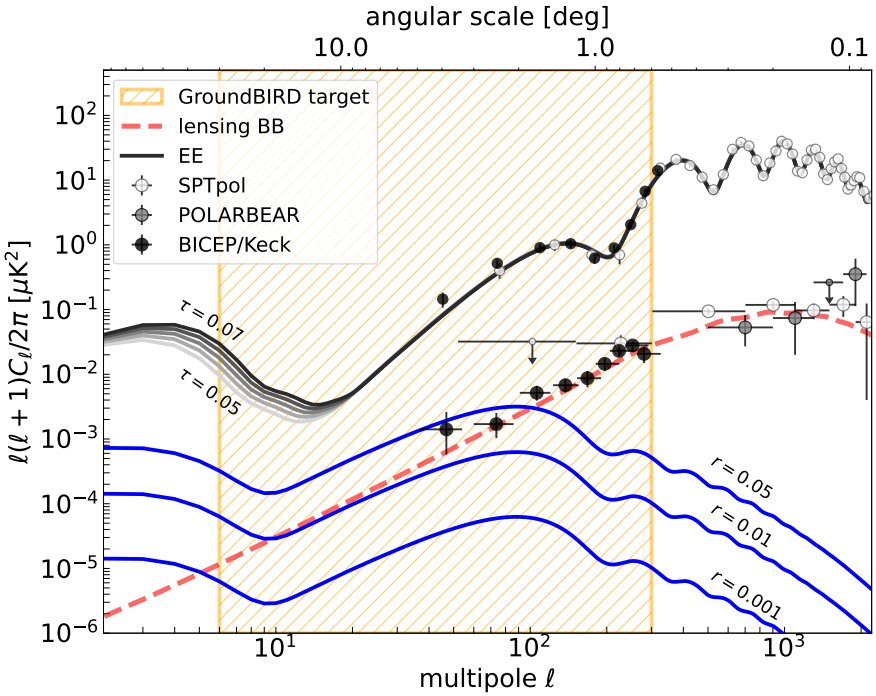

Figure 1.13: The theoretical and observed power spectra for EE and BB. GroundBIRD measures a region $6 < \ell < 300$. Our science targets are B-modes from primordial gravitational wave and the optical depth, τ [20, 21, 10, 14, 11].

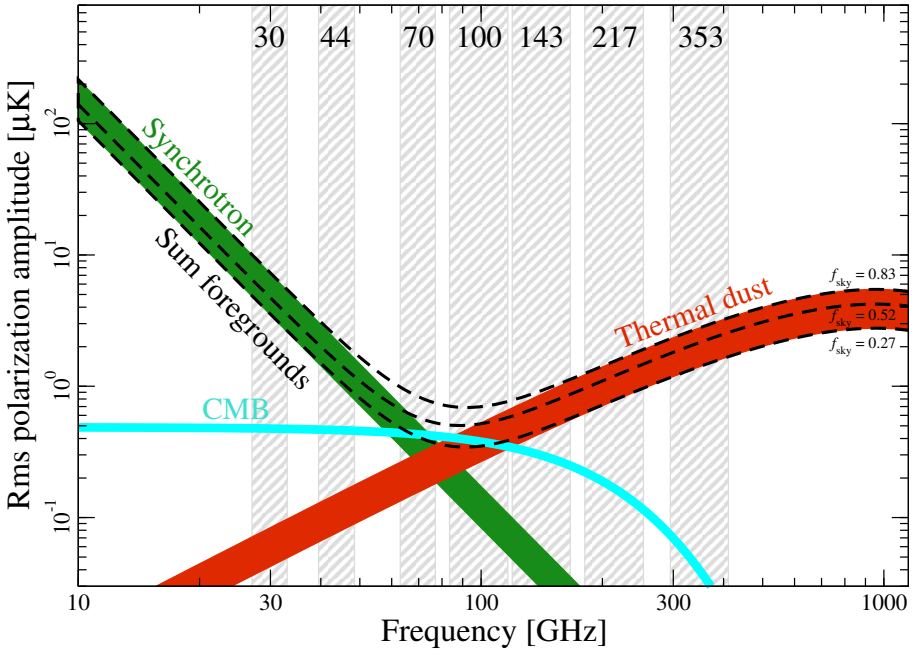

Figure 1.14: Root mean square of amplitude for foregrounds and CMB as a function of frequency [47]. This is made by Planck. The CMB showed by the cyan curve has a different frequency dependence than that of the foregrounds. Therefore, the multi-frequency observations allow us to separate the CMB from the foregrounds.

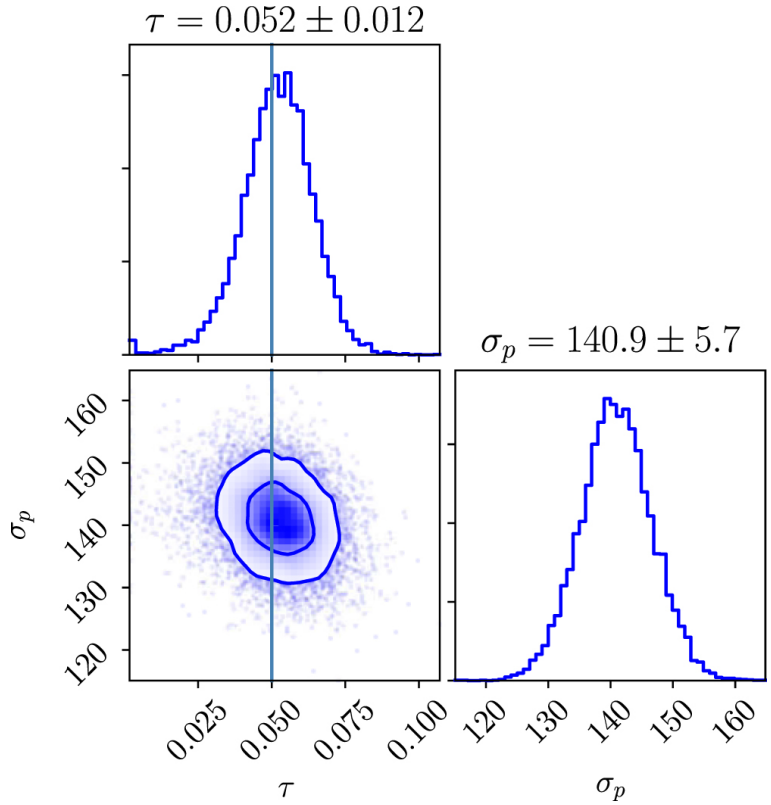

Figure 1.15: Forecast of the sensitivity on the measurement of τ using data taken by GroundBIRD and QUIJOTE. This figure is taken from [48].

Table 1.3: Expected noise level of polarization maps for GroundBIRD and QUIJOTE [48]

Telescope	Frequency band [GHz]	Noise level ($\mu K \cdot arcmin$)
QUIJOTE	11	3600
QUIJOTE	13	3600
QUIJOTE	17	5100
QUIJOTE	19	5100
QUIJOTE	30	160
QUIJOTE	40	91
GroundBIRD	145	110
GroundBIRD	220	780

by the QUIJOTE experiment which is located 20 m next to GroundBIRD. The QUIJOTE experiment has two telescopes: the multifrequency instrument (11, 13, 17, 19 GHz), and the thirty-gigahertz and forty-gigahertz instrument (30, 40 GHz). QUIJOTE also can observe a large sky coverage of $\sim 70\%$ as well as GroundBIRD, and their scanning strategies are similar (i.e. observation in azimuthal direction with fixed elevation). Therefore, the multi-frequency observations with GroundBIRD and QUIJOTE are appropriate strategy to separate CMB and the foregrounds at the large angular scale.

As shown in Figure 1.15, GroundBIRD and QUIJOTE collaboration made forecast to measure the optical depth (τ) with the $\sim 20\%$ uncertainty for three-year observation [48]. The expected noise level for each frequency band in this study is listed in Table 1.3.

1.6 Current status and Subjects of GroundBIRD

GroundBIRD has started science observations from May 2023. Until then, we had commissioning observations with prototype detectors. The purpose of the commissioning observations is to establish scan and calibration strategies, as well as to confirm and provide feedback to the detector design.

At first, we have to develop calibration methods of the telescope to achieve the science goals. We also need to understand the noise properties in the real data. We also need an analysis pipeline which consists of four steps; (1) applying the calibrations, (2) filtering the time-ordered data (TOD) based on the characterization of the noise, (3) map-making from the TOD (i.e., reconstructing the spherical patterns of CMB in the sky coordinates), (4) estimating angular power spectra. We will extract cosmological parameters based on the power spectra.

We performed commissioning observations from January 2022 – May 2022. Design of the detector array for the commissioning is almost the same as that for the science observations. Using the commissioning data, we develop calibration methods and characterize the noise prior to the science observations. In this thesis, we cover three topics as follows,

- Pointing (line-of-sight) calibration: The goal of the pointing accuracy is less than $4.7'$, which is one order of magnitude smaller than the angular resolution of the GroundBIRD telescope. This is the similar level to that was previously achieved by other CMB experiments.

- Polarization angle calibration: Polarization angle is defined as each antenna orientation in the sky coordinate system. The goal of precision of the polarization angle is $\lesssim 0.43^\circ$, which was previously achieved by other CMB experiments.

- Noise characterization: For characterizing the noise, we have to develop the analysis pipeline as a first step. Using the pipeline, we perform a study to characterize the noise and to suppress the effect of the noise.

1.7 Outline of this thesis

This thesis is organized as follows. In chapter 2, instruments of the GroundBIRD experiment and our scan strategy are described. In chapter 3, we describe details of the commissioning observations as well as the prototype detector arrays. In chapter 4, we explain an analysis framework as well as sky coordinate systems. In chapter 5, pointing calibration using the Moon is described. In chapter 6, we describe the calibration of the polarization angle using the pointing information. In chapter 7, the noise study is described whereas this is not completed yet. In chapter 8, we discuss the results obtained in chapters 5–7 as well as the prospects based on them. Finally, our conclusions are presented in chapter 9.

Chapter 2

GroundBIRD Experiment

2.1 Teide Observatory

GroundBIRD is a ground-based CMB polarization experiment. Figure 2.1 is a photo of the GroundBIRD telescope.

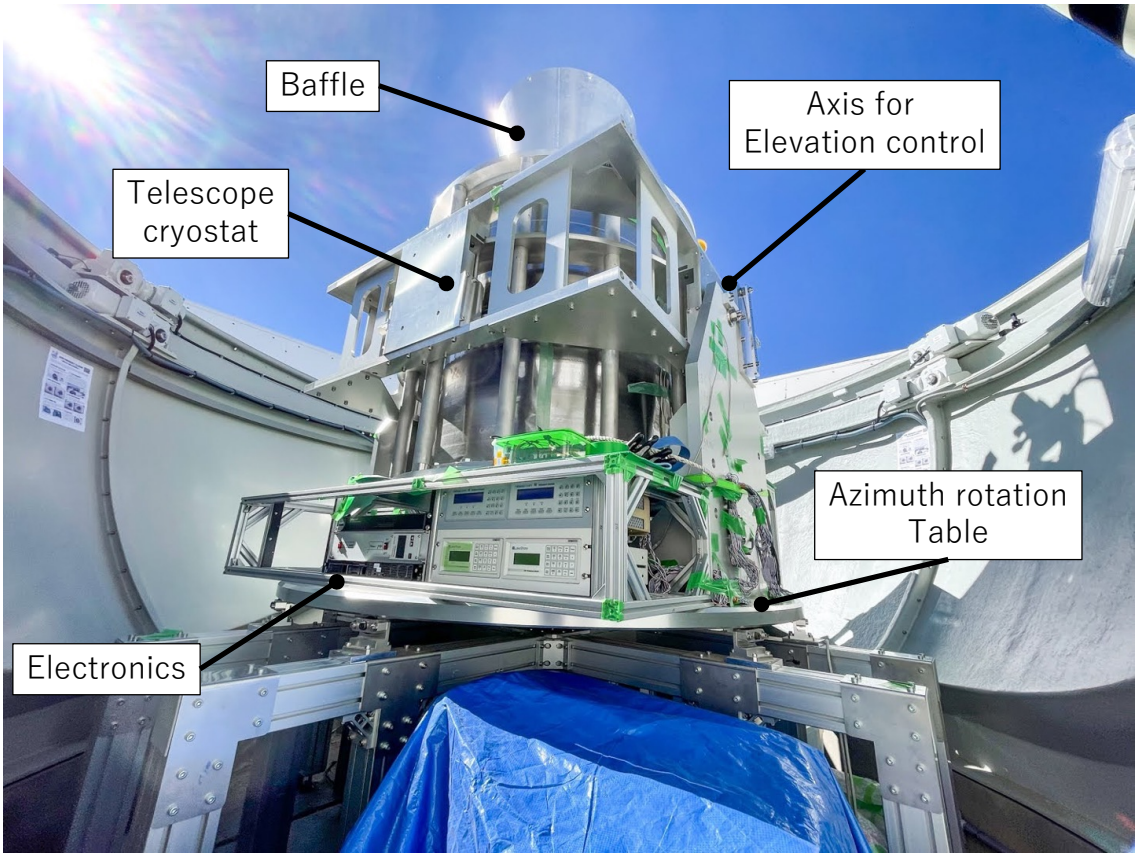

Figure 2.1: Photo of the GroundBIRD telescope. The telescope cryostat and electronics are located on the azimuth rotation table [49]. Those can be rotated in the azimuth with a fixed elevation with up to the speed of 20 revolutions per minute (RPM).

The telescope is located at the Teide Observatory in the Canary Islands, Spain. Its longitude, latitude, and altitude are 28°18′ N, 16°30′ W, and 2,400 m, respectively. The

Teide Observatory is a great place to observe the universe from the ground thanks to the excellent quality of the sky. For instance, a median of precipitable water vapour (PWV) was observed 3.5 mm at the Teide Observatory from 2012 to 2013 [50]. There is another CMB experiment, QUIJOTE (Q-U-I JOint Tenerife), next to the GroundBIRD telescope as shown in Figure 2.2.

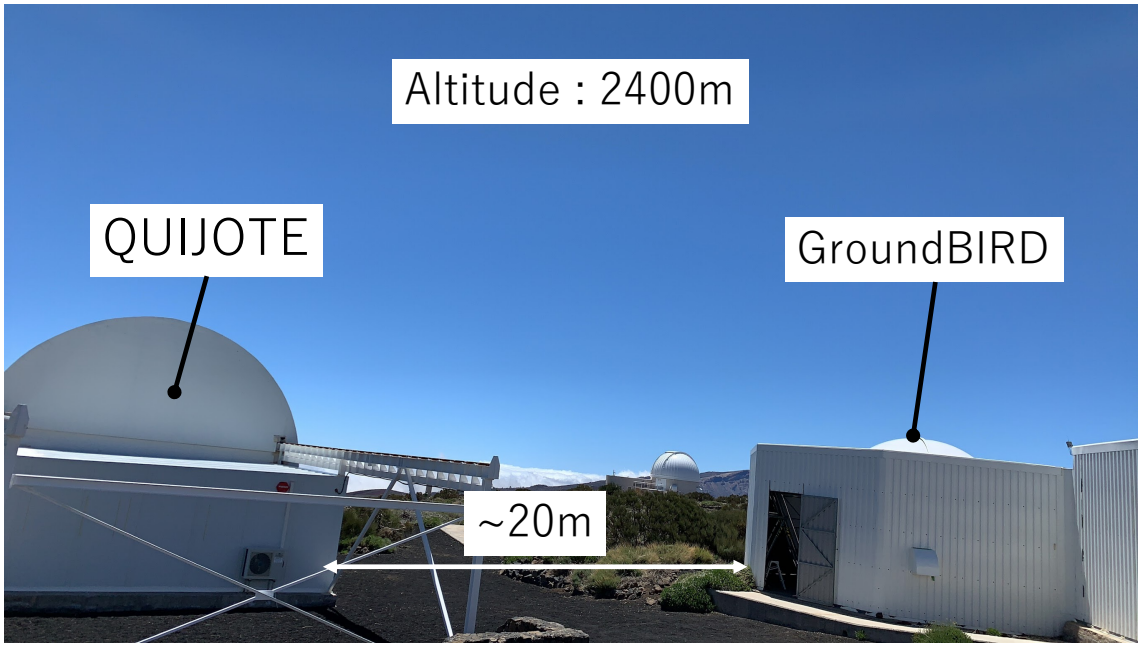

Figure 2.2: Photo of Teide Observatory around GroundBIRD and QUIJOTE. Teide Observatory is located in the Canary Islands, Spain. The altitude of Teide Observatory is approximately 2,400 m. An astronomical seeing condition at Teide Observatory is great for observations. (e.g., median PWV for one year is 3.5 mm [50])

2.1.1 Scan strategy

GroundBIRD observes the sky by rotating the telescope in an azimuthal direction with a fixed elevation angle. The maximum rotation speed is 20 revolutions per minute (RPM). This rapid scan modulation which mitigates the effects of atmospheric fluctuations is a unique observational strategy [45]. In addition, continuously rotating observation enables us to observe a large sky coverage for one day due to the Earth rotation as illustrated in Figure 2.3. For instance, we can observe $\sim$ 45% of the full sky if the GroundBIRD telescope is fixed the elevation angle of 70° [48].

Figure 2.4 is an example of a hit map in the equatorial coordinate system for 20 hours observations. This hit map is made by using healpy [51, 52] with the parameter $N_{\mathrm{side}} = 128$. Details of the coordinate systems are described in section 4.1. The color represents the amount of data at each pixel (i.e., each pointing). We used data taken with 19 detectors for almost one day. The detector's configuration is described in chapter 3. We did not perform observations at the gap around the center due to regeneration of the Helium sorption cooler. We also do not observe when the Sun exists around the telescope pointing.

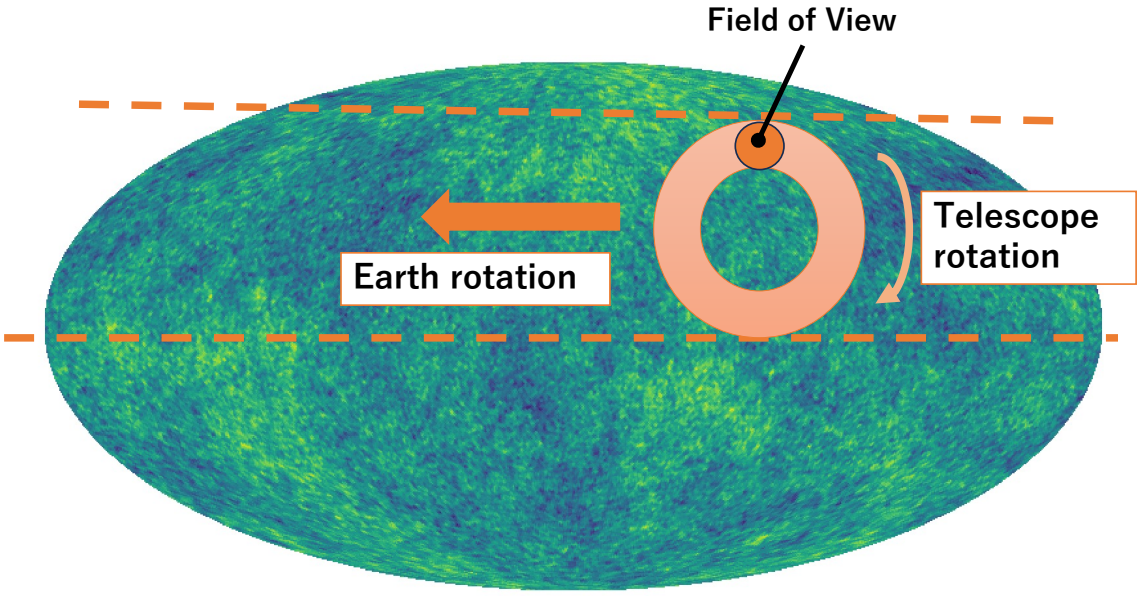

Figure 2.3: Scan strategy of the GroundBIRD. GroundBIRD observes a sky within a field of view of $\pm 11^{\circ}$. Its rotation in the azimuth with fixed elevation lets GroundBIRD observe the sky in a circle region in the equatorial coordinate system. The combination of the telescope rotation and Earth rotation allows us to observe almost half of the full sky in one day.

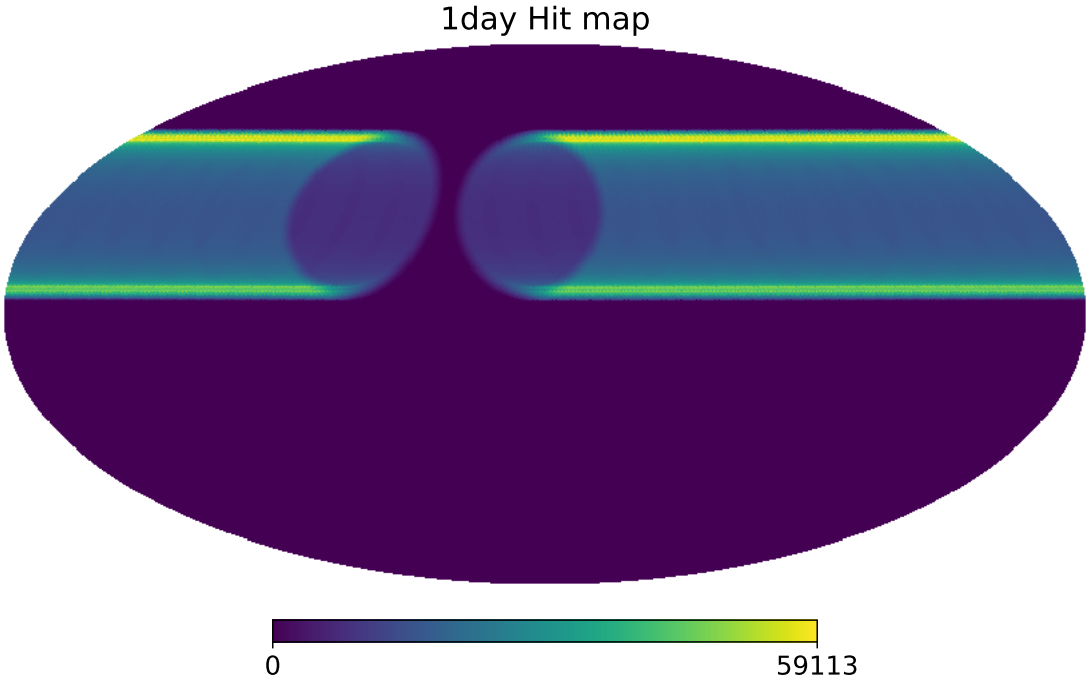

Figure 2.4: Hit map of GroundBIRD telescope with 19 detectors for 20 hours in the equatorial coordinate system. This map is created using healpy [51, 52] with the parameter $N_{\mathrm{side}} = 128$.

[0]http://healpix.sourceforge.net

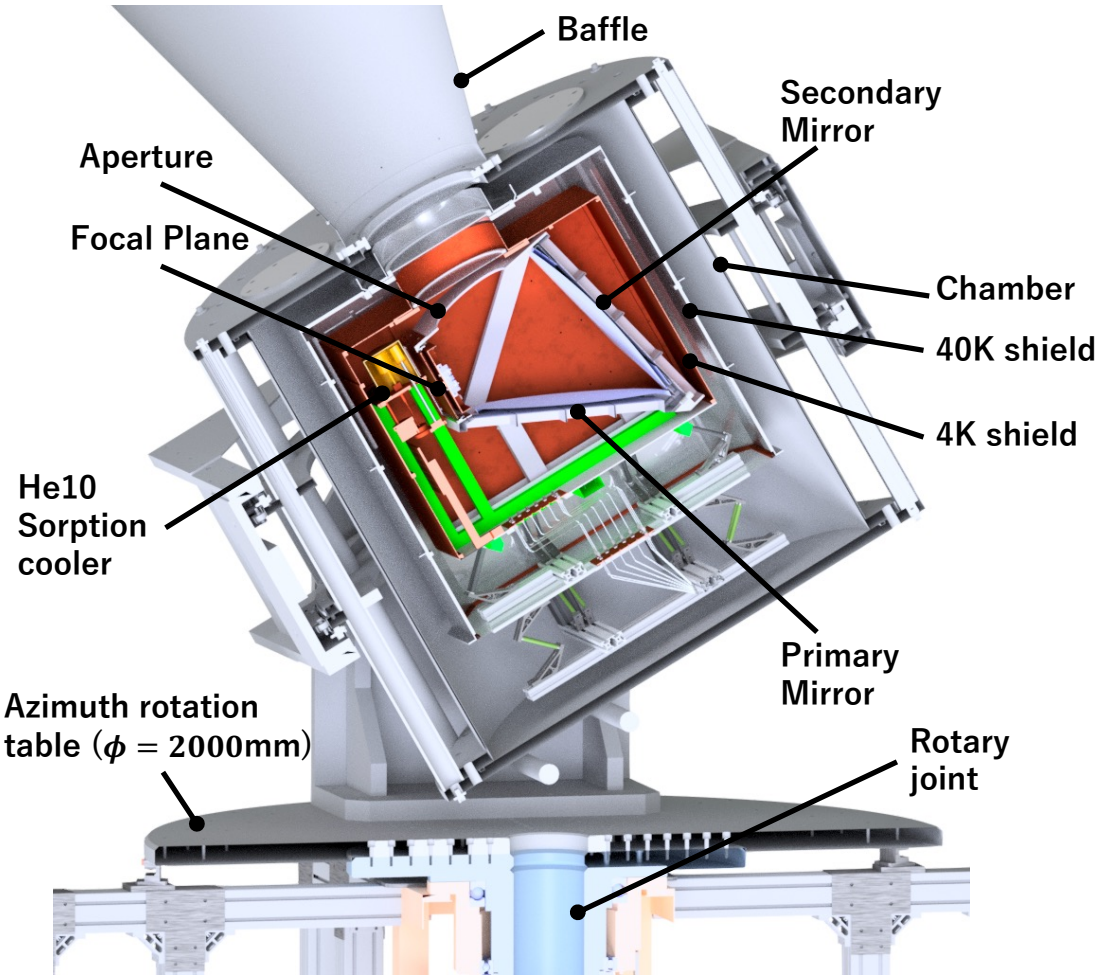

Figure 2.5: Cross-sectional illustration of the GroundBIRD cryostat. The chamber keeps a vacuum state inside the cryostat. The 4 K and 40 K shields reduce the light generated from outer (i.e., hotter) parts. We cool the parts inside the cryostat to 4 K with a Pulse Tube Cooler (PTC) and the focal plane temperature to around 280 mK with the He10 sorption cooler. The CMB can be focused with the Mizoguchi-Dragone dual reflector. It is detected by MKIDs placed on the focal plane. The rotary joint lets the telescope rotate while keeping electrical connections and compressed He for the PTC between the parts above and below the rotation table.

2.2 GroundBIRD telescope

GroundBIRD telescope is located on an azimuth rotation table and rotates continuously in the azimuthal direction at a fixed elevation as shown in Figure 2.1. Some electronics (e.g., detector readout, thermometers) are also set on the rotation table. We protect them from dust, rain, and sunlight with a dome when we do not perform observations. We can operate all systems (e.g. opening/closing the dome, tilting and rotating the telescope) remotely.

Figure 2.5 shows a cross-sectional illustration of the GroundBIRD cryostat. The GroundBIRD cryostat consists of three shields: the chamber (300 K shield), 40 K shield, and 4 K shield. The chamber keeps a vacuum state inside the cryostat. We set magnetic

Figure 2.6: Picture inside the cryostat. The surface except the mirrors is covered by the absorber. We use Mizuguchi–Dragone dual reflector which is a combination of a primary paraboloid and a secondary hyperboloid mirror.

shields (MS-FR, PROTERIAL) at the inner side of the chamber to reduce unwanted magnetic fields (e.g., Geomagnetism effects). The 40 K (4 K) shield cut thermal radiation emitted from hotter (i.e., outer) instruments. We covered both shields with Multi-Layer super Insulation (MLI) and the magnetic shields to reduce the thermal radiation and the magnetic fields, respectively. 40 K and 4 K circumstances are realized with a Pulse Tube Cooler (PT415, Cryomech). We fixed instruments at 40 K and 4 K circumstances rigidity with glass fiber reinforced polymer (GFRP) tubes and carbon fiber reinforced polymer (CFRP) tubes, respectively. These tubes, while mechanically strong, have low thermal conductivity under low-temperature conditions for thermal insulation.

Sky signals come through the baffle, a polyethylene window [53], and a Radio-Transparent Multi-Layer Insulation (RT-MLI) [54] into inside the cryostat. We set the baffle to reduce the unwanted radiation from outside [55]. The polyethylene window, which is transparent for millimeter-wavelength radiation keeps the vacuum state inside the cryostat. The RT-MLI, which is also transparent for the millimeter-wavelength radiation reduces radiation of high-frequency bands (i.e., $>$ 1 THz). The sky signals are focused onto focal plane detectors using a Mizuguchi–Dragone dual reflector [56, 57, 58]. We set it at 4 K circumstances to reduce thermal radiation from the mirrors themselves. An aperture in front of the mirrors is a diameter of 220 mm. It mainly determines the beam width of the GroundBIRD telescope. The beam is defined as the telescope response with respect to the angle from the pointing direction. The angular resolution is represented by the beam width, which is the full width at half maximum (FWHM). For instance, beam widths of the GroundBIRD telescope for the frequency bands of 145 GHz and 220 GHz are 0.60° and 0.42°, respectively [59]. Their ellipticities are up to 1% and 2%, respectively. The inner side of the baffle and the un-reflected parts of the mirror are covered with an absorber for millimeter-wavelength bands (ECCOSORB AN72, E&C ENGINEERING K.K.) as shown in Figure 2.6.

The sky signals are detected by antenna-coupled Microwave Kinetic Inductance De-

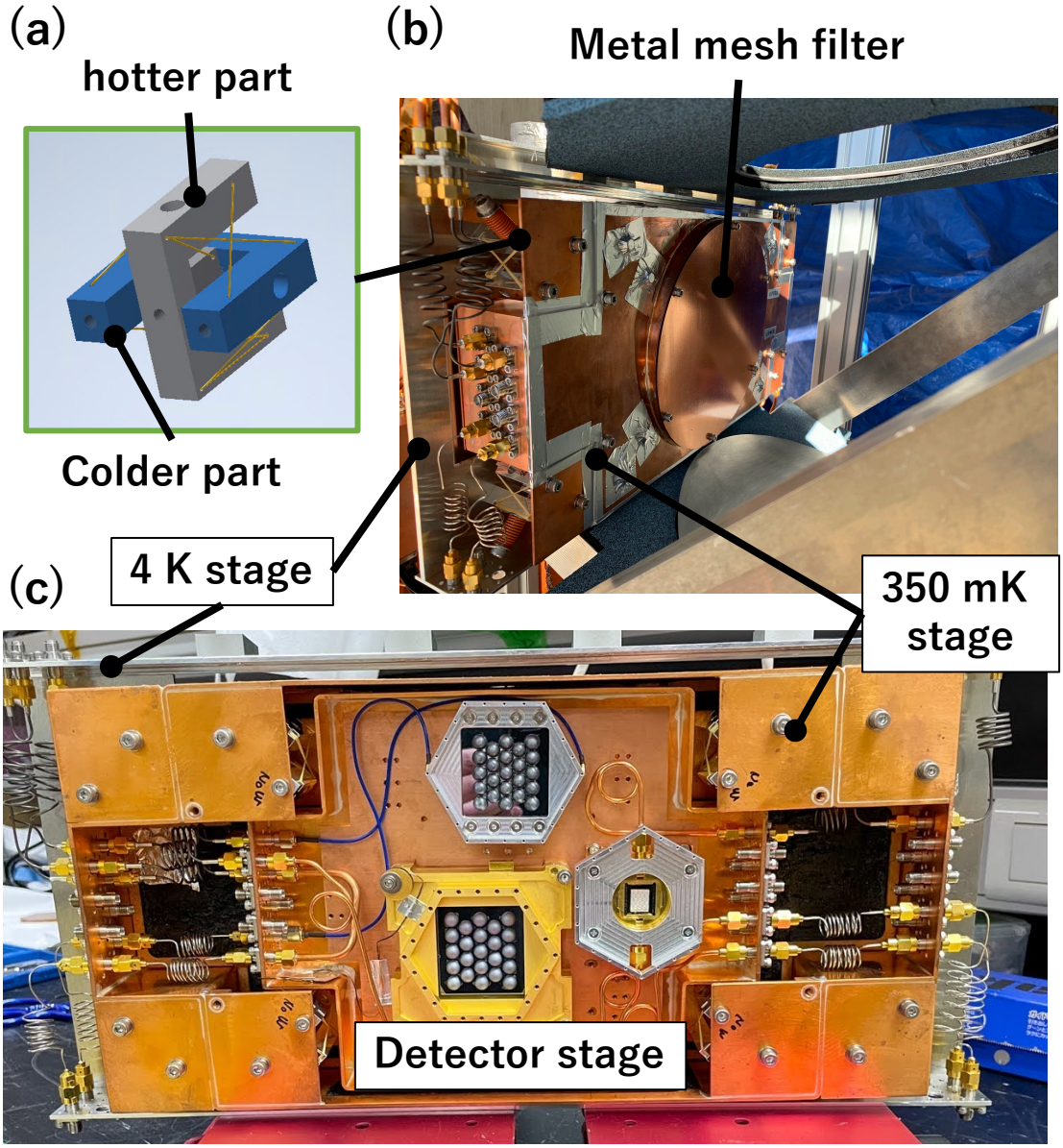

Figure 2.7: (a) Thermally isolated structure constructed by aluminum parts and string made from Kevlar. The structure is kept only by the tension of the string. (b) Photo of the focal plane installed in the cryostat. A metal mesh filter (Low pass filter) is set in front of a detector stage. (c) Photo of the detector stage of the focal plane. This configuration was in December 2021, which is described in chapter 3.

tectors (MKIDs) with silicon lenslet in front of each antenna. The detectors are mounted on the detector stage as shown in Figure 2.7 (c). We cool the detectors as well as the detector stage below 300 mK with the Helium sorption cooler (CRC-GL10-008, CHASE RESEARCH CRYOGENICS LTD). We realize the focal plane by using custom-made thermally isolated structure as shown in Figure 2.7 (a). This structure consists of aluminum parts and Kevlar strings. It enables us to fix the focal plane rigidity while providing great thermal isolation thanks to the low thermal conductance and a small cross section.

According to the simulation study by the CST Microwave Studio, the beam width of

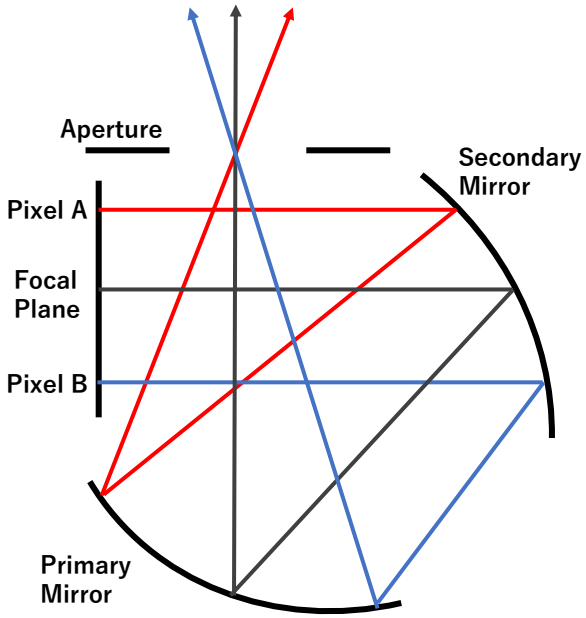

Figure 2.8: The pointing of each detector pixel depends on its location in the focal plane. The pointing difference is called collimation offset. We use Mizuguchi–Dragone dual reflector which is a combination of a primary paraboloid and a secondary hyperboloid mirror. The aperture diameter is 220 mm. For two mirrors, diameters at optical area are the same. The diameters for the minor-axis and the major-axis are 360 mm and 490 mm, respectively [49].

the telescope for 145 GHz band is $36'$ (i.e., $0.60°$) [59]. The beam width for 220 GHz is $25'$ (i.e., $0.42°$). Their ellipticities are at most 1% (2%) for 145 GHz (220 GHz) according to this simulation.[1] Because each detector is placed at the different position on the focal plane, each detector points to a different position in the sky as shown in Figure 2.8. The angular interval between the collimations of each detector in the sky is typically $0.85°(51')$. Therefore, area for detectors in the focal plane determines a Field-of-View (FoV). FoV of the GroundBIRD telescope is $\pm 11°$.

We installed several metal mesh filters (QMC Instruments) to reduce unwanted radiation. Three low-pass filters are set in a window of each shield as well as in the focal plane. Figure 2.7 (b) shows the filter mounted at the 350 mK stage. To specify the frequency bands, we install low-pass and high-pass filters in front of each detector array. All transmittance of the filters for the 145 GHz band is shown in Figure 2.9. We select the radiation of frequency band 145 ± 15 GHz. We summarize the specification of the GroundBIRD telescope in Table 2.1.

As explained in section 2.1.1, the fast rotation is essential for the GroundBIRD experiment. The most challenging point is the supplement of Helium gas for the PTC from a compressor on the ground to the PTC on the rotation table. We achieved it with rotary joints as shown in Figure 2.10. A custom-made rotary joint [60] for Helium gas enables us to circulate Helium from the compressor to the PTC. A commercial rotary joint (Model-

[1] There is no laboratory measurement to confirm this simulation. Validation using other planets such as Jupiter is a future study.

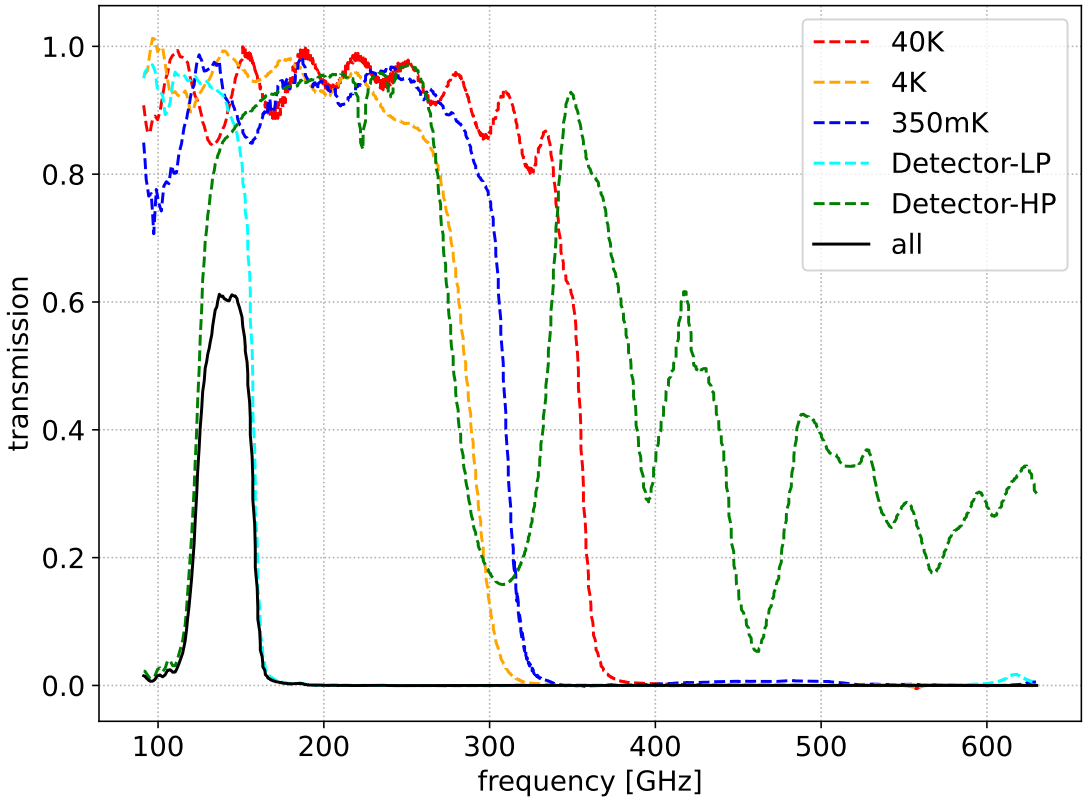

Figure 2.9: Transmittance of the metal mesh filters installed inside the cryostat for 145 GHz frequency band.

Table 2.1: Optical specifications of the GroundBIRD telescope [59]

Frequency bands	145 GHz, 220 GHz
Aperture diameter	220 mm
Beam width for 145 GHz	$0.60^\circ(36')$
Beam width for 220 GHz	$0.42^\circ(25')$
Ellipticity for 145 GHz	$< 1\%$
Ellipticity for 220 GHz	$< 2\%$
Major minor diameter of the mirror	440 mm
Mirror minor diameter of the mirror	360 mm
Focal plane diameter	20mm
Field of view	$\pm 11^\circ$
Typical collimation interval between each detector	$0.85^\circ(51')$

830, Mercotac Inc.) is used for an electrical connection between the ground and the place on the rotation table. These two rotary joints enable to rotate the telescope at 20 RPM.

2.3 Microwave Kinetic Inductance Detector

The fast rotation scanning requires detectors with a fast response. Superconducting detectors are popular to use for CMB experiments because of their low noise property. One

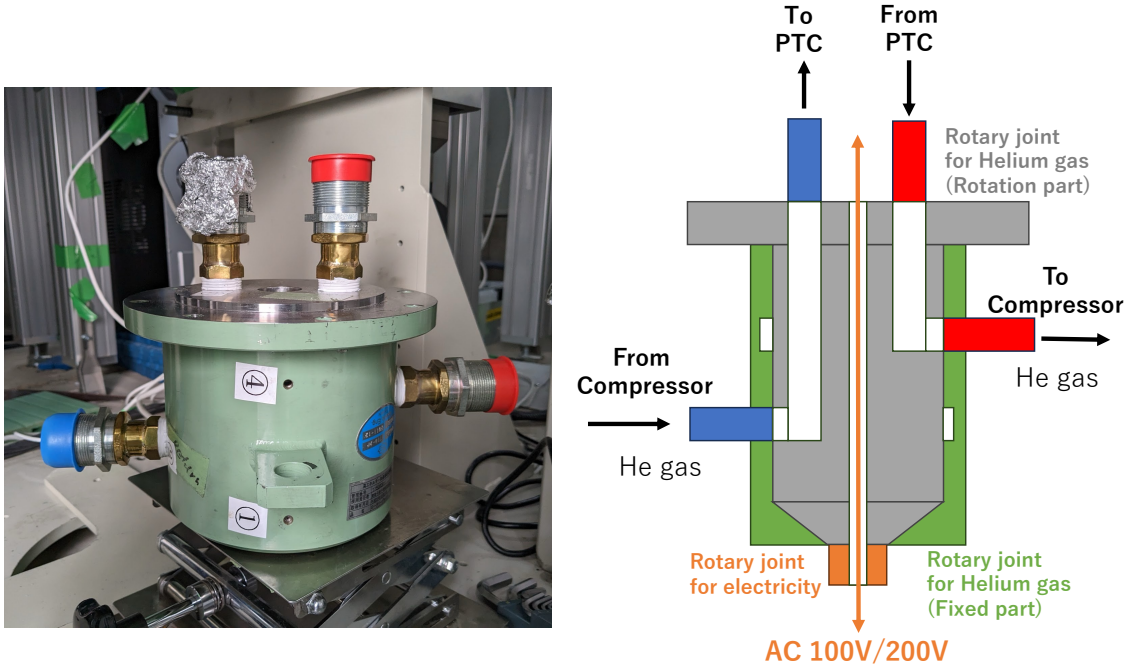

Figure 2.10: Picture and schematic of the rotary joint. The rotary joint for Helium gas enables its transfer between the compressor and the PTC. The rotary joint for electricity makes electrical connection between top and bottom of the rotation table.

of the superconducting detectors often used in CMB experiments is the Transition Edge Sensor (TES) [61, 62]. However, its response speed ($(\mathcal{O}(1)$ ms) [62]) is not fast enough for GroundBIRD. Therefore, GroundBIRD adopted a Microwave Kinetic Inductance Detectors (MKID) [63], which is another type superconducting detector with a fast response ($< \mathcal{O}(1)$ ms).

As illustrated in Figure 2.11 (a), an MKID consists of an antenna-coupled superconducting resonator and a feed line capacitively coupled to each resonator. These are constructed with a coplanar waveguide (CPW) on a dielectric substrate (e.g., Silicon). The MKID equivalents to the circuit of Figure 2.11 (b) electrically. The parallel LCR circuit corresponds to the resonator. It is capacitively coupled to the feed line. L and R in the resonator depend on the superconducting properties. The length of the resonator corresponds to a quarter of a wavelength of fed microwaves. Therefore, this type of MKID is known as a quarter-wave MKID. At the current time, a hybrid-type MKID [64] is popular because it can achieve lower noise and higher sensitivity than that of MKIDs made from a single material. The resonator of the hybrid-type MKID is split into two parts:

- The sensitive part located close to the antenna: It is made from a sensitive material (e.g., Aluminium) for the center strip and a low noise material (e.g., NbTiN) for the ground as shown in the top-left of Figure 2.11. Its geometry is designed to be as narrow as possible to achieve high sensitivity because smaller area realizes high sensitivity.

- The coupling part located at the feed line: It is made from a low-noise material (e.g., NbTiN) for both the center strip and the ground as shown in the bottom-left

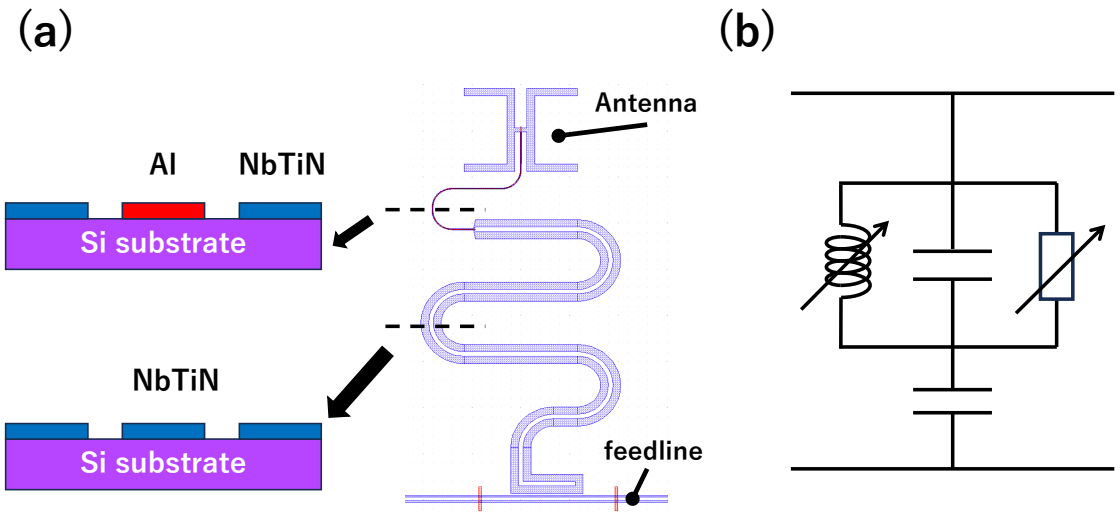

Figure 2.11: (a) A resonator of the MKID consists of two parts; the sensitive part and the coupling part where the wide CPW is made from only NbTiN. For the sensitive part, we use a narrow CPW which is made from Al and NbTiN. For the coupling part, we use a wide CPW which is made from only NbTiN. The CMB is collected by the antenna. We measure its power as the change of resonant condition by breaking Cooper pairs. The resonant condition is read by a feedline coupled to the resonator. (b) Electrical equivalent circuit of an MKID. Breaking the Cooper pairs and generating quasiparticles changes the inductance and resistance. Thus, a resonance condition is changed.

of Figure 2.11. Its geometry is designed to achieve low noise property.

The photon (or other energy) detection principle of the MKID is to measure a change in the resonance. The incident photon breaks Cooper pairs and creates quasiparticles inside the resonator. The kinetic inductance and resistance of the resonator depend on the number density of Cooper pairs and quasiparticles, respectively. Consequently, the resonance is changed based on the power of the incident photon. The resonance is monitored with a transmittance of fed microwaves. Figure 2.12 shows examples of the change of the resonance in a phase and an amplitude.

Based on these properties, the MKID has three advantages,

- Fast response : Two quasiparticles close to each other become Cooper pair again. This is known as the recombination of the quasiparticles. The response speed of the MKID depends on time for the recombination of the quasiparticles. This time is also known as quasiparticle lifetime, which is typically $\mathcal{O}(10)$ ms under the condition for GroundBIRD. This is faster than the response speed of the TES. This property enables us to observe with a high sampling rate (e.g., 1 kHz).

- Easy multiplexing : The resonant frequency is proportional to the length of the MKID. Thus, we can easily realize different resonant frequencies for each MKID by assigning the different lengths to each resonator. We can read $\mathcal{O}(1000)$ MKIDs by using frequency domain readout multiplexing with only a pair of readout cables. This property enables us to install a lot of detectors inside a cryostat while a heat load is kept at a minimum amount.

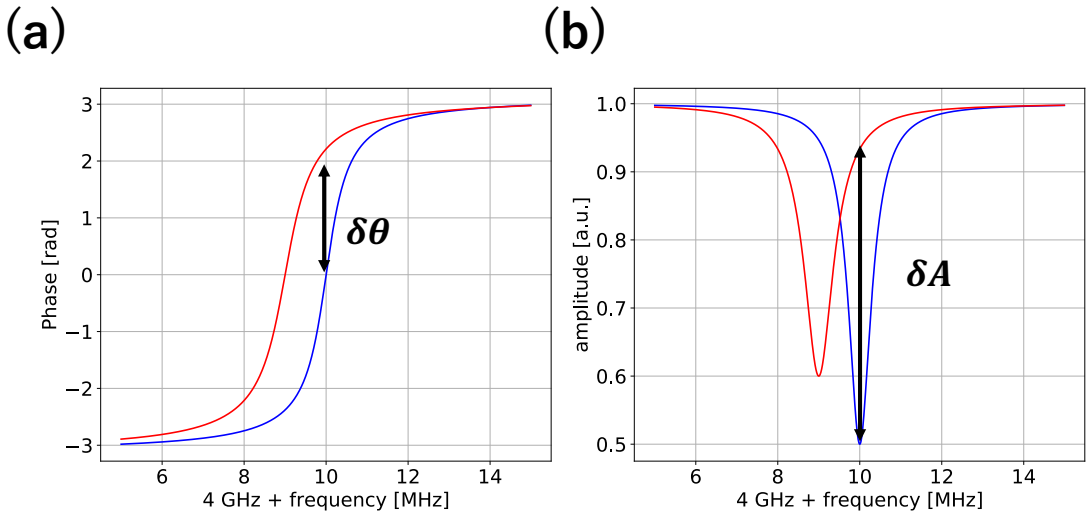

Figure 2.12: (a) Example of the change of the phase ($\delta\theta$) of the resonance at the resonant frequency. (b) Example of the change of the amplitude (δA) of a transmittance (S_{21}) of the resonance at the resonant frequency.

- Simple fabrication : The geometry of the MKID is more simple than that of other superconducting detectors (e.g., TES). This property enables us to fabricate it easily and achieve a high yield rate.

2.4 Readout systems

Readout systems of GroundBIRD consist of mainly three components: detector readout, azimuth readout, and elevation readout. As illustrated in Figure 2.13, the detector readout and the elevation readout are placed on the rotation table. The azimuth readout is installed on the ground. These readout systems are synchronized by using a common pulse which is distributed to all readout systems. In this Section, these readout systems as well as the synchronization among them are described.

2.4.1 Detector readout

The readout system of the MKID for GroundBIRD was developed originally [66]. Figure 2.14 and Figure 2.15 show a photo and a schematic of the readout electronics outside the cryostat. An FPGA board (KCU105, Xilinx) synthesizes a multi-tone wave to introduce power to each resonator. The digital microwaves are converted to an analog signal with a custom-made board "Rhea" [67]. The Rhea board has a digital-to-analog converter (DAC) as well as an analog-to-digital converter (ADC). Both sampling rates are 200 MHz. Therefore, the Rhea board can convert the microwave at a frequency below 100 MHz (IF signal). Two input/output whose phase difference is 90° provides the effective readout bandwidth of 200 MHz. We cut the microwaves above a frequency of 100 MHz with a low-pass filter (SLP-100+, Mini-Circuits) in front of the Rhea board. We optimize the amplitude of the microwaves with commercial amplifiers (ZX60-43-S+, Mini-Circuits) and attenuators. Because the typical resonant frequency of the MKID for GroundBIRD is

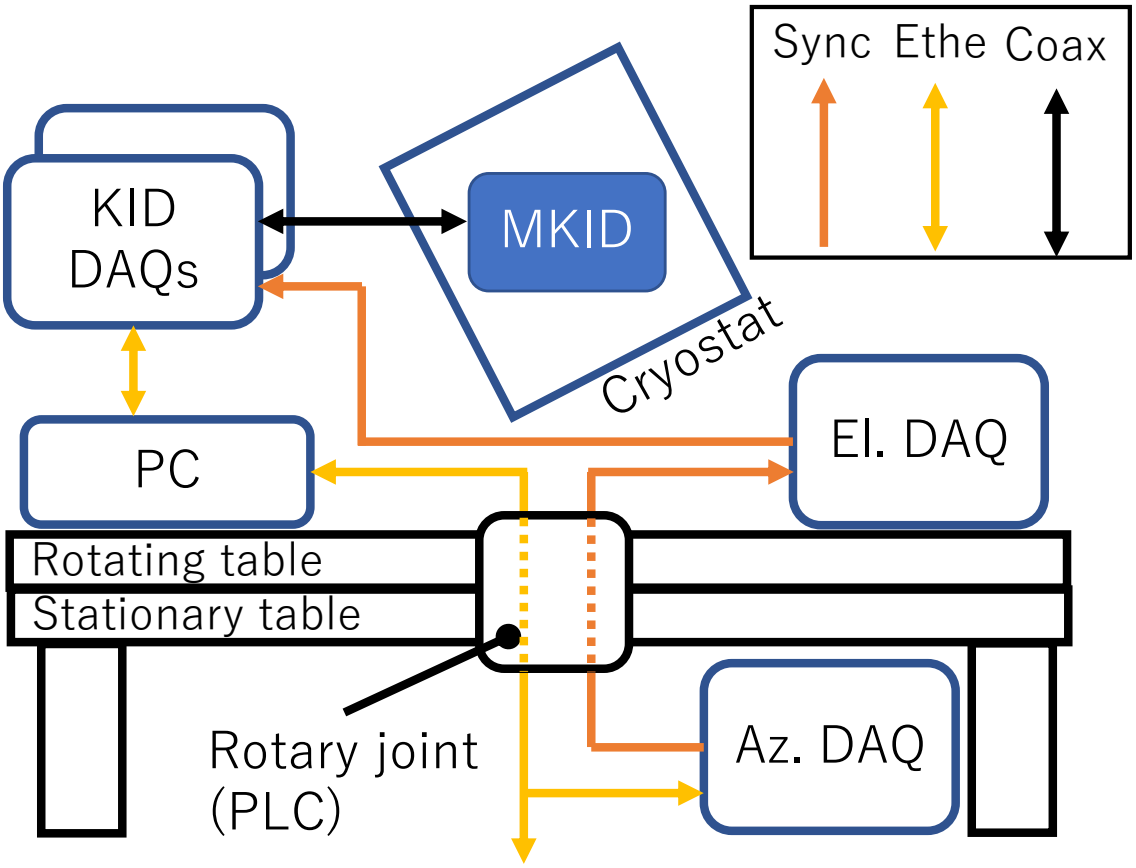

Figure 2.13: DAQ systems for the GroundBIRD. DAQs for MKIDs and elevation encoder are placed on the rotation table, while DAQ for azimuth encoder is placed under the rotation table. The synchronization signal is generated at the a DAQ for the azimuth encoder. It is sent to the DAQ for the elevation encoder and MKID in turn by using Power Line Communication (PLC) through the rotary joint. We communicate The PC on the rotation table via the PLC. MKIDs are readout via coaxial cables between the DAQ and MKIDs.

4.5GHz (RF signal), the microwave is up-converted with an IQ mixer (MLIQ-0218L, Marki Microwave). Reference microwaves at a frequency range of 4.5 GHz for the up-conversion is generated at a local oscillator (FSL-0010, NI Microwave components).

We modify the amplitude of the up-converted microwaves again with the attenuator and an amplifier (ZX60-83LN12+, Mini-Circuits) with respect to the response and noise of the MKID. The microwaves enter the cryostat through a DC block (INMET 8039, API technologies corp.). It is attenuated by 30 dB to reduce thermal noise before going to 4 K circumstance as shown in Figure 2.16. The output microwaves from the MKID are amplified by a cold low noise amplifier (C-LNA, LNF-LN4_8C, LOW NOISE FACTORY) installed at 4K circumstances to achieve a high signal-to-noise ratio. The microwaves come back to the readout electronics. It is converted to a digital signal at the Rhea board. We extract the amplitude and phase responses of the MKID based on a Direct Down-Conversion (DDC) logic [68] in the FPGA board. We record the downsampled signals at a sampling rate of 1 kHz.

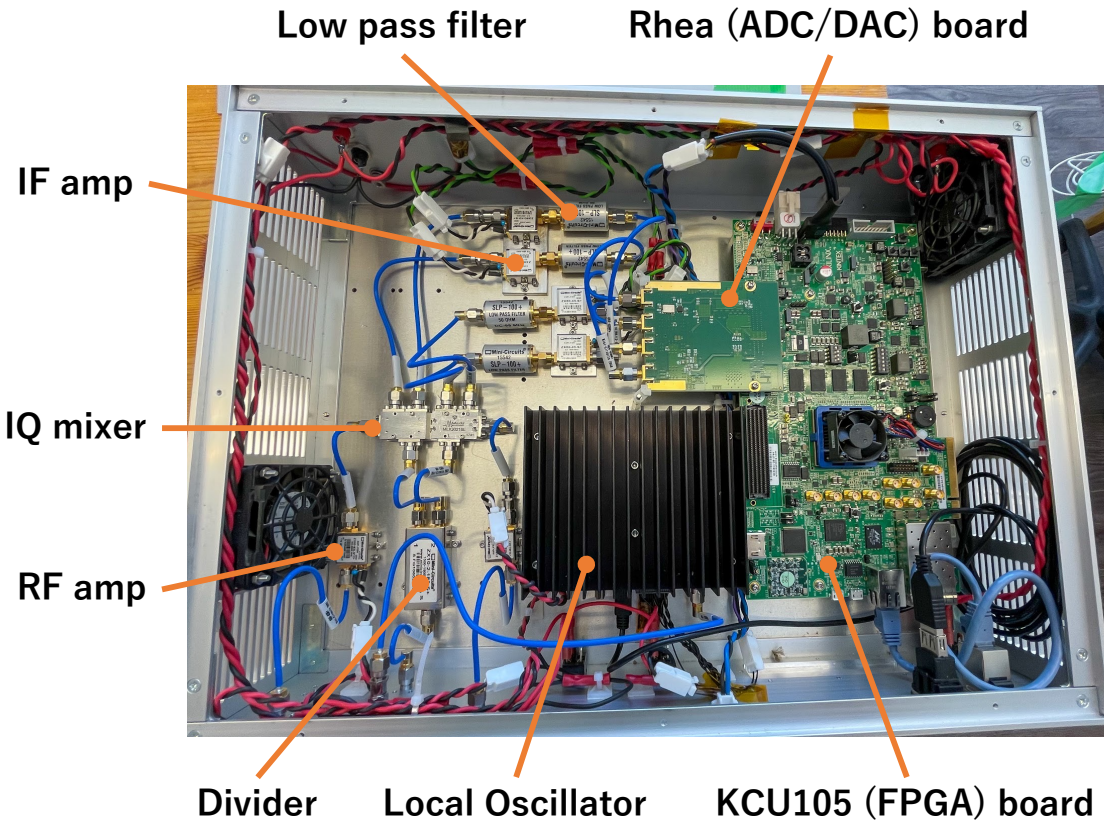

Figure 2.14: Photo of the readout electronics for the MKID outside the cryostat.

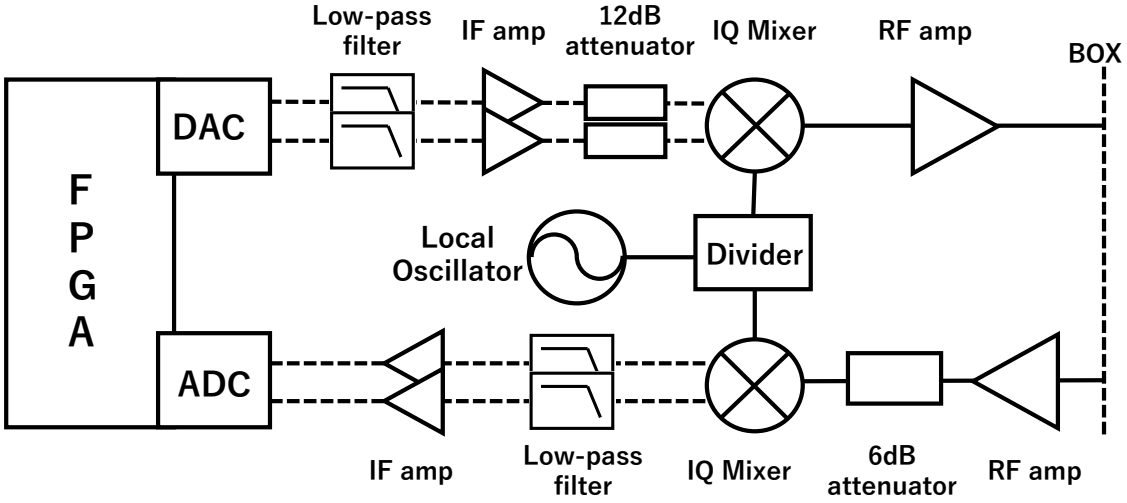

Figure 2.15: Diagram of the readout electronics for the MKID outside the cryostat as shown in Figure 2.14. Fed microwaves at a frequency below 100 MHz (IF signal) are generated/read with the Rhea (ADC/DAC) board and KCU105 (FPGA) board. Low pass filters reduce the unwanted analog signal at high frequencies (e.g. above 100 MHz). The microwaves are up-converted/down-converted with IQ mixers by using the microwaves at the frequency range of $\mathcal{O}(1)$ GHz (RF signal) generated by the local oscillator.

We confirmed that the noise levels of the readout system is well below the typical noise

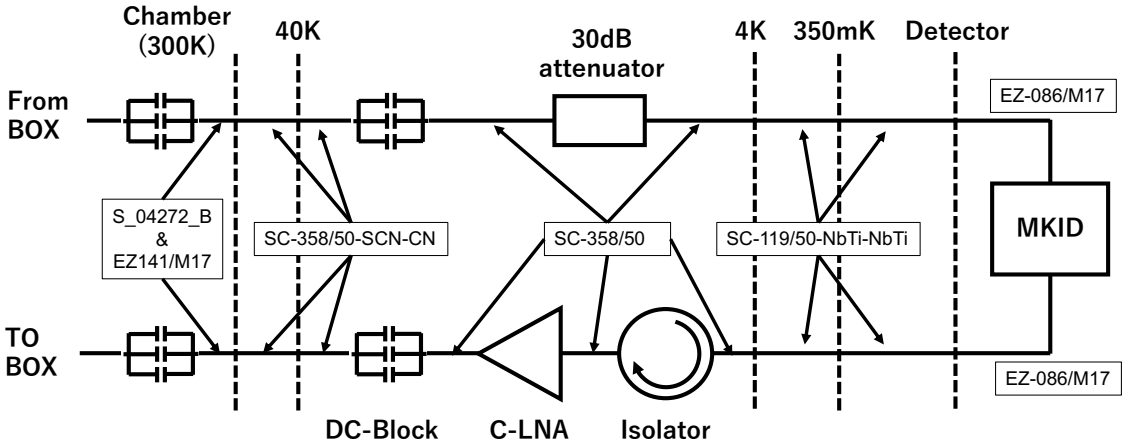

Figure 2.16: Diagram of the readout electronics inside the cryostat. We attenuate the thermal noise as well as the amplitude of the microwaves at 4 K circumstance with the 30 dB attenuator. The output microwaves from the MKID are amplified by a cold low noise amplifier to achieve a high signal-to-noise ratio.

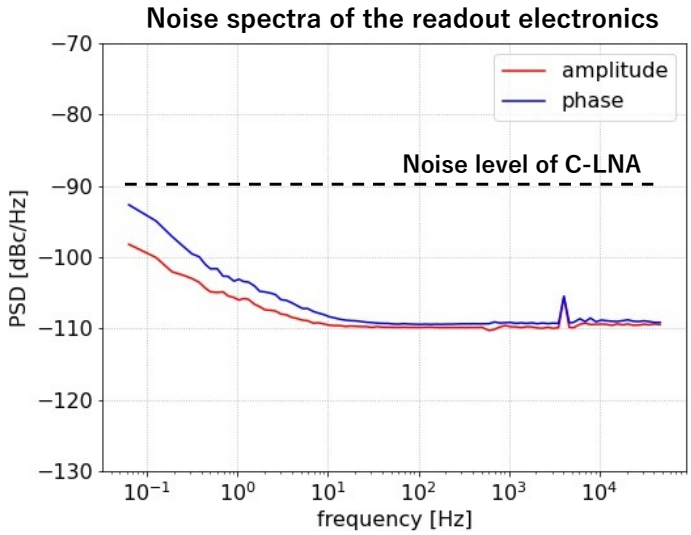

Figure 2.17: Power spectrum densities of the amplitude and phase responses in the loop-back condition. Both noise levels are low enough compared to the typical noise level of the C-LNA (-90 dBc/Hz).

level of the C-LNA (-90 dBc/Hz) as shown in Figure 2.17. Since the C-LNA is the first amplifier in the readout chain after the detector, we conclude that the noise is dominated by the C-LNA for the current setting.

2.4.2 Azimuth readout

The azimuth readout system is placed below the rotation table. An azimuth angle of the telescope is monitored with a magnetic rotary encoder (ERM220, HEIDENHAIN). The encoder signal is received at a sampling rate of 1 kHz with a commercial FPGA board (Spartan–3A, XILINX). A precision of azimuth angle is $5.7' \times 10^{-2}$ by using an interpolation method as described in [69].

2.4.3 Elevation readout

The elevation readout system is set on the rotation table. An elevation angle of the telescope is monitored with a laser rotary encoder (R–1SL, Canon). The encoder signal is received at a sampling rate of 1 kHz with a commercial FPGA board (ZYBO–Z7–20, Digilent Inc.). A precision of elevation angle is $6.6' \times 10^{-2}$.

2.4.4 Synchronization

Synchronization among these three readout systems is important because of our fast scanning observation. They are synchronized by using a common pulse clock every 1 second which is generated at the FPGA for the azimuth readout system. The pulse signal is distributed to the elevation readout system as well as the detector readout system. Based on the recorded time of the pulse signal for each readout system, we can synchronize them in offline analysis. The precision of the synchronization is 55 ns [69], which is small enough compared with the sampling rate of 1 kHz.

Chapter 3

Commissioning Observations

GroundBIRD performed commissioning observations from January to April of 2022 with the prototype detector arrays. By using the commissioning data, we developed calibration methods for the pointing and polarization angle. In addition, we studied the noise in the data. In this chapter, we describe the configuration of the focal plane at first. Then, we describe pre- and post-tunings of the detector readout. At the end of this chapter, we briefly introduce the Moon observation for the calibration and the CMB observation.

3.1 Focal plane configuration

We installed three detector arrays in the focal plane during the commissioning observations as shown in Figure 3.1

MKID array for 145 GHz The MKID array for 145 GHz was mainly used to take data during the commissioning observations. This array was developed by the Delft University of Technology (TU Delft) and the Netherlands Institute for Space Research (SRON). The design of the MKID array was almost the same as that for science observations.

MKID array for testing flexible coaxial cables This array served as a test bench for verifying the quality of flexible cables intended for use in the science observation.

MKID array used in previous commissioning This array was also fabricated by TU Delft and SRON. This is used for the first commissioning observations in 2019. However, it was not optimized for the GroundBIRD experiment (i.e., it was not optimized for the frequency band of either 145 GHz or 220 GHz). Therefore, we only used it for comparing with the previous commissioning observations.

We only use data taken by the first MKID array for 145 GHz in this thesis. This is because the second array was used only to test the flexible cable and the third array was not optimized for frequency bands of GroundBIRD.

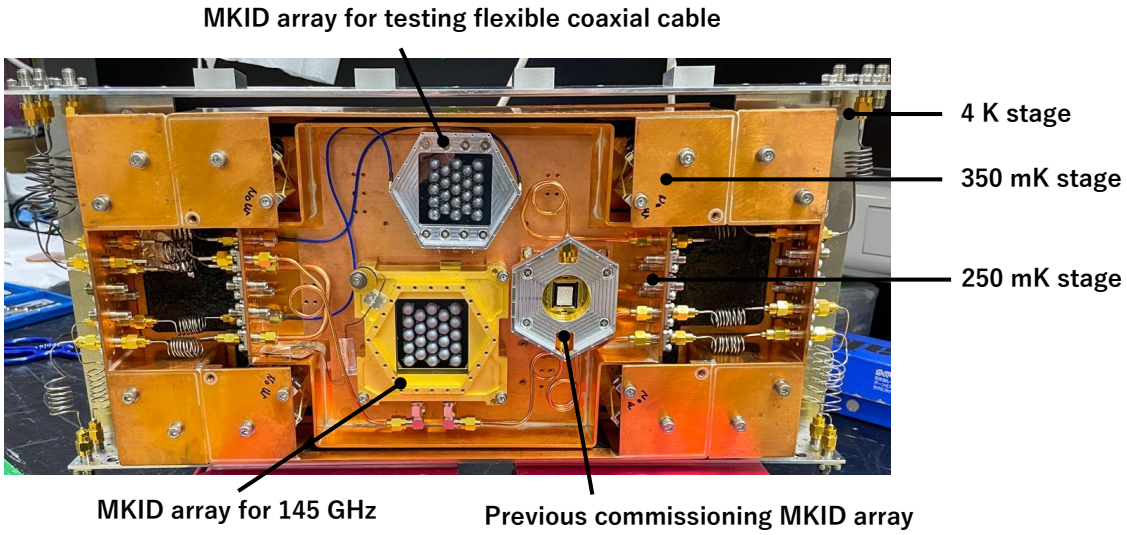

Figure 3.1: Photo of the focal plane during the commissioning observations. There are three MKID arrays; The MKID array for 145 GHz fabricated at TU Delft and SRON, The MKID array which is used for the first commissioning observation, The MKID array for testing flexible coaxial cables. I used data taken by the MKID array for 145 GHz (left bottom) for analysis in this thesis.

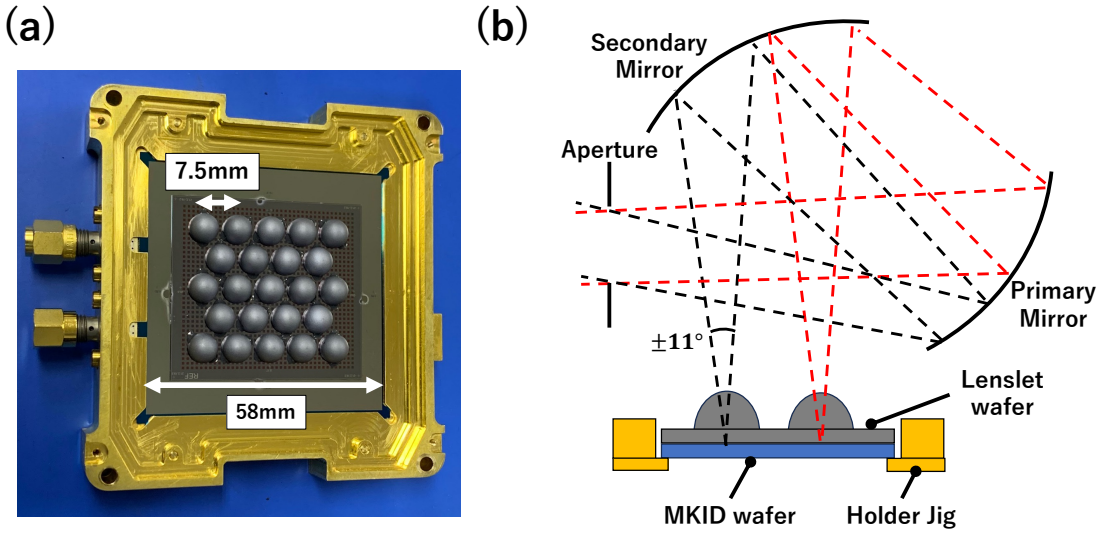

Figure 3.2: (a) Photo of the MKID array for 145 GHz [49]. (b) Illustration of the MKID array, the mirrors, and the aperture. The MKID array consists of the lenslet wafer, the MKID wafer, and the holder jig. Both wafers are fixed on the holder jig. We installed 23 Silicon lenslets on the lenslet wafer. We overlay their optical paths which are limited by ±11° due to the aperture.

3.2 Detector design

Figure 3.2 (a) shows a picture of the MKID array. This MKID array was designed and fabricated at TU Delft and SRON in the Netherlands. An MKID wafer and a lenslet wafer are mounted on a holder jig made from gold-coated oxygen-free copper. The outer dimensions of the MKID wafer are 58 mm squares. The Silicon lenslets which are used

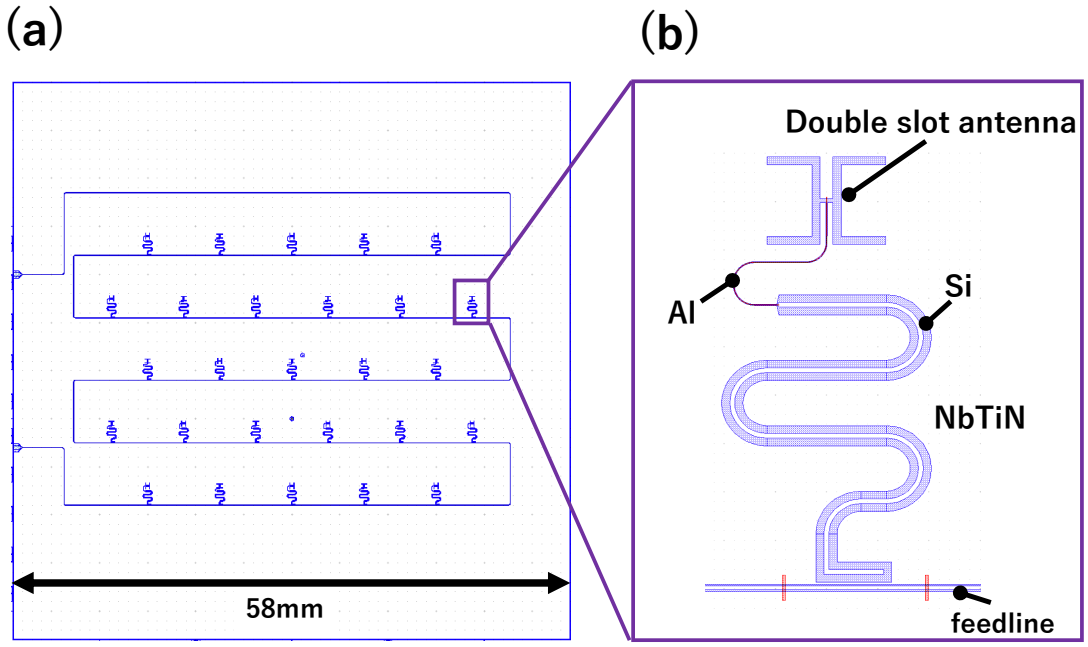

Figure 3.3: (a) Design of the MKID array. There are 27 MKIDs. 23 of them were used with the Si lenslets and 4 of them were used without the Si lenslets. We designed two antenna angles: parallel and perpendicular to the direction of detector alignment in turn. (b) Design of the MKID itself. The superconducting materials (i.e., Aluminium and NbTiN) are deposited on a Silicon substrate. We designed the geometry of the double slot antenna for the frequency band of 145 GHz. We also designed the geometry of the resonator to achieve high responsivity and low noise.

for focusing the CMB are placed in front of each antenna with 7.5 mm interval among the detectors. This interval in the MKID/lenslet array introduces the collimation interval in the sky as described in chapter 2.

As shown in Figure 3.3 (a), there are 27 MKIDs in the MKID wafer. 23 of them have the Silicon lenslets, while 4 of them do not have the Silicon lenslets. A design of each MKID is shown in Figure 3.3 (b). This MKID is designed based on the hybrid-type MKID. We deposited Aluminum (Al) and Niobium-Titanium-Nitride (NbTiN) as superconducting material on a Silicon substrate. The sensitive part of the resonator is designed by a narrow CPW made from NbTiN-Al-NbTiN. On the other hand, the coupling part of the resonator is designed by a wide CPW made from NbTiN-NbTiN-NbTiN. The transition temperature of Al is about 1.3 K. We use Al to detect the photon above the frequency of 100 GHz. The narrow CPW geometry for the sensitive part provides high responsivity. NbTiN has a high transition temperature (15 K) and low two level system (TLS) noise property [70]. The TLS noise is frequency-dependent noise, and it is higher at the lower frequency region. It is important to suppress the TLS noise so that it is negligible at a higher frequency region than the scanning frequency of GroundBIRD (i.e., 0.3 Hz). The magnitude of the TLS noise depends on materials and electric field density of the resonator. NbTiN has low TLS noise property [70]. The electric field density can be reduced by expanding the CPW

Table 3.1: Specifications of the MKID array.

Number of MKIDs	27
Number of Si lenslets	23
Length of resonator [mm]	5.057–5.274
CPW of the sensitive part(NbTiN-Al-NbTiN) [μm]	$2-2-2$
CPW of the coupling part (NbTiN-NbTiN-NbTiN) [μm]	$40-24-40$
Interval of each antenna in the MKID wafer [mm]	7.5
Typical collimation interval in the sky [arcmin]	51

geometry [71]. Thus, we designed the CPW of the coupling part to be as wide as possible. We assigned different lengths to each resonator. Their lengths are designed so that all resonant frequencies are within the readout bandwidth of GroundBIRD (200 MHz). We designed the center of the resonant frequencies to be about 4.5 GHz, which is suitable for our readout system.

We used a double slot antenna [72] which is a single-polarization sensitive antenna. We optimized its geometry for the frequency band of 145 GHz. In this array, we designed two types of antenna orientations alternately: parallel and perpendicular to a direction of detector alignment (i.e. horizontal direction in Figure 3.3 (a).) The orientation of the antenna defines the polarization angle of each detector in the sky. We describe the polarization angle in chapter 6.

We used hemispherical shape Silicon lenslets which are made in Miyoshi LLC. An optical path of the beam from the lenslet is limited by $\pm 11^\circ$ because of the aperture as illustrated in Figure 3.2 (b). We optimized the geometry of the lenslet with respect to the GroundBIRD optics as well as the frequency band of 145 GHz. We summarize the specification of the MKID array including the design parameters in Table 3.1.

3.3 Tuning of detector readout system

Figure 3.4 shows an observation routine for GroundBIRD. We wait for 1 hour after opening the dome and rotating the telescope because the detector temperature is changed due to different conditions (e.g., optical loading). Prior to taking time-ordered data (TOD), we need to identify each resonant frequency by changing the frequency of the fed microwaves. This measurement is called as “frequency sweep”. We perform the frequency sweep once an hour because the resonant frequency could change due to observation conditions (e.g., sky condition and detector temperature). After identifying the resonant frequency for each MKID, we take TODs with a sampling rate of 1 kHz for 1 hour. We have to stop observations when we regenerate the Helium sorption cooler at least once a day. We cannot perform observations when the Sun is located within the FoV of the GroundBIRD telescope as well.

3.3.1 Frequency sweep

Figure 3.5 shows a transmittance as a function of frequency at the detector temperature of 283 mK. We found 26 MKIDs within the readout bandwidth (200 MHz). We also found that 1 MKID outside the readout bandwidth.

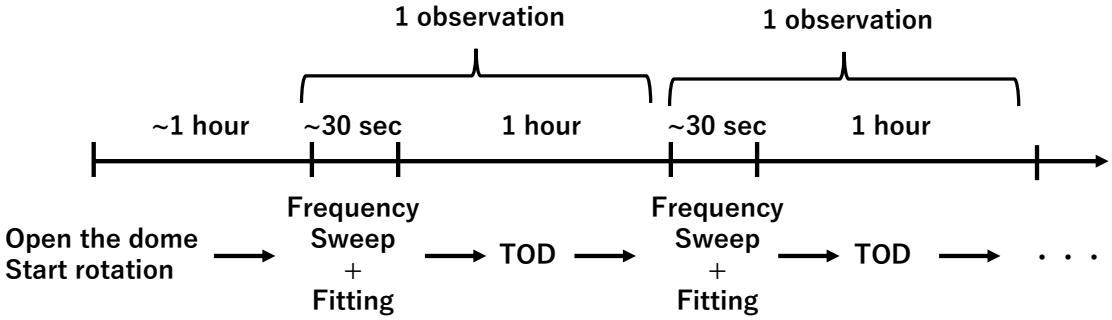

Figure 3.4: The observation routine for GroundBIRD. We need to wait for approximately 1 hour to stabilize the detector temperature. We perform a frequency sweep to identify the resonant frequency once an hour because it could be changed in time. After the frequency sweep, we take TODs for 1 hour.

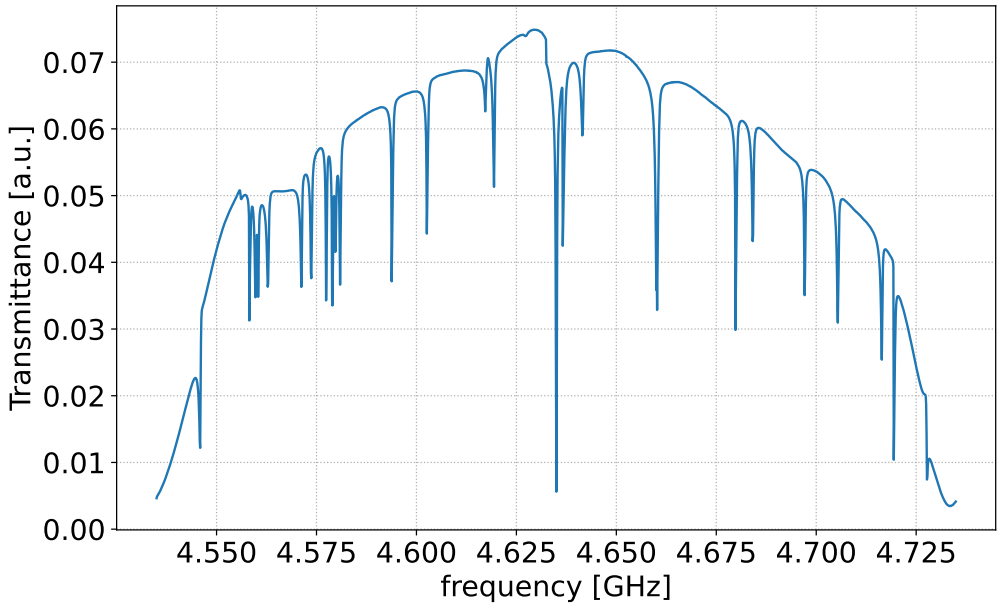

Figure 3.5: Transmittance as a function of frequency. 26 MKIDs were found within the bandwidth (200 MHz) of the GroundBIRD readout system. 1 MKID was also found outside the bandwidth.

3.3.2 Extraction of resonant frequencies

The resonant frequencies can be extracted by fitting the frequency sweep data after correction of a cable delay [74]. Figure 3.6 shows a comparison between extracted resonant frequencies and the design values. Resonant frequencies could be systematically shifted from the designed values because the resonant frequency would be affected by the variation in the thickness of the superconducting thin films. The scattering of the resonant frequency difference was about 0.4%. We achieved a 96% yield rate within the readout bandwidth thanks to the lower scattering of the resonant frequency.

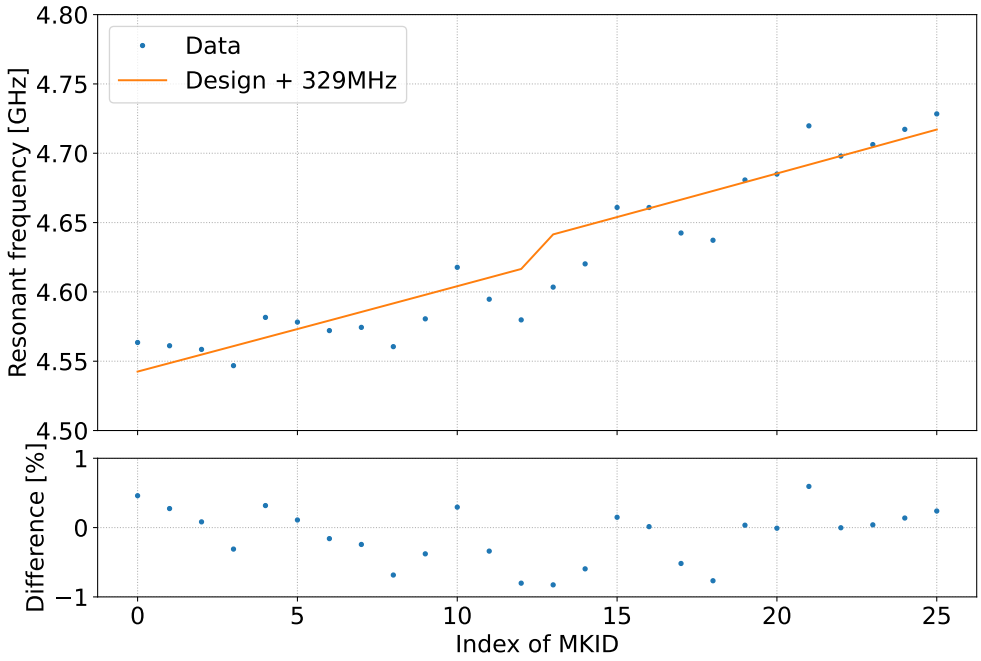

Figure 3.6: Comparison of resonant frequencies between data and the design. The scatter of difference in the resonant frequencies between the data and the design was about 0.4%.

3.4 Preprocessing to time-ordered data

3.4.1 Off-resonance subtraction

We take data at frequencies where there are no resonators as well. We call such a frequency as off-resonant frequency (e.g., 4.7 GHz in Figure 3.5). This data is used to subtract common noise unrelated to the MKID response (e.g. C-LNA) [73]. The noise unrelated to the MKID response affects TOD regardless of whether it is taken at the resonant frequency. We can reduce the effect by subtracting common-mode noise estimated from the data at the off-resonant frequency.

3.4.2 Corrections of phase delay and nonlinear effect

As shown in Figure 3.4, each observation has 1 hour time-ordered data (TOD). We measured the phase and amplitude responses at the resonant frequency with our readout electronics. We use the phase response of the resonance for the analysis because it has higher responsivity than that of the amplitude response [74]. The response is affected by the microwave phase delay owing to the cable length and data treatment in the FPGA board [75]. Figure 3.7 (a) shows an example of the phase response of the TOD and the frequency sweep. Prior to the analysis, we correct its effect based on the frequency sweep data [74]. We show the phase response after the correction of the phase delay in Figure 3.7 (b). In addition to the correction of the microwave phase delay, we correct the nonlinear

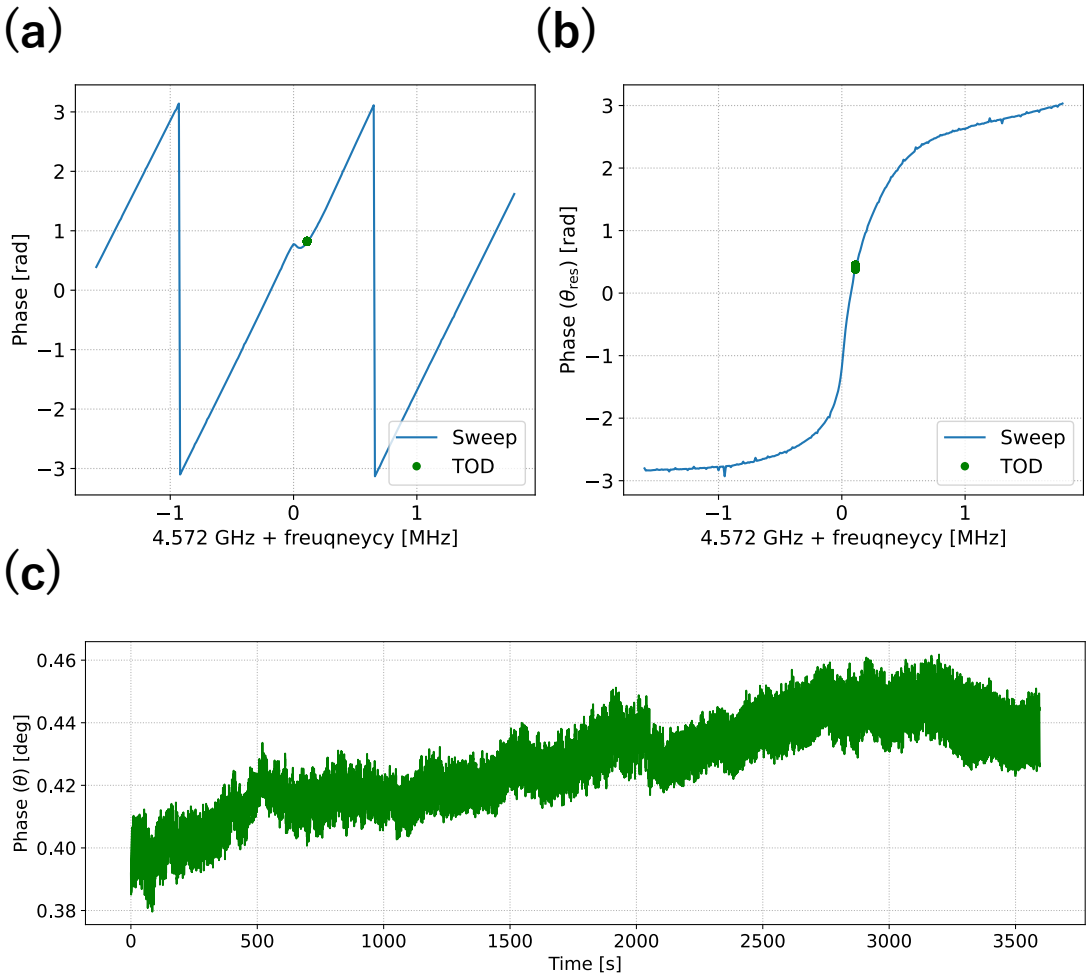

Figure 3.7: (a) Unprocessed phase response of the TOD for 1 hour which is taken with our readout electronics. We also show the phase response of the frequency sweep prior to taking the TOD. The measured phase is continuously changed due to the microwave phase delay. (b) The phase response ($\theta_{\rm res}$) of the TOD and the frequency sweep after the correction for the microwave phase delay. (c) The phase response (θ) after the correction for the nonlinear effect in addition to the microwave phase delay. We use this phase response for the analysis.

effect of the phase response ($\theta_{\rm res}$) by using the following formula [75],

$$\theta = 2\tan(\theta_{res}/2). \tag{3.1}$$

Figure 3.7 shows θ as a function of time after all corrections described in this section. We use θ for the analysis.

3.5 Commissioning observations

During the commissioning observations, we took two types of data: Moon observation data and continuous sky observation data.

Moon observations The Moon is one of the calibration sources for telescopes because the Moon is the brightest source outside the Earth except for the Sun. Although it is too bright to use as a calibrator for some telescopes, we can use the Moon as a calibrator because of a large dynamic range of the MKID and the large beam width (0.6°) of the GroundBIRD telescope. We can calibrate pointing by using the Moon as described in chapter 5. We observed the Moon from the 28th of February to the 12th of April. We took them by rotating the telescope at 10 RPM with a fixed elevation of 70°.

Continuous sky observation During CMB observations, we continuously observe the sky. We observed the sky continuously from 18:21 (UTC) on the 26th to 08:29 (UTC) on the 27th of April. We took it by rotating the telescope at 10 RPM with the fixed elevation of 70° as well. This observation is a demonstration of the CMB observations. By using these data, we can develop an analysis pipeline and characterize the noise property as described in chapter 7.

Chapter 4

Analysis Framework

We describe methodological overview about the data analysis as well as the sky coordinate systems.

4.1 Sky coordinate systems

In CMB analyses, the equatorial coordinate system or the galactic coordinate system is popular because the CMB anisotropies are invariable in these coordinate systems during the history of the human being. We characterize the CMB in either of them. On the other hand, these coordinate systems are not appropriate to characterize the telescope on the ground. Therefore, we also use the horizontal coordinate system for instrumental characterization such as the pointing calibration. In this thesis, we use the horizontal coordinate system and the equatorial coordinate system. For describing the study in this thesis, we explain the definition of them as well as their relation for transforming the observation data to each other.

4.1.1 Horizontal coordinate system

The horizontal coordinate system is based on the zenith and the meridian which is a great circle that passes the north and the south. A point in the horizontal coordinate system is represented by using two parameters: azimuth and elevation angles as shown in Figure 4.1 (a). The azimuth is an angle[1] from the north. The elevation is an angle from the horizon plane to the zenith. The horizontal coordinate system is used for characterizing the ground-based telescopes because their location is always center. However, we have to take into account the fact that locations of CMB and astronomical sources are moving along the time in the horizontal coordinate system.

4.1.2 Equatorial coordinate system

The equatorial coordinate system is based on the north celestial pole and the celestial equator. The north celestial pole is defined as a crossing point between the axis of the Earth rotation and the celestial sphere. The celestial equator is a plane perpendicular to the axis of the Earth rotation. A point in the equatorial coordinate system is represented

[1] This is not a left-handed coordinate system but a right-handed coordinate system

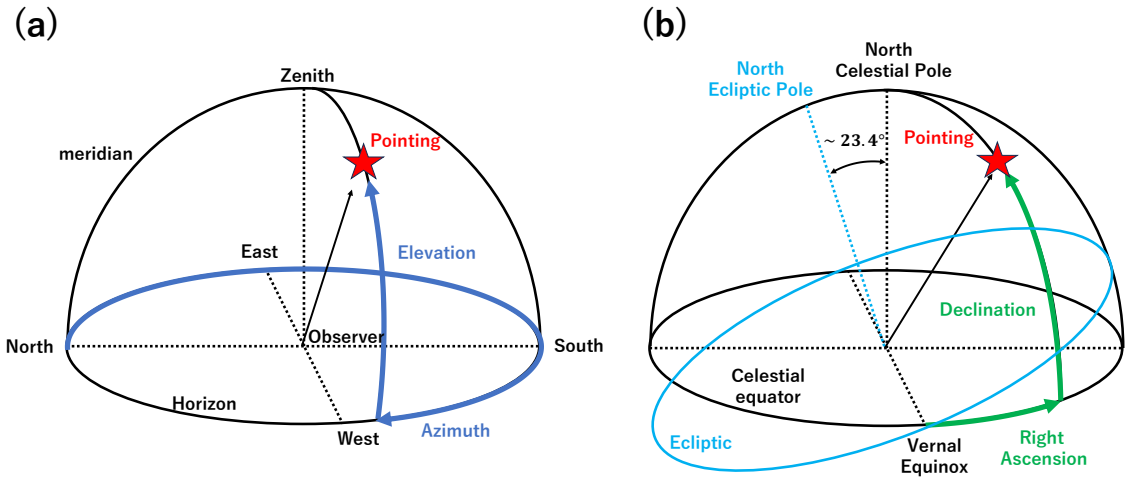

Figure 4.1: (a) Illustration of the horizontal coordinate system. The horizontal coordinate system is based on the zenith and the meridian of the observer. A point in the horizontal coordinate system is characterized by azimuth and elevation. (b) Illustration of the equatorial coordinate system. The equatorial coordinate system is based on the celestial equator and the north celestial pole. A point in the equatorial coordinate system is characterized by right ascension and declination.

by using two parameters: declination and right ascension angle as shown in Figure 4.1 (b). The right ascension is an angle from the vernal equinox which is a crossing place between the celestial equator and the ecliptic. Its direction is opposite to the azimuth. The declination is an angle from the celestial equator. The equatorial coordinate system is used for characterizing locations of CMB and astronomical sources because their locations are invariable.

4.2 Relation of coordinate systems

The polarization angle depends on the pointing as well as the coordinate system. As introduced in section 4.1, the horizontal coordinate system and the equatorial coordinate system are popular to use. In this section, their relationship and other coordinate systems are described.

4.2.1 Relation between the Horizontal coordinate system and the Equatorial coordinate system

The relationship between the horizontal coordinate system and the equatorial coordinate system is illustrated in Figure 4.2 [76]. The point in the horizontal coordinate system is represented by azimuth (A) and elevation (E), and the point in the equatorial coordinate system is represented by right ascension (α) and declination (δ). Using the latitude (ϕ) and the longitude (λ) of the observer, the Greenwich sidereal time (Θ), and the hour angle ($H \equiv \Theta + \lambda - \alpha$) as shown in Figure 4.3, the relation of the coordinate systems is

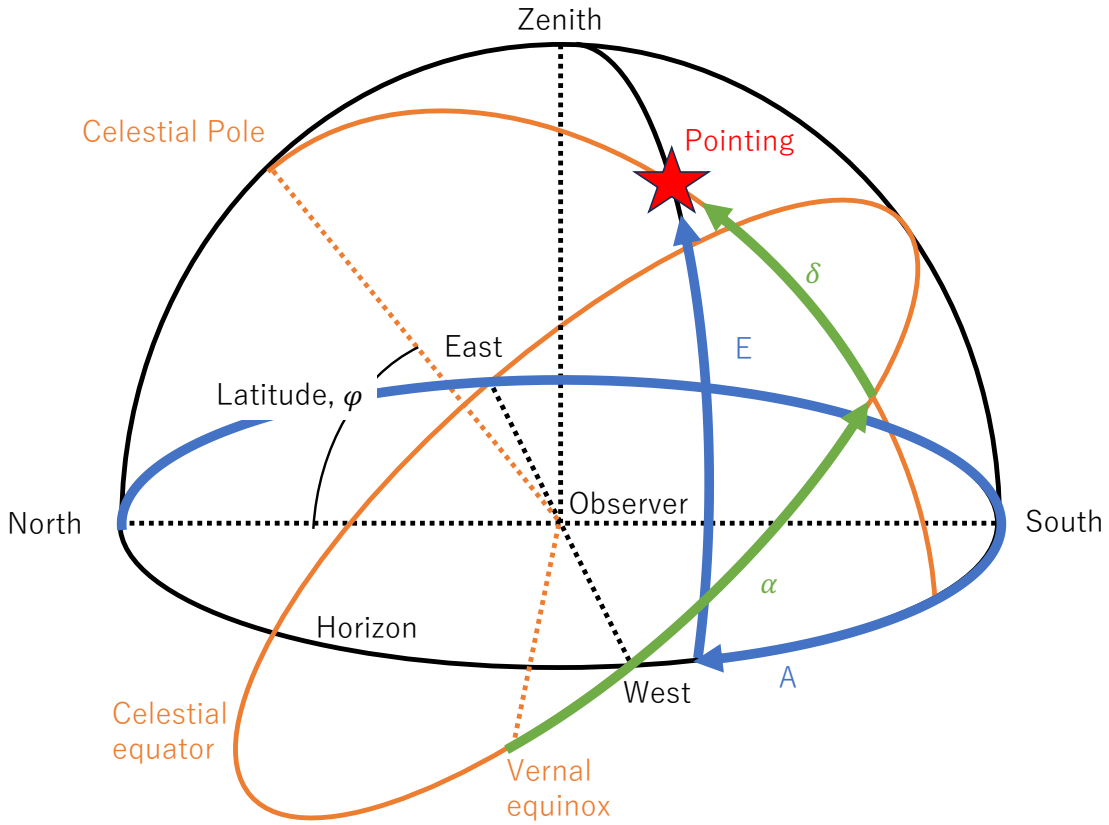

Figure 4.2: Relationship between the horizontal coordinate system (black) and the equatorial coordinate system (orange). The horizontal coordinate system is described in the elevation angle (E) from the horizon and azimuth angle (A) from the north to clockwise. On the other hand, the equatorial coordinate is described in declination (δ) from the celestial equator and right ascension (α) from the vernal equinox. Translation from horizontal coordinate to general equatorial coordinate system (e.g. FK5, ICRS) has to take precession, nutation, and polar motion into account as described in the text.

formulated as follows,

$$\begin{cases} \cos E \sin A = -\cos\delta \sin H, & \text{(4.1a)} \\ \cos E \cos A = \cos\phi \sin\delta - \sin\phi \cos\delta \cos H, & \text{(4.1b)} \\ \sin E = \sin\phi \sin\delta + \cos\phi \cos\delta \cos H. & \text{(4.1c)} \end{cases}$$

4.2.2 Other coordinate systems

An ecliptical coordinate system and the galactic coordinate system are also popularly used in the CMB analysis. The ecliptical coordinate system is based on the north ecliptic pole and the ecliptic, and the galactic coordinate system is based on the Galactic (Milky Way) plane and a pole perpendicular to the galactic plane. The pointing in the ecliptical coordinate system is also calculated from pointing in the equatorial coordinate system at

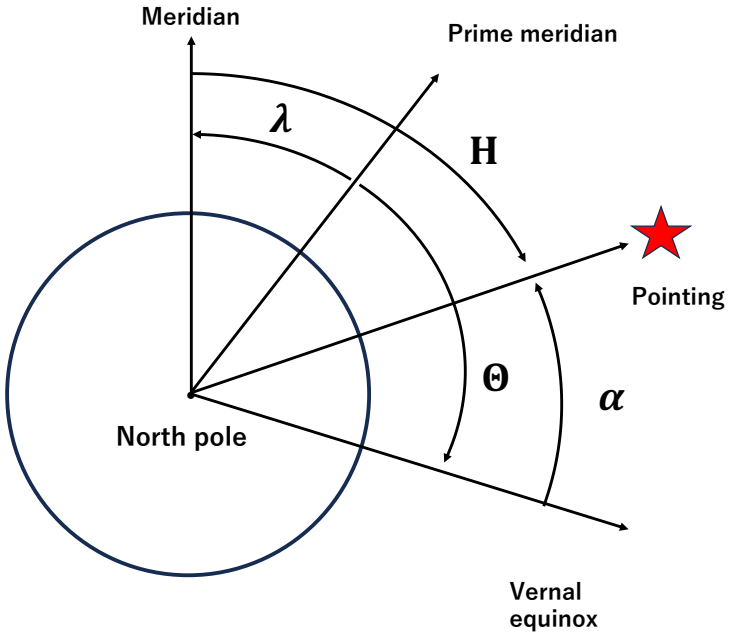

Figure 4.3: Relationship of the right ascension (α), the longitude (λ), the Greenwich sidereal time (Θ), and the hour angle (H).

the same epoch by using the following rotation matrix [76],

$$\begin{pmatrix} \cos\beta_{lat}\cos\lambda_{lat} \\ \cos\beta_{lat}\sin\lambda_{lat} \\ \sin\beta_{lat} \end{pmatrix} = R_1(\epsilon) \begin{pmatrix} \cos\delta\cos\alpha \\ \cos\delta\sin\alpha \\ \sin\delta \end{pmatrix}, \tag{4.2}$$

where β_{lat} and λ_{lat} are latitude and longitude in the ecliptic coordinate system. R_1 is the rotation matrix about x axis. It is defined as follows,

$$R_1(\theta) \equiv \begin{pmatrix} 1 & 0 & 0 \\ 0 & \cos\theta & \sin\theta \\ 0 & -\sin\theta & \cos\theta \end{pmatrix}. \tag{4.3}$$

ϵ is the obliquity of the ecliptic ($\epsilon \sim 23.4^\circ$).

The pointing in the galactic coordinate system is also calculated from pointing in the equatorial coordinate system at the epoch of J2000.0, Julian year, which is defined as time at noon (GMT), 1st of January, 2000. Their relation is defined by using the following rotation matrix,

$$\begin{pmatrix} \cos b_{gal}\cos l_{gal} \\ \cos b_{gal}\sin l_{gal} \\ \sin b_{gal} \end{pmatrix} = R_{equ\_to\_gal} \begin{pmatrix} \cos\delta\cos\alpha \\ \cos\delta\sin\alpha \\ \sin\delta \end{pmatrix}, \tag{4.4}$$

where b_{gal} and l_{gal} are latitude and longitude in the galactic coordinate system. $R_{equ\_to\_gal}$ is a rotation matrix of pointing vector from the equatorial coordinate system to the galactic coordinate system as follows [77],

$$R_{equ\_to\_gal} = R_3(90^\circ - \theta_{gal})R_1(90^\circ - \delta^P)R_3(90^\circ + \alpha^P), \tag{4.5}$$

where α^P and δ^P are the north galactic pole in the equatorial coordinate system, and θ_{gal} is the position angle of the Galactic center at the north galactic pole with respect to the equatorial pole. In FK5 (J2000.0) system which describe in section 4.2.3, their numerical values are

$$\begin{aligned} \alpha^P &= 12^h51^m26^s.2755, \\ \delta^P &= +27°7'41''.704, \\ \theta_{gal} &= 122°.93191857. \end{aligned} \tag{4.6}$$

R_3 is the rotation matrix about z axis, which is defined as follows,

$$R_3(\theta) \equiv \begin{pmatrix} \cos\theta & \sin\theta & 0 \\ -\sin\theta & \cos\theta & 0 \\ 0 & 0 & 0 \end{pmatrix}. \tag{4.7}$$

4.2.3 Motion of the Earth rotation axis

The Earth axis of the rotation varies because of motions in the solar system. Because that motion changes the vernal equinox and the celestial equator, the basis of the equatorial coordinate system is changed. Therefore, we have to define its basis for making the CMB map. In particular, this is important to compare with maps made by other experiments. There are three types of motions.

- Precession: The precession of the Earth axis is a long-term ($\mathcal{O}(1000)$ years) effect caused by gravity from the Moon and other planets.
- Nutation: The precession of the Earth axis is a short-term ($\mathcal{O}(10)$ years) effect caused by gravity from the Moon and other planets.
- polar motion (wobble): The polar motion includes all effects except for the precession and the nutation (e.g., Chandler wobble).

The precession of the axis is a dominant source of them. If we consider only the precession, the vernal equinox and the celestial equator are called the "mean" vernal equinox and "mean" celestial equator. On the other hand, if we consider both the precession and the notation, the vernal equinox and the celestial equator are called "true" vernal equinox and "true" celestial equator. Besides, we have to fix an epoch to calculate the change of the Earth axis. Therefore, it has to be written explicitly which (i.e. mean or true) and when axes are used.

The equatorial coordinate system refers to a reference frame based on astronomical observations (e.g. star catalog). There are two types of reference frames.

- FK5 : Fundamental Katalog 5 (FK5) is based on optical observation [78]. An equatorial coordinate referred to as FK5 (hereafter called FK5 system) is one of the common coordinate systems, which is based on the mean vernal equinox and the mean celestial equator at the epoch of J2000.0.
- ICRF: International Celestial Reference Frame (ICRF) is based on radio observation [79]. The International Celestial Reference System (ICRS) is one of the famous

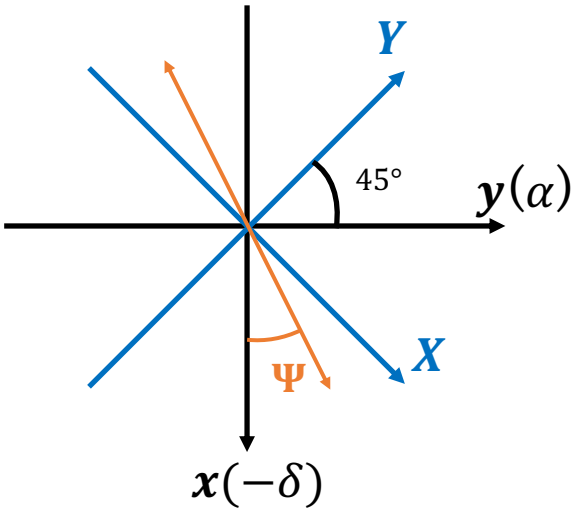

Figure 4.4: Definition of the Stokes parameters in the Healpix convention [51]. In the equatorial coordinate system (FK5), x and y axes correspond to $-\delta$ and α, respectively. X and Y axes are rotated by 45° from x and y axes. The polarization angle (Ψ) is defined as an angle from the x axis.

reference systems referred to as the ICRF which was adopted at the International Astronomical Union's conference in 1998 [80]. ICRS does not depend on the motion of the Earth axis because it is realized by only ICRF at an inertial frame. Therefore, we do not need to mention the epoch if we used ICRS.

In this paper, we use the FK5 system as the equatorial coordinate system because this is popularly used in the CMB experiments [81]. As described in this section, we need to take into account the precession, the nutation, and the polar motion to convert the pointing in the horizontal coordinate system to that in the FK5 system. Furthermore, we also take aberration into account for the conversion.

4.3 Stokes parameters

We categorize the detected signal as polarized or unpolarized components. We introduce "Stokes parameters" to describe them. The Stokes parameters consist of four parameters: I, Q, U, and V. Intensity of unpolarized signals is represented as I. For polarization, Q and U represent intensities of linear polarization, and V represents intensity of circular polarization. We define the x–y and X–Y coordinates as illustrated in Figure 4.4. The X-Y coordinate is rotated by 45° from the x-y coordinate. In these coordinates, the Stokes parameters are described as follows,

$$\begin{cases} I = E_x^2 + E_y^2 = E_X^2 + E_Y^2, & \text{(4.8a)} \\ Q = E_x^2 - E_y^2, & \text{(4.8b)} \\ U = 2E_xE_y \sin\Delta = E_X^2 - E_Y^2, & \text{(4.8c)} \\ V = 2E_xE_y \cos\Delta, & \text{(4.8d)} \end{cases}$$

where E_i is electrical field along i axis ($i = x, y, X, Y$). Δ is the phase difference between the electrical fields along x and y axes. Q and U are defined as the intensity difference between x and y axes and X and Y axes, respectively. V is the intensity difference between right and left circular polarization which is negligible. The polarization angle is defined as $\Psi \equiv \frac{1}{2} \arctan \frac{U}{Q}$.

4.4 Analysis pipeline

In CMB analysis, we make I, Q, and U maps by using time-ordered data (TOD) with applying calibrated pointing and polarization angle information. Then, we estimate power spectra from the maps. We make efforts to filter out the noise effects before making the maps. The anisotropy of the CMB is also smeared during the filtering process. Therefore, we need to develop appropriate filtering methods which keep efficiency for the CMB whereas highly suppress the noise. To develop the filtering methods, we evaluate the loss of the CMB power in the spectra by using "transfer function" (see section 4.4.5). We explain the data analysis flow in Figure 4.5. To obtain the cosmological parameters, we need to perform real data analysis and validation with simulated TOD. Hereafter, we describe each data analysis process.

4.4.1 Data selection

We could have bad-quality data (e.g., bad weather conditions). It is important to remove them at least before the map making process. Criteria of data selection are individual for each experiment. We generally perform it as the first step in the data analysis. For the GroundBIRD experiment, we take data about PWV, temperature, humidity, and infrared sky images [82] during observations. We plan to develop data selection based on these data in the future.

4.4.2 Applying calibrations

To reconstruct the map from TOD, we need to calibrate the pointing, polarization angle, and responsivity for each detector. Each calibration is performed by using an individual method (e.g. by using planets).

The responsivity for each detector has individual gain. In addition, their responses are expressed in units of measured value (e.g., radians for MKIDs) rather than in units of Kelvin. We need to convert each detector response to that in units of Kelvin. We generally perform it by using astronomical sources whose intensity is well measured by previous experiments.

We generally know only encoder's values in the elevation and azimuth, we have to calibrate pointing for each detector. This is also performed by using astronomical sources which we can calculate their position precisely.

We cannot reconstruct the polarized maps (Q and U) without the polarization angle information. We generally know only designed antenna orientations in the wafer or simulated angles by using commercial simulation software (e.g., LightTools). We need to calibrate the polarization angle for each detector. We generally perform it by using known polarized responses (e.g., polarized astronomical sources).

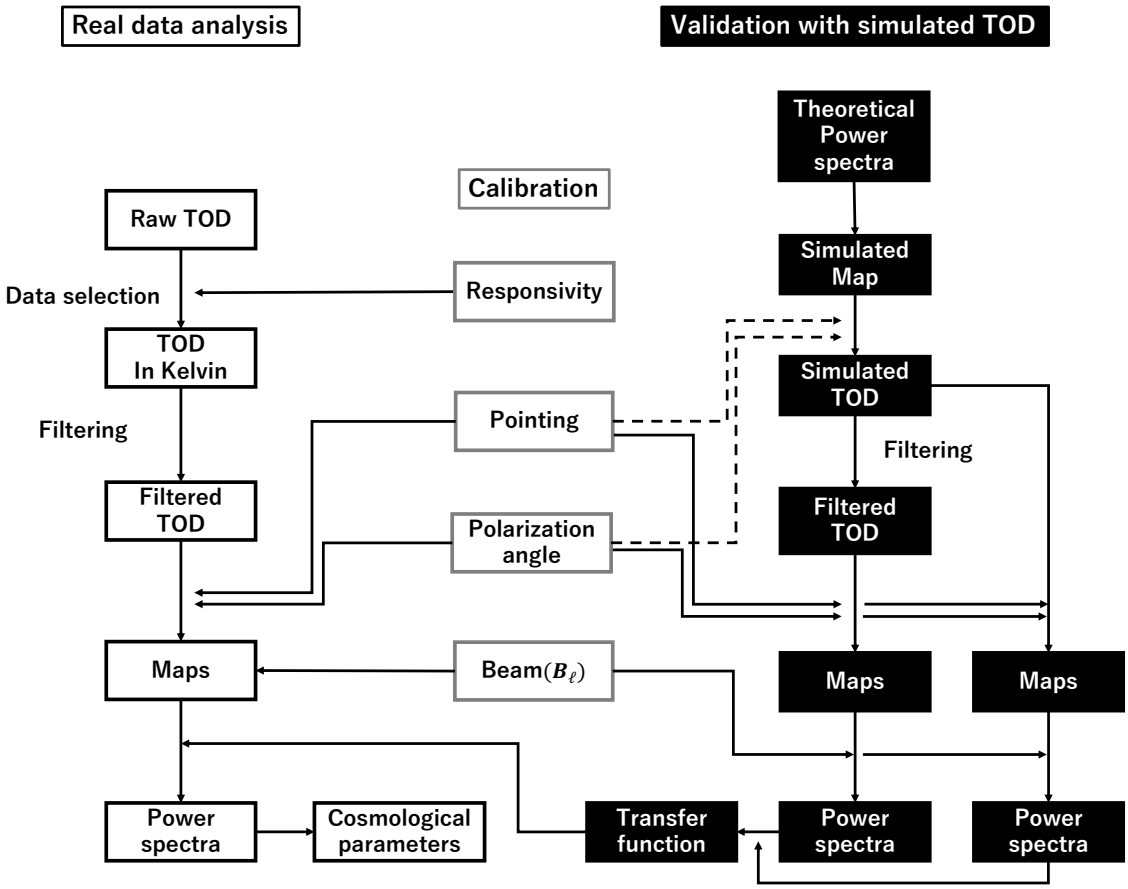

Figure 4.5: Overview of data analysis flow. At first, we apply data selection to "Raw TOD" (raw data). Then, we calibrate the responsivity for each detector. In this process, we convert the units to Kelvin from MKID's response. We apply filters to TOD for suppressing the noise effects. The I, Q, and U maps are obtained from the filtered TOD with the pointing and polarization angle information. To estimate power spectra from the maps, we need to validate a transfer function and a beam window function (B_ℓ). The beam window function is calculated from the calibrated beam information. We validate the transfer function by using simulated TOD which includes only CMB signal. In the simulation, we make simulated maps based on the theoretical power spectra. These maps are smeared by the beam. Using the same pointing and polarization angle information as real data analysis, we generate simulated TOD. We then apply the same analysis processes (filters, map-making, power spectrum estimation) as real data analysis. We also calculate power spectra without the filtering process. We evaluate the transfer function by comparing these two power spectra. We estimate the power spectra by using the transfer function and the beam window function (B_ℓ).

In chapters 5 and 6, we describe the pointing calibration and the polarization angle calibration respectively in detail.

4.4.3 Filtering

The obtained TOD includes the noise as well as the CMB. Because the CMB anisotropy is too faint, the TOD is dominated by the noise. To suppress the noise, we apply filters to

the TOD. We defined TOD after applying the filters as "Filtered TOD" in Figure 4.5 The filters also smear the CMB anisotropy. Thus, we have to use appropriate filters which keep efficiency for the CMB whereas highly suppress the noise. The efficiency for the CMB is evaluated by the transfer function as described in section 4.4.5.

4.4.4 Map-making

After applying the calibration results in addition to the data selection, we reconstruct maps from TOD. We write the TOD as

$$\boldsymbol{y} = \mathbf{P}\boldsymbol{m} + \boldsymbol{n}', \tag{4.9}$$

where $\boldsymbol{m}$ are the maps including Stokes I, Q, and U, and pointing matrix $\mathbf{P}_m$ spreads it into TOD ($\boldsymbol{y}$). $\boldsymbol{n}'$ is noise. We used MADAM library [83, 84] to reconstruct "binned map" from TOD. The binned map is defined as follows [84],

$$\boldsymbol{m} = \left(\mathbf{P}_m^T \mathbf{C}_n^{-1} \mathbf{P}_m\right)^{-1} \mathbf{P}_m^T \mathbf{C}_n^{-1} \boldsymbol{y}, \tag{4.10}$$

where $\mathbf{C}_n$ is a white noise covariance matrix which is calculated from the white noise component ($\boldsymbol{n}$) in the noise ($\boldsymbol{n}'$) as $\mathbf{C}_n = \langle \boldsymbol{n}\boldsymbol{n}^{\boldsymbol{T}} \rangle$. The reconstructed maps are represented in spherical coordinates with the parameter $N_{\mathrm{side}} = 128$ by using healpy, which is a python library. Its angular resolution is 0.46° which is slightly smaller than our beam width (0.6°). This resolution allows us to calculate power spectra at multipole lower than that corresponds to our beam width.

4.4.5 Transfer function

We evaluate the transfer function by using simulated TOD which includes only CMB signal. At first, we simulate CMB maps based on the theoretical power spectra. These maps are smeared by the beam. Then, we generate simulated TOD by using the same calibrated pointing and polarization angle as real data analysis. The simulated TOD (y) is

$$y = I(i) + Q(i)\cos(2\Psi) + U(i)\sin(2\Psi), \tag{4.11}$$

where (Ψ) is the polarization angle, i is a pixel index of the maps. We obtain power spectra by applying the same analysis processes (filters, map making, power spectrum estimation) to the simulated TOD. We also obtain power spectra without any filtering as references. We evaluate the transfer function by comparing these power spectra.

4.4.6 Power spectrum estimation

We estimate power spectra from the obtained maps based on a MASTER (Monte Carlo Apodized Spherical Transform EstimatoR) technique [85]. We calculate the pseudo-power spectra from the obtained maps. The filtering, the partial sky coverage of the maps, and a limited beam resolution introduce biases of the pseudo-power spectra. Based on the MASTER technique, we estimate an unbiased binned power spectrum (C_q) from a binned pseudo-power spectrum ($\widetilde{C_q}$). The binned pseudo-power spectrum is calculated from a

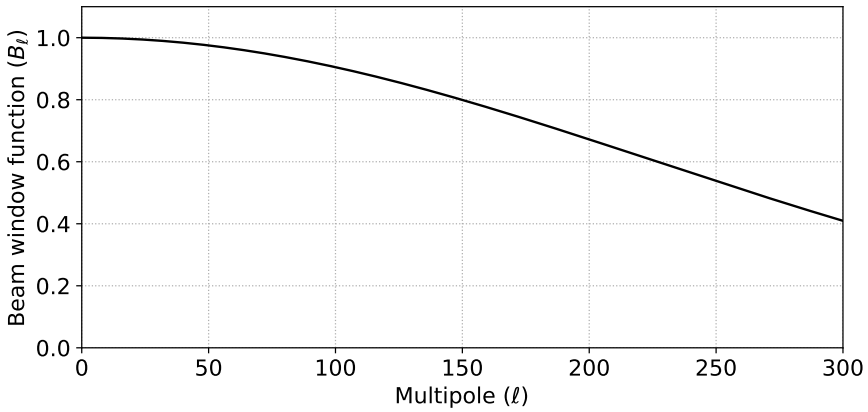

Figure 4.6: Beam window function for the beam width of 0.6° at $\ell \leq 300$. $\ell = 300$ corresponds to the beam width of 0.6°.

pseudo-power spectrum ($\widetilde{C_\ell}$) by using binning weights (w_q^ℓ),

$$\widetilde{C_q} = \sum_{\ell \in \vec{\ell_q}} w_q^\ell \widetilde{C_\ell} \ . \tag{4.12}$$

We use the same weighing for each multipole (i.e., $w_q^\ell = 1/\Delta\ell$). $\Delta\ell$ is a bin width. C_q and $\widetilde{C_q}$ are related as follows,

$$F_q \langle C_q \rangle + \langle N_q \rangle = \sum_{q'} (\mathcal{M})^{-1}_{qq'} \left\langle \widetilde{C_{q'}} \right\rangle , \tag{4.13}$$

where $\mathcal{M}$ is a binned coupling matrix, N_q is a noise bias (i.e., noise power spectrum). In case the TOD is dominated by the noise, we approximate the left-hand side of this equation as $F_q \langle C_q \rangle + \langle N_q \rangle \approx \langle N_q \rangle$. The binned coupling matrix is

$$\mathcal{M}_{qq'} = \sum_{\ell \in \vec{\ell_q}} \sum_{\ell' \in \vec{\ell'_q}} w_q^\ell M_{\ell\ell'} B_{\ell'}^2 . \tag{4.14}$$

where $M_{\ell\ell'}$ is the mode-mode coupling kernel which represents the bias due to the partial sky map. It also includes the bias from pixel weighting which is used to estimate the psuedo-power spectra. We can calculate it analytically [85]. B_ℓ is the beam window function which represents the bias due to the limited beam resolution. We assumed detector beam width (FWHM) of 0.6° which is the designed value as described in chapter 2. Under the symmetric Gaussian beam, the beam window function is calculated by using the following formula [87],

$$B_\ell = e^{\frac{-\ell(\ell+1)(\sigma_b/\sqrt{8\log_2 2})^2}{2}}, \tag{4.15}$$

where σ_b is the beam width. Figure 4.6 shows the beam window function for the beam width of 0.6°. After estimating the unbiased power spectra, we can extract the cosmological parameters from them.

We use the NaMaster library to estimate the binned power spectrum [86]. We focus on the EE power spectrum in this study because E-modes is our primary target. We estimate

the binned power spectrum with the bin width ($\Delta\ell$) of 10 within $52 \leq \ell \leq 301$. A higher multipole region is limited by the beam width (0.6°). At a lower multipole region ($\ell \leq 51$), we did not estimate the power spectrum well. We suspect that the binned mode-mode coupling kernel did not work well for our configurations (e.g., limited sky coverage). We have to develop new algorithm, which can estimate the power spectrum without bias even at low multipole in the future.

Chapter 5

Pointing Calibration using the Moon

Pointings of each detector in the sky coordinate system have intervals each other as described in section 2.2. We only know the elevation and azimuth angle of the telescope taken by their encoders. For making CMB maps from time-ordered data (TOD), we have to calibrate the pointing of each detector.

5.1 Why did we choose the Moon? Pros and Cons

In previous CMB experiments [88, 89, 90], they primarily used planets such as Jupiter as calibration sources. Given their small visible size compared with the large beam widths of CMB telescopes, the planets can be safely considered point-like sources. Their location in the sky can be calculated precisely by using `astropy`, which is a python library for astronomical calculations [91, 92]. There are pros and cons to using the planets for pointing calibration.

- Pros :
  - We do not need to consider possible nonuniformity of their brightness.
  - There are some individual candidates (e.g., Jupiter, Saturn, Venus).
- Cons :
  - It is difficult to detect them with a high signal-to-noise ratio. This is because their visible intensity is smeared by the angular resolution of the telescope. Thus, they are faint signals in general. Even though we used Jupiter, which is the brightest of the point sources, telescopes whose beam width is sub-degrees need to accumulate data to identify its position. This data accumulation for a long time introduces additional noise (e.g., 1/f type noise which is a noise depending on the time).
  - Sometimes, we cannot observe them for long periods because their evolution is $\mathcal{O}(10)$ years.

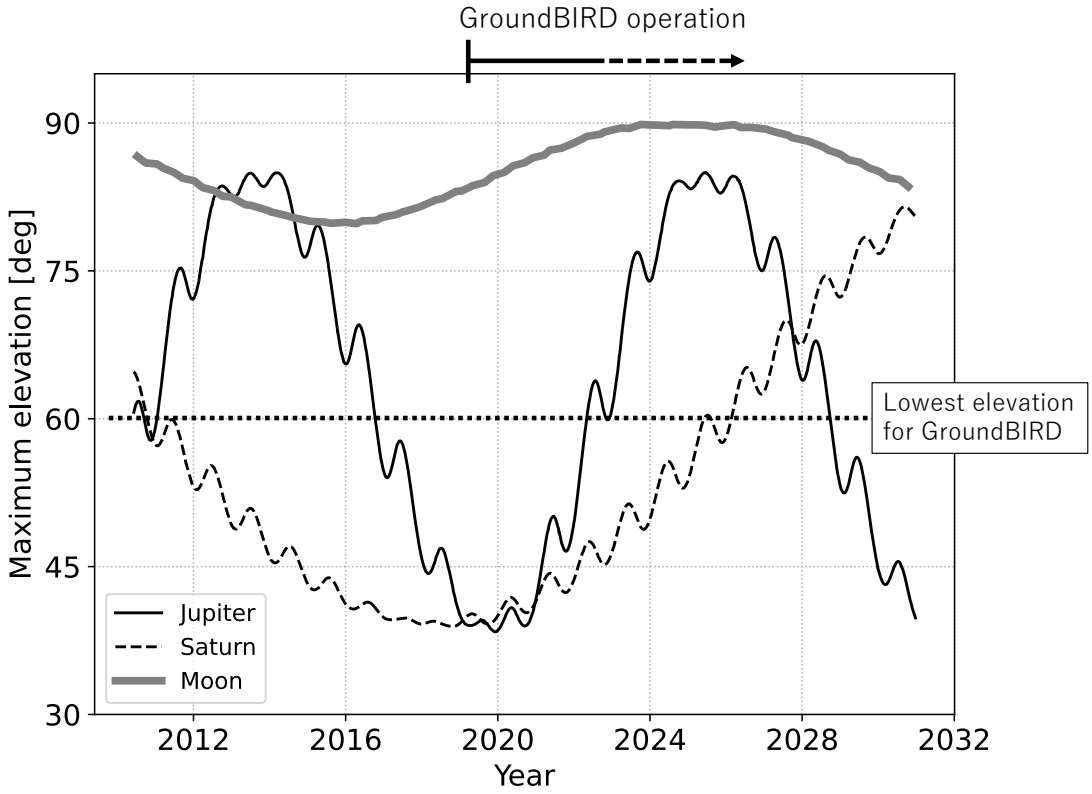

Figure 5.1: Maximum elevations of Jupiter, Saturn, and the Moon between 2011 and 2031 at the Teide Observatory in the Canary Islands, Spain. The orbital periods of Jupiter and Saturn are 12 years and over 20 years, respectively. In the years around 2020, their maximum elevations were lower than 60°. Thus, GroundBIRD cannot observe these plants during the periods. However, the Moon has always had a high elevation throughout these years [49].

For ground-based CMB experiments, the previous study achieved a ratio of pointing accuracy to their beam width is 0.13–0.14 [89, 93] This is because the pointing error is related to the beam width and leads to a smearing of the beam. Again, the beam is defined as the telescope response in relation to the angle from the pointing direction. We represent the angular resolution as the beam width, which is the full width at half maximum (FWHM).

Jupiter and Saturn are popular pointing calibration sources for observations in the millimeter-wavelength range. Their visible sizes are typically ($0.2' \sim 0.3'$). These are sufficiently small compared with the beam width, which is typically $1'$–$1°$ for CMB experiments. Their maximum elevation varies periodically on the order of 10 years as shown in Figure 5.1. They cannot be observed when their maximum elevation is lower than the lowest elevation of the telescope. GroundBIRD faced this difficulty during the commissioning observations because the lowest elevation of the GroundBIRD is 60°. Although Mars and Venus are other candidates as a calibrator, it is difficult to use because their location in the sky is close to the Sun. In addition, these planets (i.e., Jupiter, Saturn, Mars, and Venus) are not sufficiently bright to observe at high signal-to-noise ratios be-

cause of the larger beam width of the GroundBIRD telescope (i.e. 0.6°). The maximum brightness of known non-planets listed in the Planck Catalogue of Compact Sources (i.e., TauA) is $\leq 1/10$ that of Jupiter and Venus [94]. Therefore, we need another candidate as a calibrator for pointing calibration.

The Moon is a potential astronomical source for pointing calibration. GroundBIRD can observe the Moon frequently at least once a month. Its visible size is $30'$ (i.e., 0.5°). Its brightness temperature ($\sim$ 200 K) is sufficiently bright to observe with a high signal-to-noise ratio. The measurement with the high signal-to-noise ratio avoids the additional noise related to the data accumulation for a long time. Recently, in the CLASS experiment, the Moon was used as a calibrator for pointing calibration [95] because the beam width was sufficiently larger (i.e., 1.5°) than the visible size of the Moon. The beam width of the GroundBIRD telescope ($36'$) is slightly larger than the Moon's visible size. In addition, the dynamic range of the detector response is sufficiently large to measure the Moon signal. Therefore, we can use Moon observation data for pointing calibration. The effect of nonuniformity of the Moon's surface owing to the not-point source is discussed in Section 5.9.

5.2 Requirement

The methodology of the pointing calibration using the Moon has not been well established yet. For instance, we have not had sufficient knowledge about systematic uncertainties related to the Moon. In this study, we demonstrate the pointing calibration using the Moon and provides the study of systematic error due to non-uniformity of a brightness temperature of the Moon. Because the Moon is brighter compared with the point-like planets, established methods in this study should be useful for other experiments whose beam width is sub-degrees as GroundBIRD.

The QUIET experiment had similar beam width ($27.3'$) [96]. They estimated an impact to the B-modes measurement owing to their achieved pointing accuracy ($27.3' \times 0.13$). The impact was the tensor-to-scalar ratio (r) of 0.001. They estimated an impact to the E-modes measurement as well. Its impact is two orders of magnitude lower than the E-modes signal calculated from ΛCDM. Based on this knowledge, we set the required accuracy of pointing calibration to $4.7'$ (i.e. $36' \times 0.13$).

5.3 Moon observation and reconstruction methods

GroundBIRD observes the wide sky regions by rotating the telescope in azimuth at a fixed elevation angle. On the other hand, the Moon is moving in both azimuthal and elevation directions with the rotation of the Earth as illustrated in Figure 5.2. We observe the Moon when it passes the scanning region at around the elevation of 70°.

We introduce a new coordinate system "Moon-centered coordinate system", whose axes comprises the elevation and azimuth from the Moon's center as shown in Figure 5.3. In the horizontal coordinate system, a pointing is not changed in the elevation direction, while the Moon is moving in time. On the other hand, the Moon is fixed in the Moon-centered coordinate system. Instead, the pointing is changed in the elevation. We can transform the pointing from the horizontal coordinate system to the Moon-centered coordinate system

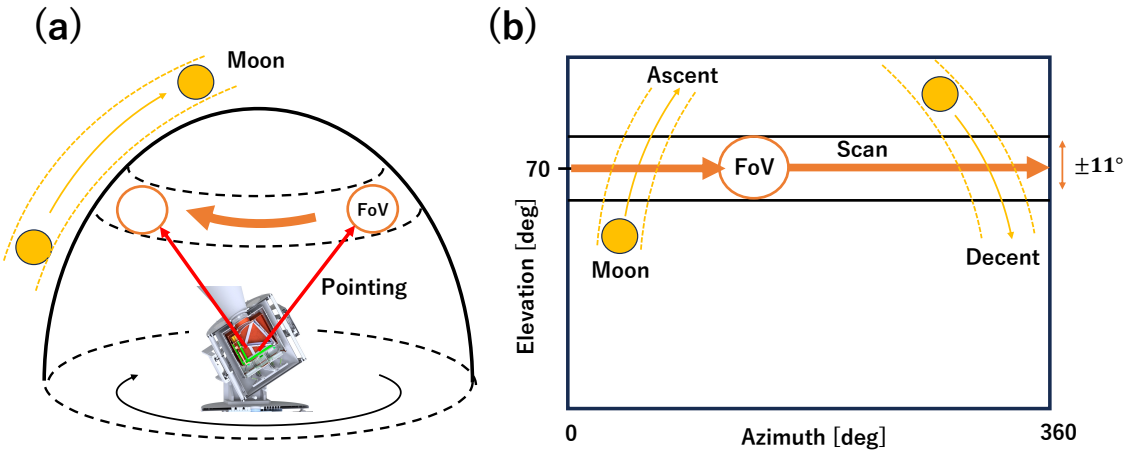

Figure 5.2: (a) Moon observation scheme for GroundBIRD. We observe the Moon when it passes the scanning region at the elevation of $\sim 70°$. (b) Projection of (a) into elevation-azimuth plane.

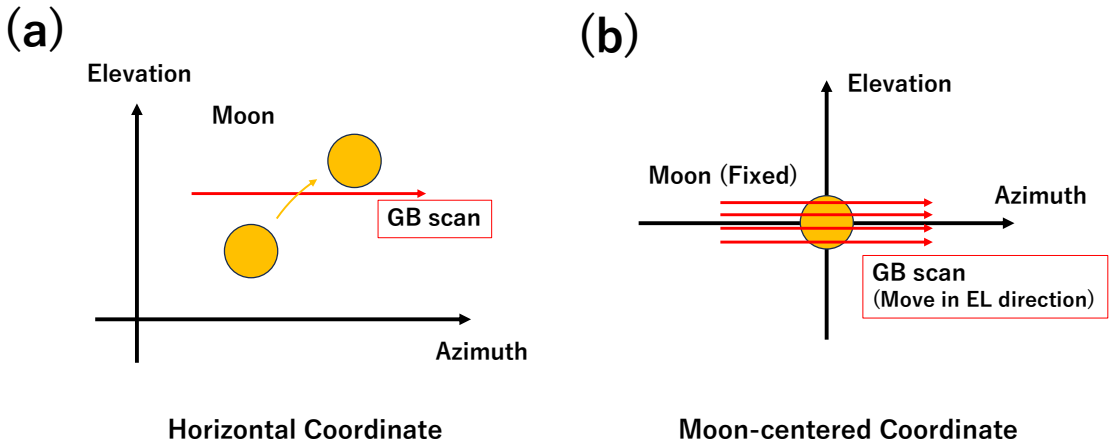

Figure 5.3: (a) Relationship between pointing of the telescope and the Moon in the horizontal coordinate system. In the horizontal coordinate system, the GroundBIRD scanning region is not changed in the elevation, while the Moon is moving in the elevation and azimuth. (b) Relationship between the pointing and the Moon in the Moon-centered coordinate system. This coordinate is useful to analyze the moon signal because its position is fixed and we can apply the angular response model directly.

by using true Moon position calculated with astropy. This coordinate system is useful to apply the angular response model of the Moon to the Moon observation data.

5.4 Angular response to the Moon

In the millimeter-wavelength range (e.g., 2 mm corresponds to 145 GHz), the signal from the Moon is dominated by thermal radiation from the Moon's surface rather than reflected sunlight. In the millimeter-wavelength range, we consider the Sun as a blackbody with a temperature of 10,000 K in the Rayleigh-Jeans limit of the blackbody spectrum. The intensity of the sunlight to the Moon depends on the distance from the Sun (d). If the

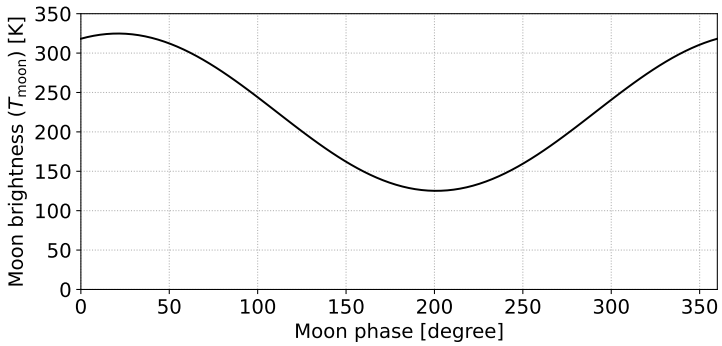

Figure 5.4: Brightness of the Moon signal as a function of the Moon phase for 145 GHz. The Moon phase at 0° corresponds to the full Moon [49].

surface temperature of the Sun is 10,000 K, the intensity is proportional to the square of a ratio of the radius of the Sun ($R_{\rm sun}$) to the distance (d) [97],

$$P_{\rm incident} \propto T_{\rm sun} \left(\frac{R_{\rm sun}}{d} \right)^2 . \tag{5.1}$$

This ratio is about 0.0046. Thus, the Moon receives only radiation which corresponds to the Rayleigh-Jeans temperature of 200 mK or so from the Sun. This is much lower than the surface temperature of the Moon ($\sim$ 200 K).

The brightness of the Moon signal in Kelvin ($T_{\rm moon}$) is modelled using the Moon phase (ψ), as follows [98]:

$$T_{\rm moon} = 225 \left\{ 1 + \frac{0.77}{\sqrt{1 + 2\delta + 2\delta^2}} \cos \left(\psi - \arctan \frac{\delta}{1+\delta} \right) \right\}, \tag{5.2}$$
$$\delta \equiv 0.3\lambda,$$

where λ is the wavelength in millimeters.

Figure 5.4 shows the brightness temperature of the Moon's surface at 145 GHz ($\lambda \sim$ 2 mm) as a function of the Moon phase. The maximum brightness temperature is delayed from the timing of the full Moon (i.e., the Moon phase of 0°) owing to a delay in the temperature variation at the Moon's surface. The maximum and minimum brightness temperatures of the Moon are 325 K and 125 K, respectively.

In the case of observation from the Earth, the visible brightness temperature ($T_{\rm eff}$) at the edge of the Moon is different from the $T_{\rm moon}$ because refractive indices of the Moon's surface is different from that in a vacuum. Considering the Moon as a black body sphere covered by a dielectric material layer [97], we can calculate the angular distribution of the visible brightness, as shown in Figure 5.5 (a). This is almost a top-hat distribution with a diameter of 30′. The mean temperature within the visible size of the Moon corresponds to the brightness temperature ($T_{\rm moon}$). Outside of the visible size of the Moon, $T_{\rm eff}$ corresponds to the CMB temperature (2.725 K). In addition, we have to take the beam into account for real observations. As shown in Figure 5.5 (b), we used an angular response model convolved with the visible brightness ($T_{\rm eff}$) and a Gaussian beam. In real, there is nonuniformity of the Moon's surface due to the Moon phase. This effect to the pointing calibration is discussed in section 5.9.

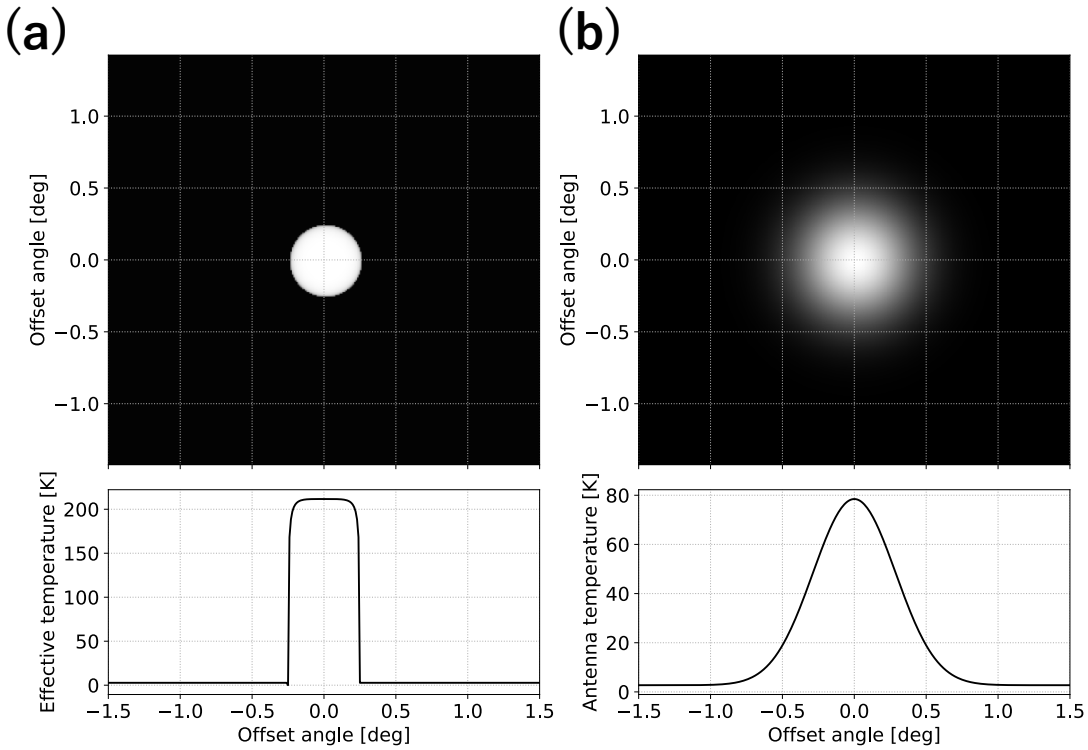

Figure 5.5: (a) Distribution of visible brightness temperature around the Moon from the Earth. A visible size of the Moon is assumed 30′ in this plot. (b) Convolved distribution with the beam modeled using the simple Gaussian (beam width of 36′) which is the designed value of GroundBIRD. The plots in the bottom row present a cross-sectional view [49].

The visible size of the Moon is calculated by using the radius of the Moon and the distance between the Moon and the telescope. The Moon radius is 1737.4 km and the distance is calculated by using astropy. We use this information for calculating the angular response model. There could be no significant improvement for extracting the Moon's center by using the calculated visible size. This is because it changes the angular response model symmetrically from the center of the Moon. As shown in Figure 5.6, the visible sizes before the convolution were changed owing to the rotation of the Earth as well as a revolution of the Moon. FWHMs of the angular resolution model were also changed.

5.5 Moon observation data

We performed 19 observations of the Moon using an azimuth rotation scan at 10 RPM with a fixed elevation at 70° as listed in Table 5.1.

We used time-ordered data (TOD) for each detector as well as telescope encoder data for Moon observation. The duration of each TOD data was 38–60 minutes. As described in section 3.3.1, one of the 23 detectors could not be used because its resonant frequency was outside the readout bandwidth of 200 MHz. Prior to the analysis, we performed the correction of the microwave phase delay owing to the cable length and the correction of the detector response as described in section 3.4. In addition, we selected good-quality

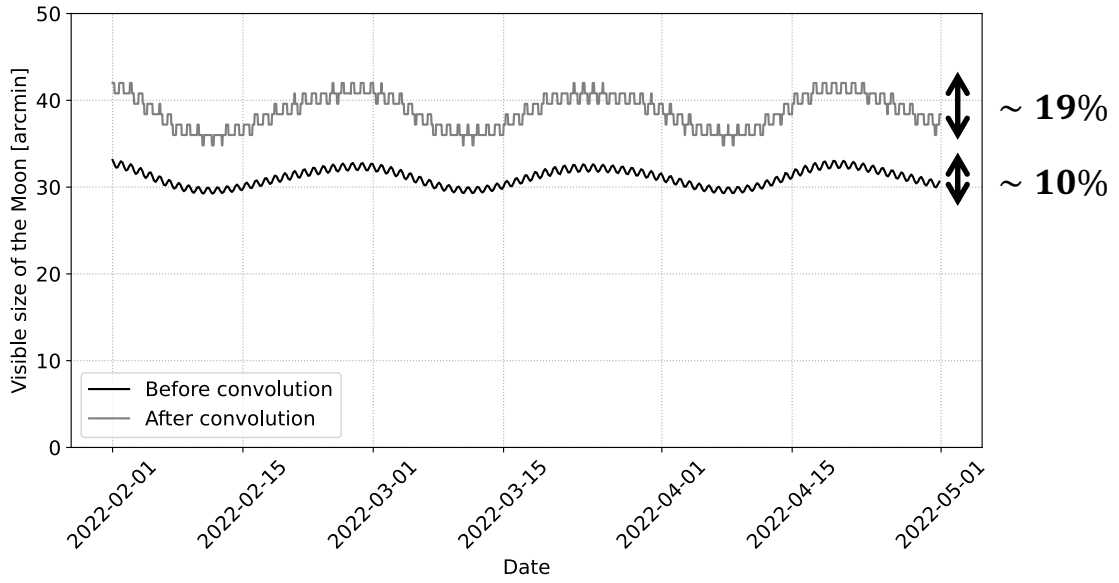

Figure 5.6: The visible size of the Moon before and after convolution with the beam from February to April 2022. It is changed owing to the Earth rotation and revolution of the Moon. The visible sizes of the Moon before the convolution fluctuated by 10%. After the convolution, FWHMs of the angular response model fluctuated by 19%.

Table 5.1: Information on the Moon observations during the commissioning observations.

Observation date(UTC)	Duration [min]	Ascent or decent	Azimuth [deg]	Elevation [deg]
8/2/2022 17:11 - 18:11	60	ascent	106 - 126	61 - 73
8/2/2022 20:14 - 21:01	47	decent	238 - 253	63 - 72
14/2/2022 22:12 - 22:50	38	ascent	95 - 103	64 - 72
15/2/2022 22:56 - 23:56	60	ascent	101 - 120	62 - 74
16/2/2022 23:48 - 24:48	60	ascent	110 - 133	61 - 72
17/2/2022 02:36 - 03:36	60	decent	224 - 247	61 - 72
7/3/2022 15:29 - 16:29	60	ascent	115 - 146	65 - 75
7/3/2022 18:01 - 19:01	60	decent	230 - 252	61 - 72
8/3/2022 15:47 - 16:47	60	ascent	100 - 117	62 - 74
9/3/2022 16:30 - 17:30	60	ascent	93 - 104	62 - 75
9/3/2022 19:50 - 20:43	52	decent	258 - 268	62 - 73
10/3/2022 20:42 - 21:36	54	decent	266 - 273	61 - 73
5/4/2022 17:41 - 18:28	47	decent	255 - 265	63 - 73
6/4/2022 15:26 - 16:26	60	ascent	91 - 103	65 - 78
6/4/2022 18:34 - 19:26	53	decent	264 - 272	62 - 73
7/4/2022 19:25 - 20:23	58	decent	269 - 275	61 - 73
8/4/2022 16:50 - 17:50	60	ascent	86 - 92	62 - 75
8/4/2022 20:16 - 21:16	60	decent	269 - 275	60 - 73
12/4/2022 20:28 - 21:28	60	ascent	114 - 140	62 - 73

data from each detector for each observation based on the following criteria:

- The intervals of the resonant frequencies for each detector must be greater than 0.5 MHz for the same observation. This condition eliminates potential crosstalk among

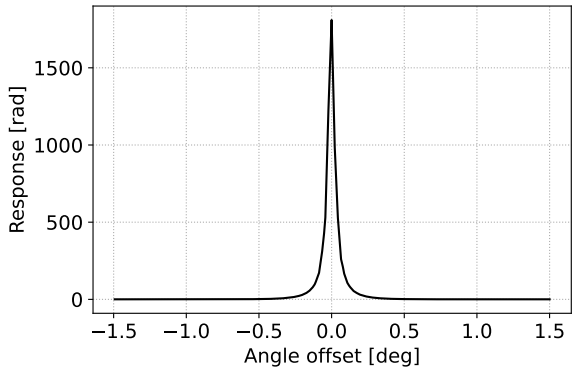

Figure 5.7: Example of the rapid jump in the detector response. If the signal intensity is higher than the range where we can model the resonance correctly, variations of detector response are rapidly changed due to the correction of the nonlinear effect by using $\tan\left(\frac{\theta_{\rm res}}{2}\right)$. $\theta_{\rm res}$ is the phase response after the correction of microwave phase delay as described in 3.4.

the detectors. We did not use two of the 22 detectors due to this criterion.

- Data within an elevation of 1.5° from the Moon center must be obtained continuously for each detector, i.e., each detector must observe the outside region of the Moon as well as the Moon itself.

- The Moon signal must be within the range where the resonance can be correctly modeled for each detector. As described in section 3.4, the detector response (θ) is proportional to $\tan\left(\frac{\theta_{\rm res}}{2}\right)$ where $\theta_{\rm res}$ is the phase response after the correction of the microwave phase delay. Thus, we observe a rapid jump in the detector response when the signal intensity is higher than the range. We identified it as rapid variations of detector response (more than 30 times) within the visible size of the Moon in the azimuthal scan. Figure 5.7 shows an example of it. We did not use one of the 20 detectors based on this criterion.

Finally, 345 Moon observation samples were selected based on these criteria.

5.6 Reconstruction of the position of the Moon

One of the TODs for single Moon observation data is shown in Figure 5.8 (a). The overall shape of the bottom figure traces the elevation pattern of the Moon. On the other hand, the spikes in the top figure trace the azimuth pattern of the Moon. After the synchronization between TODs and encoder data with the common pulse as described in section 2.4.4, maps in the horizontal coordinate system for each detector were constructed. For each TOD point, the true Moon position in the horizontal coordinate system can be calculated by using astropy. By using the true Moon positions, we converted the maps in the horizontal coordinate system to the Moon-centered coordinate system. After making the Moon image, we subtracted the baseline offset for each azimuthal scan to eliminate the effects of atmospheric fluctuations as well as atmospheric radiation itself. Each baseline offset was calculated by taking the mean of the detector response between 1.5° and 2.0°

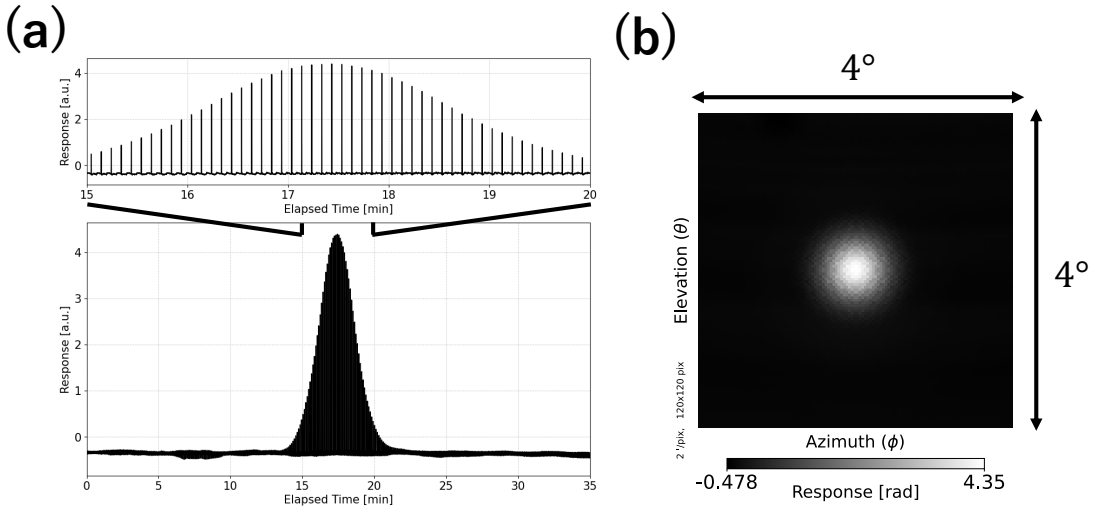

Figure 5.8: (a) Detector response as a function of the elapsed time. The plot above is an enlarged plot of the plot below concerning the time. Each spike in the plot above is the Moon signal. (b) Reconstructed Moon image using the Moon-centered coordinates for azimuth (horizontal axis) and elevation (vertical axis). This image is created using healpy with the parameter $N_{side} = 1024$. The baseline fluctuations due to atmospheric radiation are subtracted as described in the text [49].

from the observed center of the Moon. One of the reconstructed Moon images in the Moon-centered coordinate system is shown in Figure 5.8 (b). Figure 5.9 presents the reconstructed Moon images from each detector for one of the observations. The positions of the observed Moon image for each detector are different because each detector sees a different sky due to the collimation offset as described in section 2.2.

Considering a constant offset (B) and a gain of the detectors (G), we constructed a response model of the detector by using the following formula,

$$Res(\theta, \phi) = G \times T_{\rm A}(\theta, \phi, \theta_c, \phi_c, \omega) + B, \tag{5.3}$$

where T_A is the angular response model of the Moon after convolving the beam. Based on this response model, we extracted the Moon's center (θ_c, ϕ_c) for each observation by performing unbinned likelihood fit for the data within a radius of 1.5°. The fitting parameters were the elevation and the azimuth of the Moon center, detector gain, beam width, and constant offset as the background residual.

Figure 5.10 presents one of the results obtained by the fitting procedure. The difference in the beam between the data and the model has a negligible effect on the pointing calibration, which is discussed in section 5.9. The extracted Moon positions for each detector and each observation comprised 345 samples and were used to calibrate the pointing model described in the next section. The average collimation interval (i.e., a distance between neighbor detectors at the sky) was $52' \pm 1'$, which is consistent with the design ($51'$).

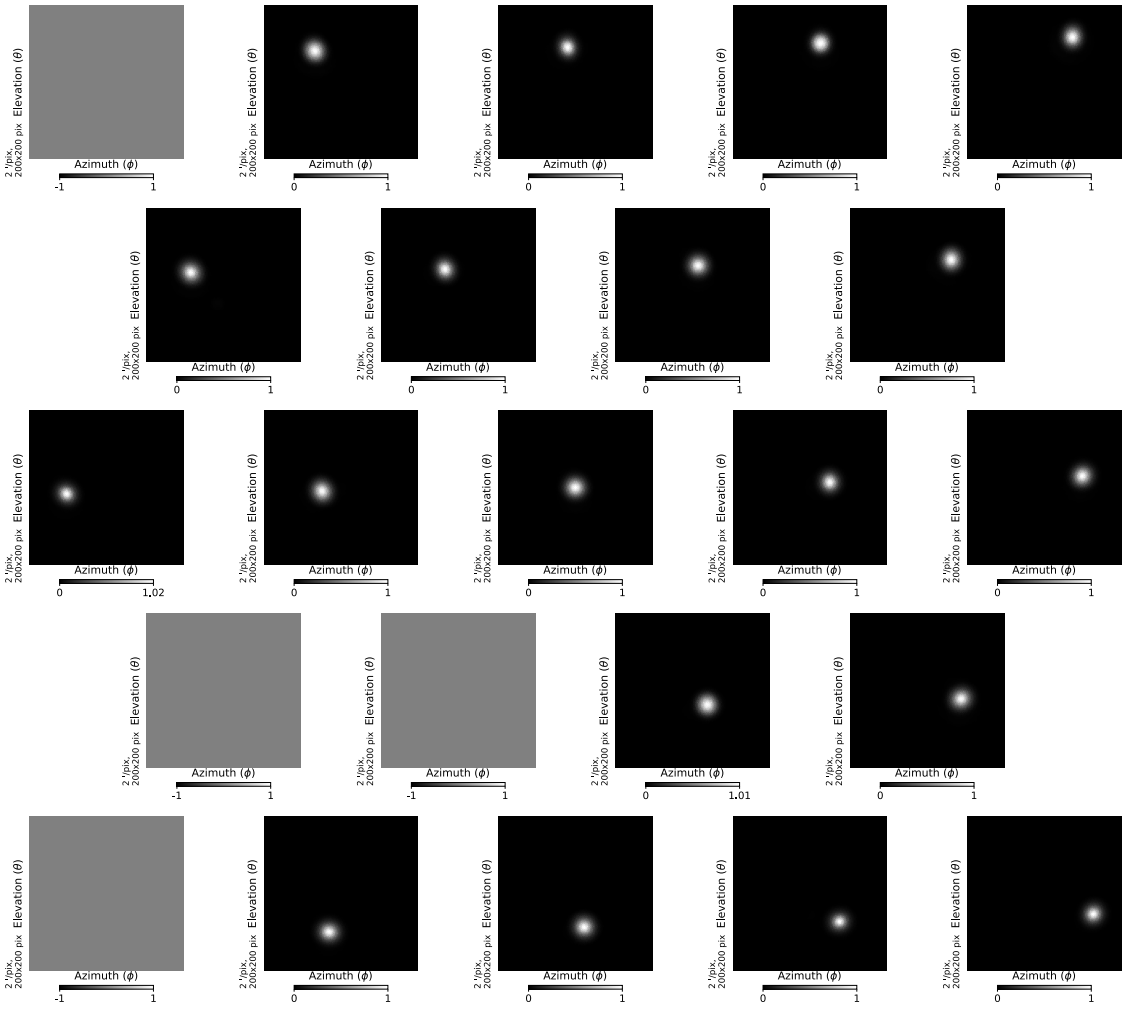

Figure 5.9: Reconstructed Moon images for each detector in the Moon-centered coordinates. The highest signal is normalized to 1. The positions of the plots indicate the locations of each detector pixel on the focal plane. The data of the four detectors are not used; they are indicated by the gray squares. The locations of the Moon images in each detector image are different because each detector has a different collimation offset. The angular ranges in all plots are $400'$ (i.e.,6.7°) times $400'$ (i.e.,6.7°). These images are created using healpy with the parameter $N_{\mathrm{side}} = 1024$ [49]

5.7 Pointing model

The tilts of the elevation and azimuth axes cause pointing shits in terms of the elevation (θ) and azimuth (ϕ) in the horizontal coordinate system as shown in Figure 5.11 (a). Thus, we modeled their pointing shifts by using the following formula [99]:

$$\begin{cases} \delta_\theta(\phi) = \delta_{\mathrm{NS}} \cos\phi + \delta_{\mathrm{EW}} \sin\phi, & \text{(5.4a)} \\ \cos\theta\delta_\phi(\theta,\phi) = \delta_{\mathrm{NS}} \sin\theta \sin\phi - \delta_{\mathrm{EW}} \sin\theta \cos\phi, & \text{(5.4b)} \end{cases}$$

where δ_{NS} is the tilt in the north–south direction and δ_{EW} is the tilt in the east–west direction as illustrated in Figure 5.11 (b) and (c). Figure 5.12 shows pointing shifts as a function of the true elevation and the true azimuth for $\delta_{\mathrm{NS}} = -1.8'$ and $\delta_{\mathrm{EW}} = -2.8'$

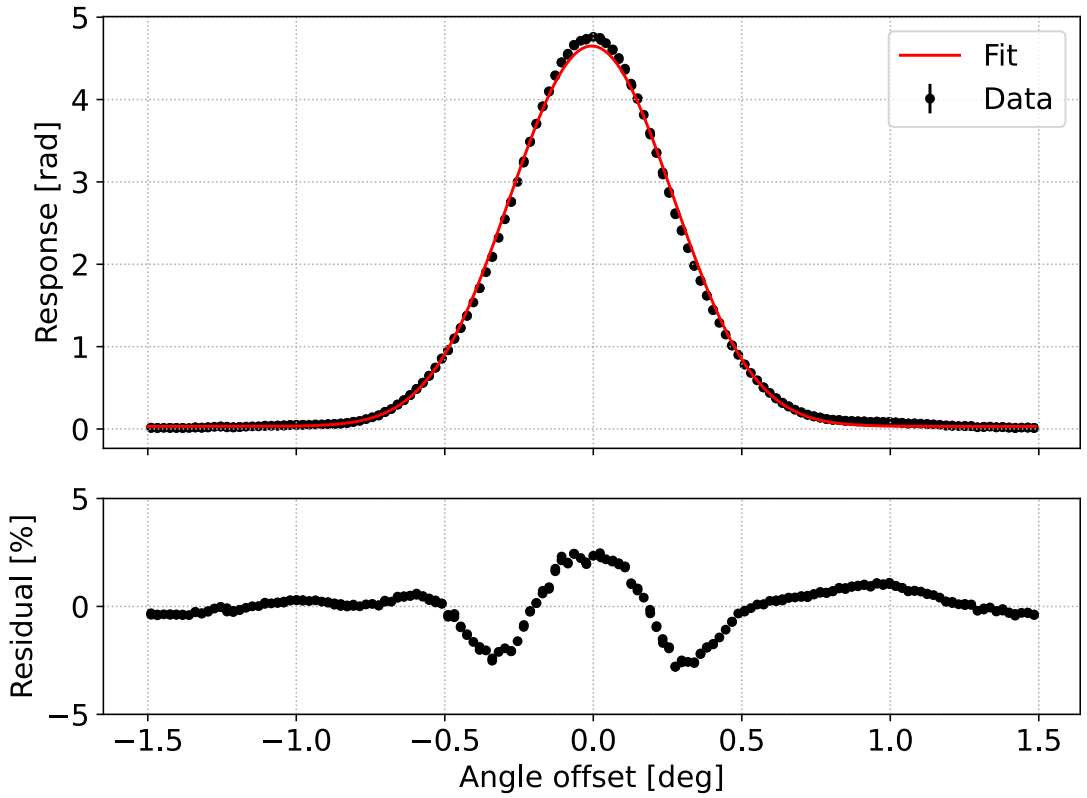

Figure 5.10: Cross-sectional views of the Moon data and a fit. The non-Gaussianity of the beam shape leads to approximately 3% residuals because we use the simple Gaussian model in the fit. This effect may affect the accuracy of pointing calibration and is considered to be a systematic error, described in the section 5.9 [49].

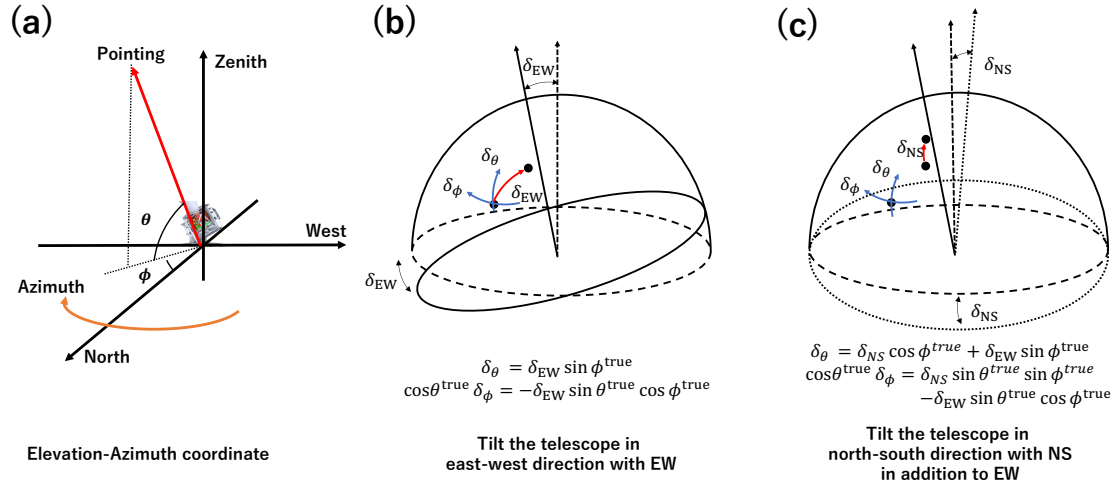

Figure 5.11: Schematics of elevation–azimuth coordinates (a) and the axis offsets in the east–west direction (b) [49]. Pointing in the elevation and the azimuth shift if a telescope base is tilted.

calculated from Eq. (5.4a) and Eq. (5.4b).

In addition to the tilts of the axes, the encoder and collimation intervals of each

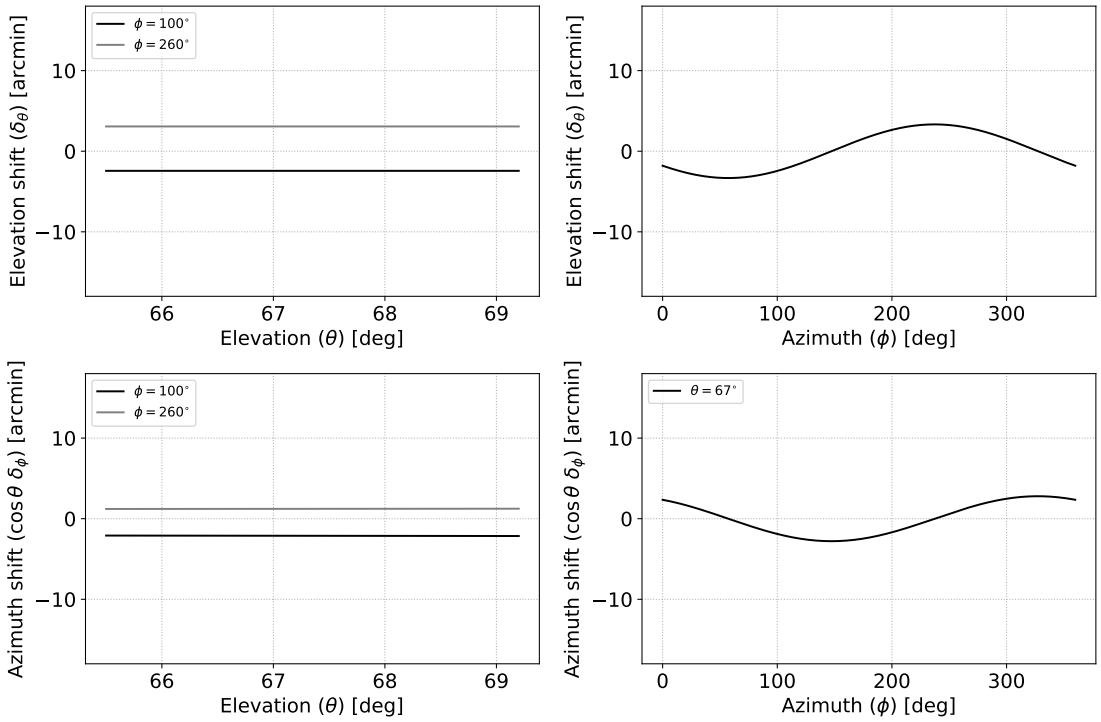

Figure 5.12: Pointing shifts as a function of the elevation or azimuth with δ_{NS} of $-1.8'$ and δ_{EW} of $-2.8'$. The shift in the elevation depends on the azimuth pointing. In contrast, the shift in the azimuth depends on both the elevation and the azimuth pointing [49].

detector cause constant pointing shits as shown in Figure 5.9. We define the parameters for the encoder offsets in terms of elevation (θ_e) and azimuth (ϕ_e). We also define the collimation offsets of each detector for the elevation (θ_i) and azimuth (ϕ_i). Here, i is the index for each detector. Using these parameters, the pointing model for the data is defined as follows:

$$\begin{cases} \theta^{\mathrm{model}} = \theta^{\mathrm{data}} - \theta_e - \theta_i - \delta_\theta(\phi^{\mathrm{true}}), & \text{(5.5a)} \\ \phi^{\mathrm{model}} = \phi^{\mathrm{data}} - \phi_e - \phi_i - \delta_\phi(\theta^{\mathrm{true}}, \phi^{\mathrm{true}}), & \text{(5.5b)} \end{cases}$$

where θ^{data} and ϕ^{data} are the extracted Moon's center from the reconstructed Moon image for each detector for each observation, and θ^{true} and ϕ^{true} are the true positions of the Moon, which are calculated by using astropy.

These parameters were optimized to minimize the angular distance (dl) between the true and model positions, where $dl^2 = (\theta^{\mathrm{model}} - \theta^{\mathrm{true}})^2 + [\cos\theta^{\mathrm{true}}(\phi^{\mathrm{model}} - \phi^{\mathrm{true}})]^2$. Although dl can be used under the approximation of the small angular distance, this approximation makes a negligible effect in this study ($\leq 0.01''$).

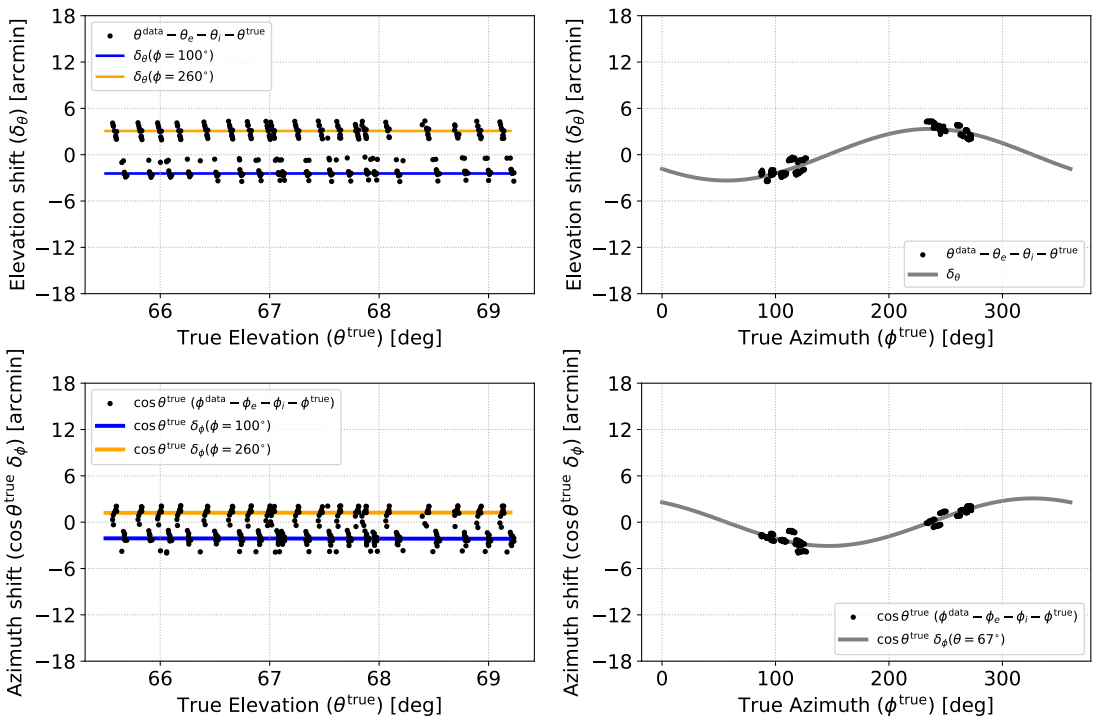

Figure 5.13: Pointing shifts as a function of the elevation or azimuth of the true Moon position. The points comprise reconstructed data calculated using Eq. (4a) and Eq. (4b). The lines were calculated using Eq. (2a) and Eq. (2b) with the same values for δ_{NS} and δ_{EW} [49]. One moon observation corresponds to a horizontal in the left two figures and a cluster in the right two figures.

5.8 Results of the pointing calibration

The optimized tilt angles were $\delta_{\rm NS} = -1.8'$ and $\delta_{\rm EW} = -2.8'$. We calculated the pointing shifts by using the extracted encoder and collimation offsets as follows:

$$\begin{cases} \delta_\theta(\phi^{\rm true}) = (\theta^{\rm data} - \theta_e - \theta_i) - \theta^{\rm true}, & \text{(5.6a)} \\ \cos\theta^{\rm true}\delta_\phi(\theta^{\rm true}, \phi^{\rm true}) = \cos\theta^{\rm true}[(\phi^{\rm data} - \phi_e - \phi_i) - \phi^{\rm true}]. & \text{(5.6b)} \end{cases}$$

Figure 5.13 shows the pointing shifts as a function of the true position of the Moon at that elevation or azimuth. We also overlay the lines calculated by using Eq. (5.4a) and Eq. (5.4b) for comparison. These pointing shifts were within the our requirement ($4.7'$).

In the CMB analysis, we have to calculate the pointing based on the optimized model. Although $\theta^{\rm true}$ and $\phi^{\rm true}$ are unknown in Eq. (5.5a) and Eq. (5.5b), we can calculate accurate pointing iteratively with sufficient precision [81] instead of solving Eq. (5.5a) and Eq. (5.5b) exactly. We use the following formulae:

$$\begin{cases} \theta_i^{(0)} = \theta^{\rm data} - \theta_e - \theta_i, & \text{(5.7a)} \\ \phi_i^{(0)} = \phi^{\rm data} - \phi_e - \phi_i, & \text{(5.7b)} \end{cases}$$

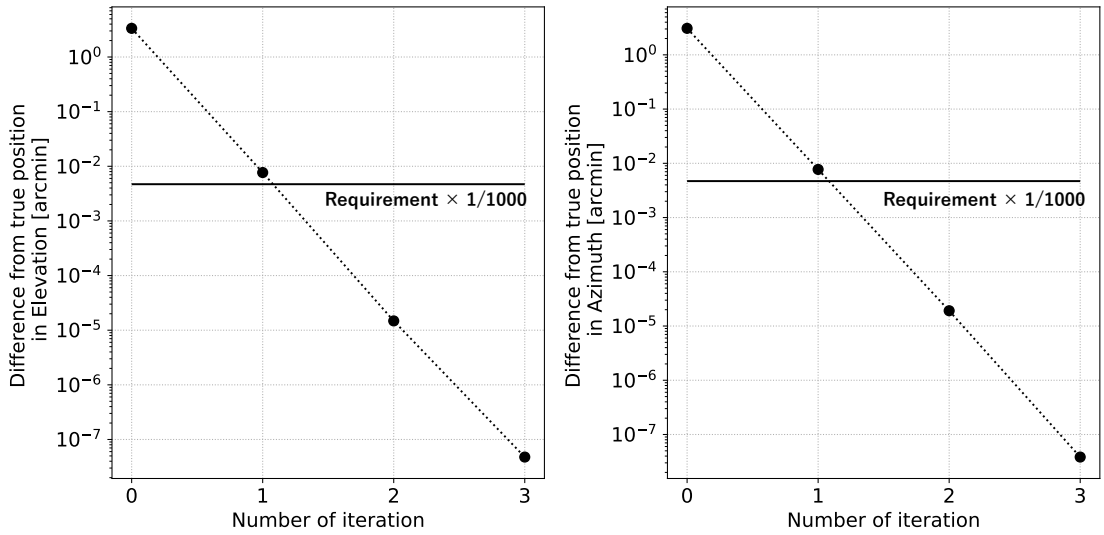

Figure 5.14: Pointing differences between a calibrated position with Eq. (5a) – Eq. (6b) from the true position as a function of the number of iterations for the elevation and azimuth. The elevation angle is assumed to be 67°, which is a typical elevation angle. The solid lines are 1/1000 of the requirement. We realize a sufficient precision at $n \geqq 2$ [49].

$$\begin{cases} \theta_i^{(n)} = \theta^{\mathrm{data}} - \theta_e - \theta_i - \delta_\theta \left(\phi_i^{(n-1)}\right), & \text{(5.8a)} \\ \phi_i^{(n)} = \phi^{\mathrm{data}} - \phi_e - \phi_i - \delta_\phi \left(\theta_i^{(n-1)}, \phi_i^{(n-1)}\right), & \text{(5.8b)} \\ \quad n = 1, 2, 3, ..., \end{cases}$$

where n indicates the n-th iteration. For validation of this calculation, we numerically calculated the differences from the true position for each n by using Eq. (5.8a) and Eq. (5.8b) and the extracted parameters. The results are shown in Figure 5.14. We could achieve sufficient precision at $n \geqq 2$. We conclude that two iterations should be performed in the calculation of the pointing to reduce this effect on the pointing calibration to a negligible level.

Figure 5.15 shows the residuals of the Moon as reconstructed from the true positions for all 345 samples. All samples were calibrated within the range of our requirements. Their root mean squares were $0.6'$ for the elevation and $0.5'$ for the azimuth times $\cos\theta$. Similar plots for each detector are presented in Figure 5.16. Their mean values were consistent with zero; that is, there is no bias.

5.9 Systematics uncertainties

The uncertainty associated with the beam shape is estimated by changing the response model of the fit. We compared the results of the baseline analysis with additional three response models as follows:

- Fixed the beam with as design (i.e. $36'$).
- Elliptical Gaussian beam. We extracted ellipticity of 2.6 ± 1.0 %.

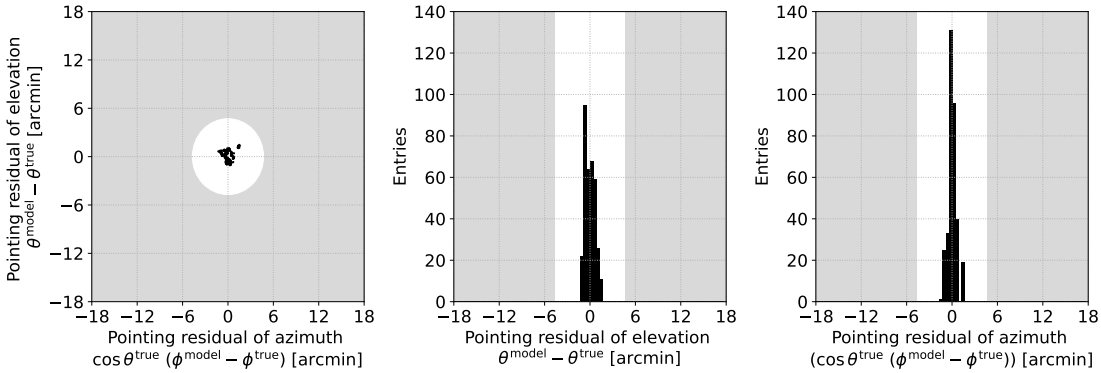

Figure 5.15: Residuals of the calibrated pointing from the true position for the elevation and the azimuth. The dynamic range of the elevation and azimuth axes corresponds to the beam width of the GroundBIRD (36′). They are within the requirement, which is indicated by the unshaded regions. [49]. RMSs of the elevation and azimuth are 0.6′ and 0.5′, respectively.

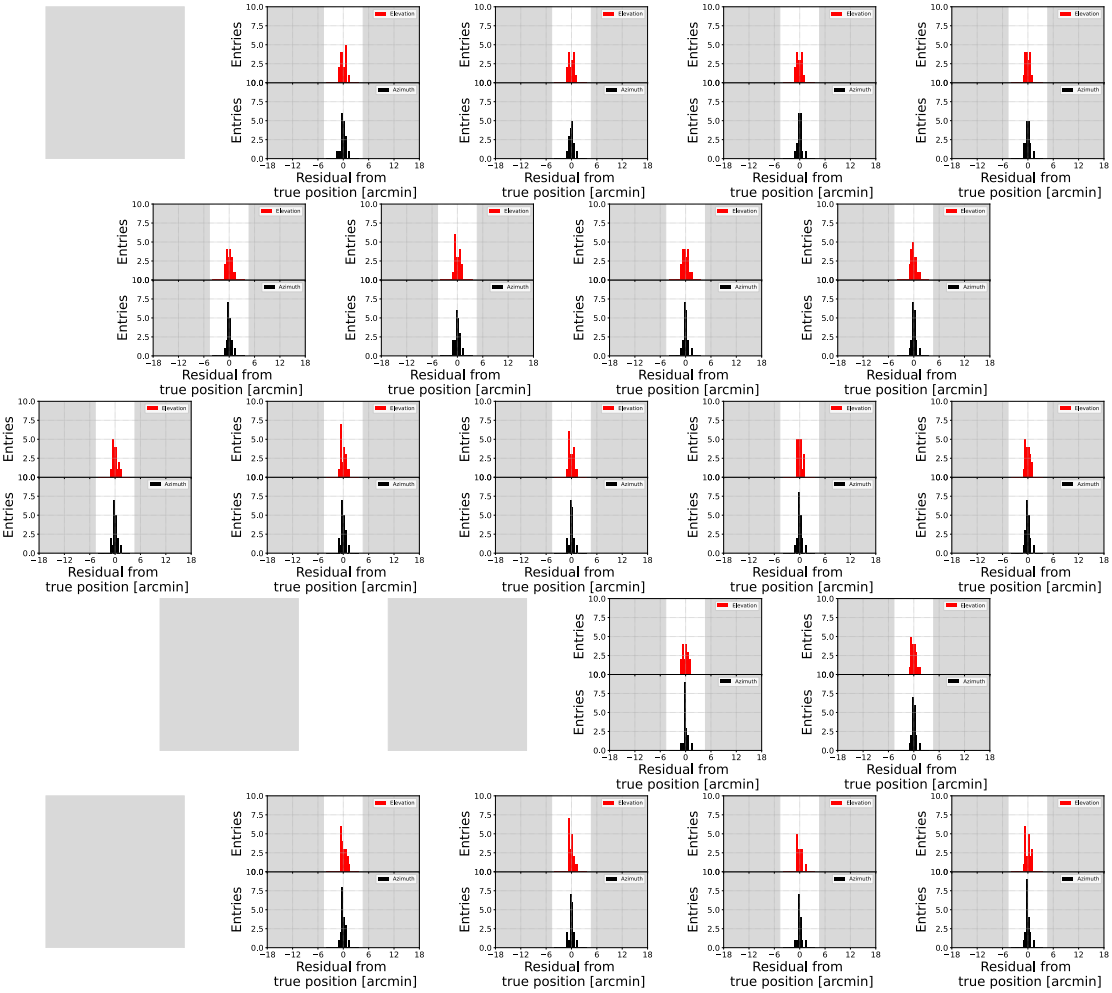

Figure 5.16: Pointing residuals of the elevation (black) and azimuth (red) for each detector. Their mean values for each detector are consistent with zero [49].

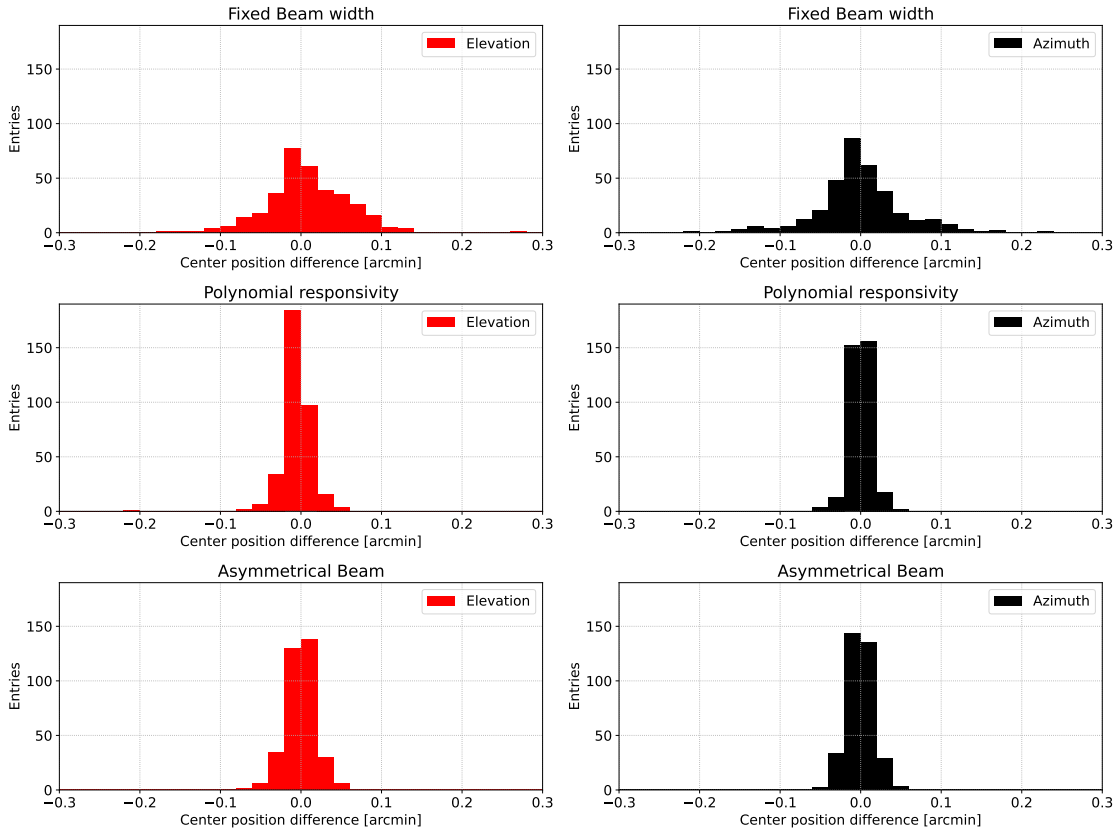

Figure 5.17: Difference of extracted Moon's center in the elevation and azimuth between the baseline model and three compared models: fixed beam width as the design, an asymmetrical two-dimensional Gaussian beam, and a polynomial responsivity. All differences are less than $0.26'$ and it is assigned as a systematic error of the Moon model.

- Polynomial (i.e., non-linear) responsivity

Figure 5.17 shows the histograms of each comparison for elevation or azimuth. The pointing differences among these three models are less than $0.26'$. Note that the assumed ellipticity of the systematic error study is larger than that of the simulation study ($< 1\%$). The uncertainties in the Moon's position owing to the time constant of the detector and the astronomical calculation with `astropy` are $0.14'$ and $0.31'$ [100], respectively. As described in chapter 2, the uncertainties in the elevation and azimuth encoders are $0.066'$ and $0.057'$, respectively. Ambient temperature change could affect the pointing. We evaluated this possible effect by comparing two calibration results at high temperature (average of 10 °C) and low temperature (average of 3 °C). We found the difference of $0.4'$, while the statistical fluctuation is dominant in this comparison. Therefore, we assigned $0.4'$ as systematic uncertainty due to ambient temperature. A possible mechanical variation associated with the scan is estimated from the difference between the residuals from the pointing model at azimuth $> 180°$ and that at azimuth $< 180°$. It was $0.0057'$

The systematic uncertainty is driven by the non-uniformity of the Moon's brightness temperature. We estimated this systematic uncertainty by using a simulation based on simplified temperature distributions of the Moon's surface for each Moon phase, as shown in Figure 5.18. Considering Eq. (5.2), we set the maximum (325 K) and minimum (125 K)

Table 5.2: Systematic uncertainties in pointing.

Source	[arcminute]
Beam shape	2.6×10^{-1}
Moon position	3.4×10^{-1}
Elevation encoder	6.6×10^{-2}
Azimuth encoder	5.7×10^{-2}
Ambient temperature	4.0×10^{-1}
Mechanical variation	5.7×10^{-2}
Non-uniformity temperature	3.2
Total	3.2

temperatures in the bright and shaded regions, respectively. This assumption gives us the most conservative systematic uncertainty. We extracted the central position of the Moon for the simulation data by using the same analysis method as that used for real data analysis. Figure 5.19 shows the difference between the extracted center position and input center position in the simulation. We assigned the maximum difference of ($3.2'$) as the systematic uncertainty due to the non-uniformity of the Moon's surface.

We summarized the systematic uncertainties in Table 5.2. We calculate the square root of the quadrature sum of all uncertainties. In total, we assigned a systematic uncertainty of $3.2'$ to the pointing calibration using the Moon.

5.10 Summary for pointing calibration

We calibrated the pointing of the GroundBIRD telescope by using the Moon observation data. The residuals of calibrated pointing from the true position were less than $1.6'$ Its root mean squares were $0.6'$ and $0.5'$ for the elevation and the azimuth, respectively. The systematic uncertainties in pointing were $3.2'$, which are driven by the non-uniformity of the brightness of the Moon. In total, we successfully achieved an uncertainty of $3.3'$ which is lower than our requirement ($4.7'$). For the CMB telescope, this was the first attempt at using the pointing calibration with the Moon for a beam width of $36'$ against the visible size of the Moon ($30'$). Thus, we realized sufficient pointing calibration.

We can frequently observe the Moon at high elevations. The orbital period of the Moon (monthly) is much shorter than that of planets ($\sim$ 10 years). In addition, the observation of the Moon with the high signal-to-noise ratio allows us to perform the unbinned likelihood fit to extract the center position of the Moon. It introduces the advantage to reduce the noise related to the data accumulation. In addition, we avoid a degradation of the angular resolution of detector response due to the binning of the data accumulation for the astronomical point sources. We discussed the systematic uncertainties related to the Moon. The non-uniformity of the Moon's brightness was assumed as the most conservative case. Nevertheless, it was one order of magnitude lower than the beam width. In conclusion, the established method in this study is applicable to other CMB telescopes whose beam width is sub-degrees.

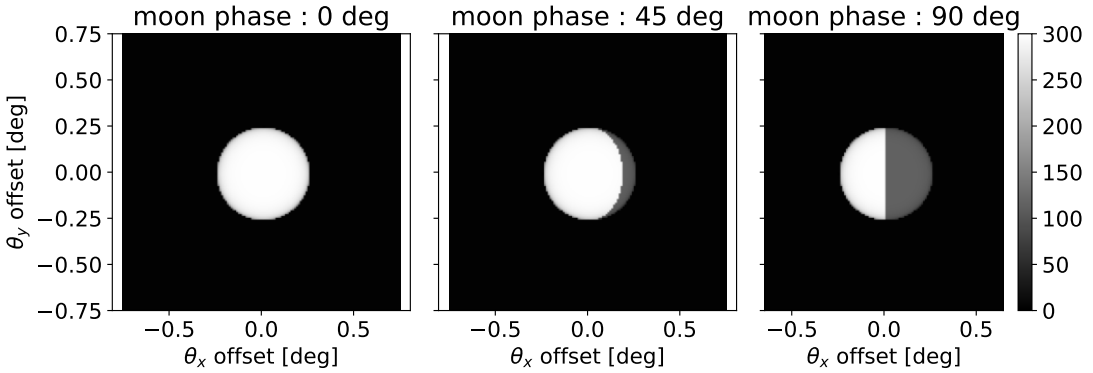

Figure 5.18: Distribution of the Moon brightness temperature, which varies with the Moon phase, where θ_x is the direction of the phase shift, and θ_y is perpendicular to it. The white and gray regions correspond to the brightness temperatures of 325 K and 125 K, respectively [49].

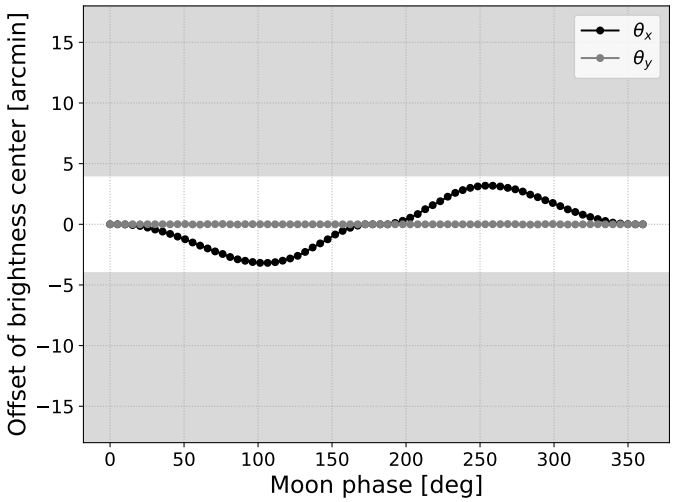

Figure 5.19: Offset of the brightness center from as a function of the Moon phase, where θ_x and θ_y are the directions of the offsets, as shown in Figure 5.18. The maximum offset found here is smaller than the requirement, which is indicated by the unshaded area [49].

Chapter 6

Calibration of Polarization Angle by using Pointing Information

Each antenna is polarization sensitive. Each antenna's response to the polarized signal varies with respect to the angle between antenna orientation and the polarized direction of the signal. "Polarization angle" is defined as each antenna orientation at the sky coordinate system. We need to calibrate the polarization angle for the CMB polarization analysis. This calibration is important to suppress potential crosstalk for the E-modes to the B-modes. In this chapter, we propose a new calibration method based on the pointing information.

6.1 Achievements in previous experiments

In previous CMB experiments, various calibration methods for the polarization angle have been attempted. Their methods and achieved precisions ($\delta\Psi$) are summarized in Table 6.1.

Polarized astronomical objects

There are polarized astronomical objects in the universe. The Crab Nebula (Tau A) is the most intense polarized astronomical object in the millimeter-wavelength range. Its polarized direction has been measured at frequencies below 150 GHz [106]. Its polarization fraction is approximately 7%. Based on the catalog from the previous measurements, we

Table 6.1: Methods and achieved precision (Ψ) for each polarization angle calibraion.

Method	$\delta\Psi$	Experiments
Minimizing the C_ℓ^{TB} and C_ℓ^{EB}	1.6° [102]	BICEP
Dielectric sheet	0.7° [103]	BICEP
Minimizing the C_ℓ^{EB}	0.2° [104]	POLARBEAR
Tau A	0.43° [104]	POLARBEAR
The Moon	1.7° [96]	QUIET
Blackbody source and Metal wire	1° [105]	SPTpol

can calibrate the polarization angle at below 150 GHz. The catalog precision is 0.3° [106]. The origin of the Tau A signal is synchrotron radiation. Its intensity is inversely proportional to the third power of the frequency ($I \propto \nu^{-3}$). The calibration using Tau A tends to be difficult at high frequency.

The Moon is another calibration source. It emits radial polarization signals because of the different refractive indices of the Moon surface. The QUIET experiment achieved precision of 1.7° by using the Moon [96].

Artificial calibrator

The BICEP experiment used a polarization dielectric sheet which can generate a polarized signal to the telescope [103]. They achieved a precision of the polarization angle of 0.7° [103].

Using a metal wire is another artificial calibration [107]. This method has not given the uncertainty of the absolute polarization angle yet[1]. The SPTPol experiment used a combination of a thermal blackbody source and a metal wire [105]. They achieved a precision of 1° at 150 GHz band.

Minimizing Correlation between B-modes and E-modes or temperature anisotropy

We can also use CMB itself for calibrating the polarization angle under the assumption of no exotic phenomenon. The correlation between E-modes and B-modes should be zero in case there is no-parity violation in the CMB patterns. In this case, the correlation between the B-modes and temperature anisotropy should be zero, too. Non-zero power for C_ℓ^{EB} and C_ℓ^{TB} indicates the mis-calibration of the polarization angle. This principle allows us to calibrate the polarization angle by nulling C_ℓ^{EB} or/and C_ℓ^{TB}. This method achieved 0.2° precision [104]. Losing the sensitivity for the exotic science, such as the parity violation in the CMB patterns is a considerable downside. For instance, the cosmic birefringence is one of parity-violating physics. The birefringence angle (β) was currently found to be $\beta = 0.36° \pm 0.11°$ whose significance exceeded 3σ [109]. We cannot use this calibration method when we study this topic.

6.2 Requirement

For the optical depth (τ) study, the precision of 1° is enough. As shown in Figure 6.1, the mis-calibration of the polarization angle ($\delta\Psi$) reduces E-modes by only a factor of $\cos^2(2\delta\Psi)$. On the other hand, for B-modes measurement (i.e., searching the primordial gravitational waves), we need to achieve a high precision because the mis-calibration causes leakage from E-modes to B-modes by a factor of $\sin^2(2\delta\Psi)$. A target accuracy for the polarization angle becomes to be 0.43° if we control the E-modes to B-modes leakage at below the level of $r = 0.004$ (1/10 of the current upper limit for r).

[1] The Simons Observatory plans to achieve a precision of 0.1° by using a gravity reference [108].

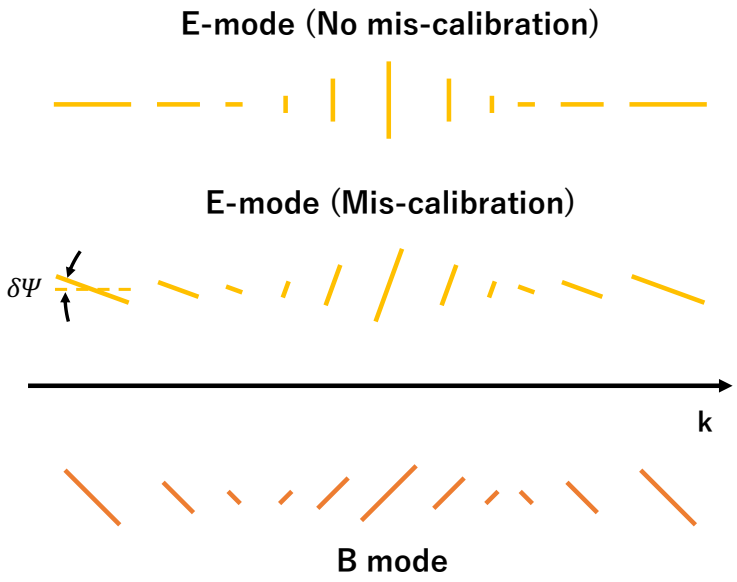

Figure 6.1: Illustration for leakage from E-modes to B-modes due to the mis-calibration of the polarization angle ($\delta\Psi$). Mis-calibrated E-modes include the B-modes component.

6.3 Methodology of polarization angle calibration by using pointing information

6.3.1 Definition of the polarization angle

As shown in Figure 6.2, the polarization angle is defined on the tangent plane in each coordinate system. The axes of the tangent plane in the horizontal coordinate system are defined as follows,

$$\begin{cases} e_\theta = (\cos\theta\cos\phi,\ \cos\theta\sin\phi,\ -\sin\theta) & \text{(6.1a)} \\ e_\phi = (-\sin\phi,\ \cos\phi,\ 0), & \text{(6.1b)} \end{cases}$$

where θ is a angle from the zenith (i.e., $\theta \equiv 90^\circ - E$) and ϕ is a counter-clockwise angle from the north (i.e., $\phi \equiv -A$).

The axes of the tangent plane in the equatorial coordinate system are defined by using the right ascension (α) and the declination (δ),

$$\begin{cases} e_\delta = (\cos\delta\cos\alpha,\ \cos\delta\sin\alpha,\ \sin\delta) & \text{(6.2a)} \\ e_\alpha = (-\sin\alpha,\ \cos\alpha,\ 0), & \text{(6.2b)} \end{cases}$$

6.3.2 Polarization angle in real observations

In real observations, the polarization angle is not perfectly aligned to the design. It varies with the pointing because of spherical projection. The tilt of telescope axes also varies the direction of the polarization angle. Figure 6.3 represents projections of the pointing and antenna orientations for squared wafer (antenna arrays) in an azimuth-elevation plane in four different situations. Here, we assume the antenna orientations are parallel to the horizontal direction of the wafer. Figure 6.3 (a) assumes the flat sky as well as the perfect alignment of the wafer to the boresight angle. Figure 6.3 (b) shows the case of

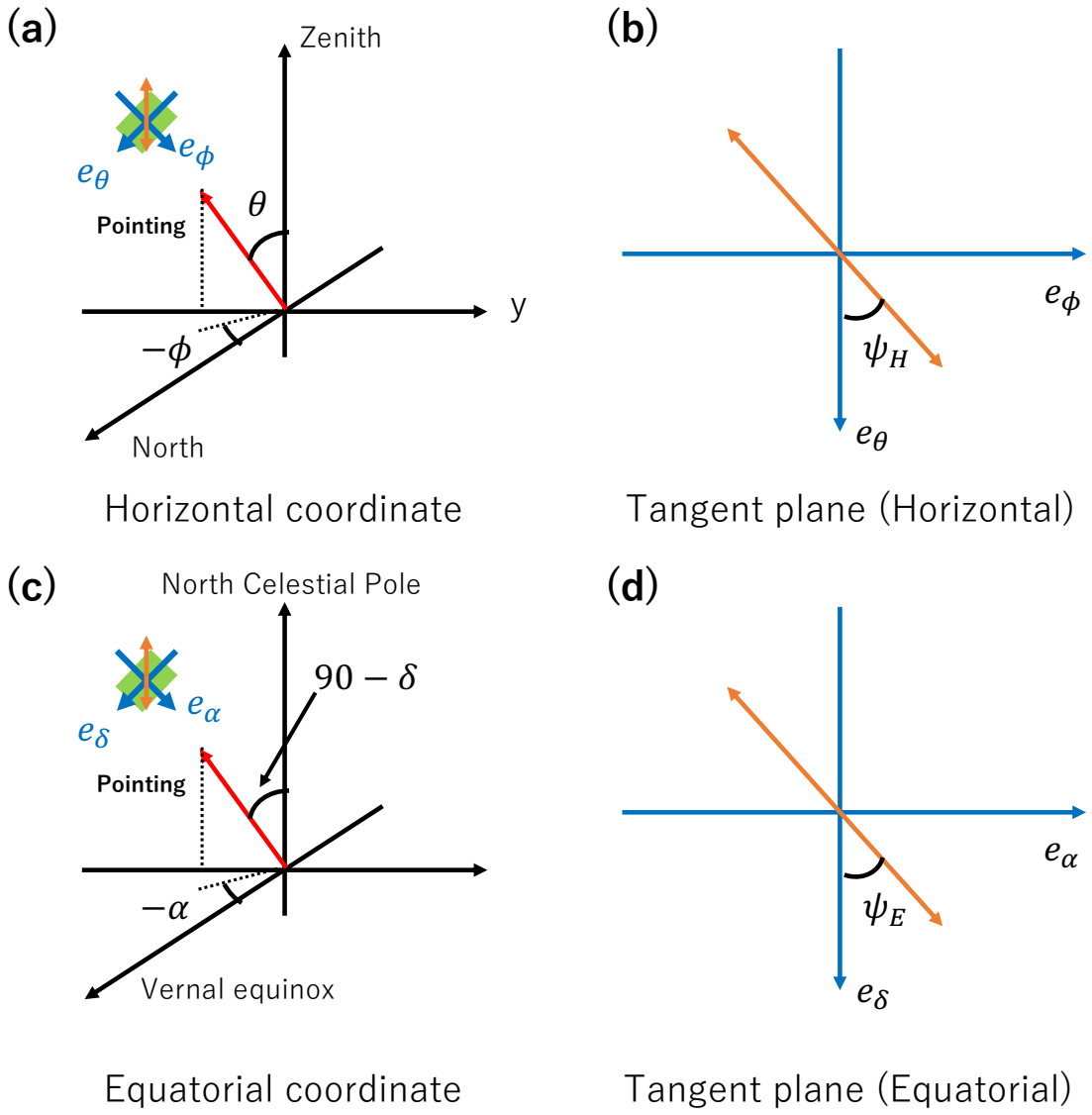

Figure 6.2: (a), (b) Definition of the polarization angle in the horizontal coordinate system. Axes of the tangent plane (e_θ and e_ϕ) in the horizontal coordinate system are defined as Eq. (6.1). (c), (d) Definition of the polarization angle in the equatorial coordinate system. Axes of the tangent plane (e_δ and e_α) in the equatorial system are defined as Eq. (6.2). Orange arrows are polarization orientation. The polarization angle is defined as an angle from e_ϕ and e_δ on each tangent plane at every pointing. We follow a HEALPix convention for the definition of the polarization angle.

the spherical sky (i.e., real coordinate) instead of the flat sky. In the spherical coordinate system, azimuth offset (δA) is approximately inversely proportional to the elevation (E), i.e., $\delta A \sim \delta A_{\rm flat}/\cos(E)$. The tangent plane for each azimuth is also changed. Thus, the antenna orientations are rotated. Figure 6.3 (c) shows the case that the wafer orientation is rotated from the gravity direction. In this case, the projections of the pointing and the antenna orientations rotate on the sky sphere. Figure 6.3 (d) shows the case there are telescope axes' tilts in addition to the case of Figure 6.3 (c). As we described in chapter

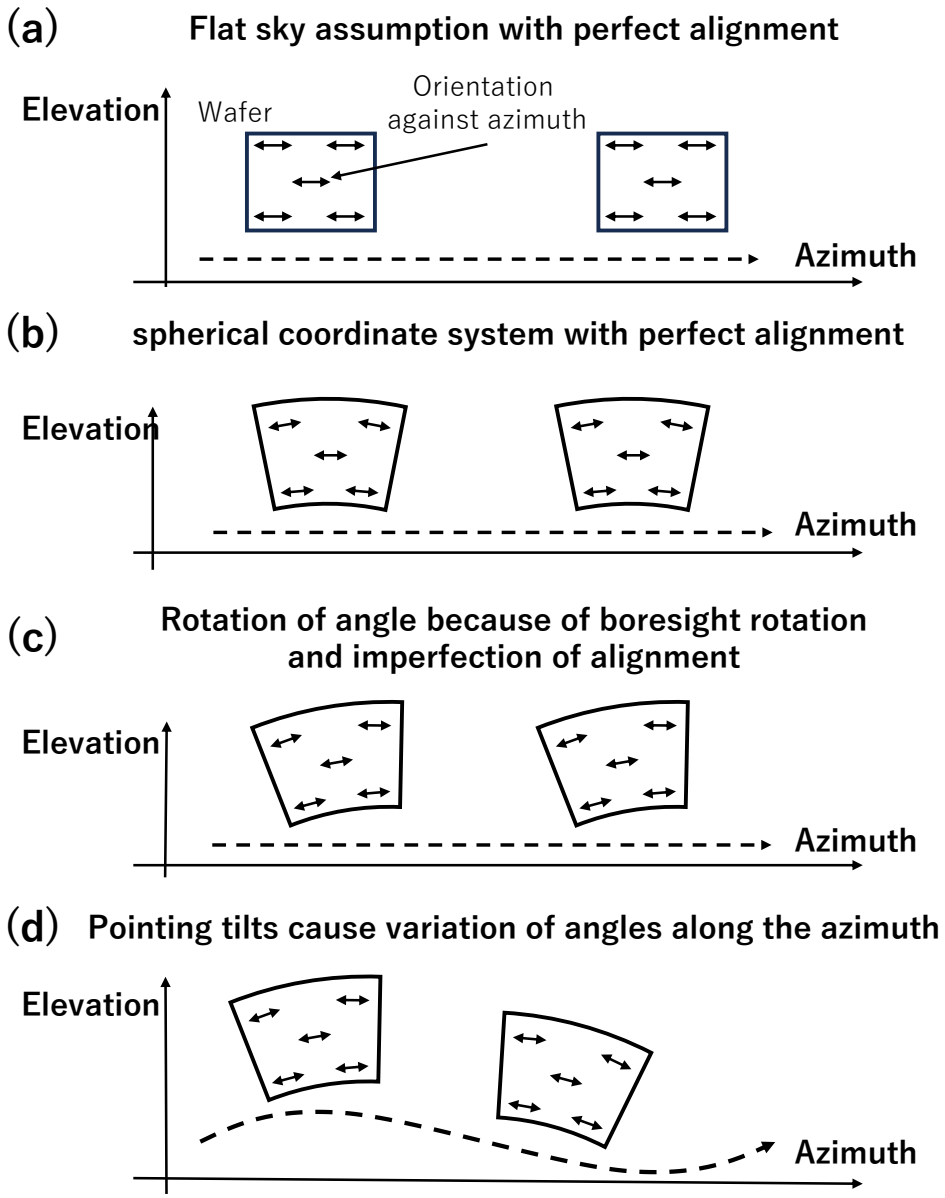

Figure 6.3: Projections of the detector wafer (square or circular sector) and the antenna orientations (arrows) in four different situations.

5, it introduces the pointing rotation along the azimuth motion.

6.3.3 Estimation of the polarization angle

Figure 6.4 illustrates the principle to estimate the polarization angle from the pointing. As described in section 6.3.2, the pointing along the same direction of the detector alignment is rotated from the azimuth. We estimate a rotation angle of the direction of the detector alignment (Ψ_r) by using their pointing as shown in Figure 6.4 (a). The rotation angle is determined as an angle between an azimuthal direction and a great circle that passes through the pointing of detectors on the detector alignment. We perform such an estimation for all detectors. We then correct the effect of the axes tilts by using the pointing information which was obtained in chapter 5. This corresponds to reconstruction of

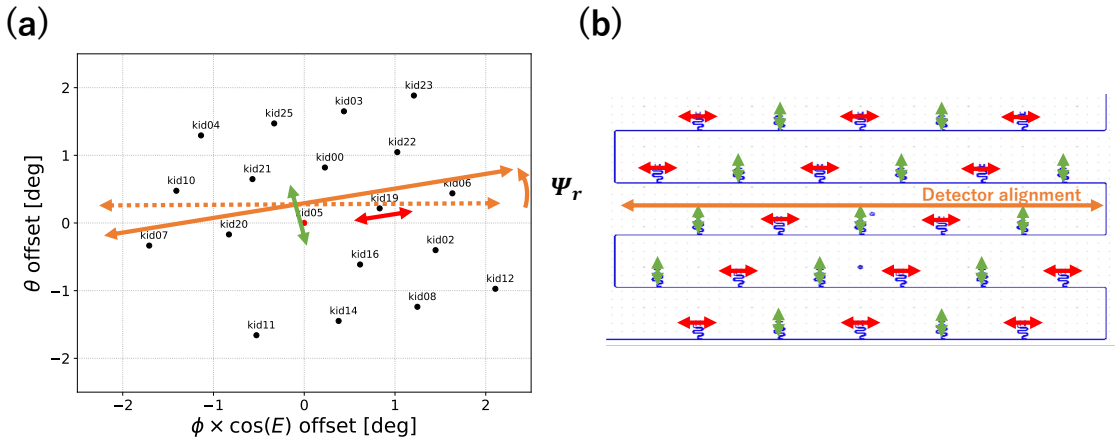

Figure 6.4: (a) Principle to estimate the rotation angle. The angle Ψ_r is a rotation from ϕ axis. Here, θ and ϕ are $90° - E$ and $-A$, respectively. We estimate Ψ_r by using pointing information in the horizontal coordinate system. (b) Antenna angles in the wafer design. All antenna angles were designed to parallel (red arrow) or perpendicular (green arrow) to the horizontal direction of the wafer (orange line). We assume the antenna orientations in the sky are the same angle (i.e., 0° or 90°) from the wafer direction.

Figure 6.3 (c) from the Figure 6.3 (d). We also calculate the rotation angle offset from the center detector (i.e., KID05) by using the collimation offsets obtained in chapter 5. After the correction of the rotation angle offset, we estimate the rotation angle of the wafer by using all detector information. We assume that the orientation of each antenna on the wafer is consistent with the design (i.e., 0° or 90°). This assumption allows us to estimate the rotation angle of the wafer by using the all detector information.

6.4 Polarization angle in the horizontal coordinate system

We extracted the rotation angle (Ψ_r) for each detector, separately. The polarization angles for each detector are illustrated in Figure 6.5. They are the same definition as the illustrated angles in Figure 6.2 (b). The angles of off–center detectors are rotated from the wafer center detector (KID05) because of the projection to the spherical sky. The pointing precision directly propagates to the angle precision in this calibration method. We estimated the error by using Monte Carlo (MC) simulation based on the pointing uncertainty.

- Add random offsets to the pointing with assuming the Gaussian distribution with sigma of $0.6'$ and $0.5'$ for the elevation and azimuth, respectively.
- Estimate the polarization angle with the same method as the real data.
- Take the differences of the polarization angle from that without any offset case.

The error for the center detector is lower than that of others. This is because we can use many detectors for the angle estimation for the center detector. For KID16 and KID02, they can only use two detectors each other. Thus, their errors are larger than others.

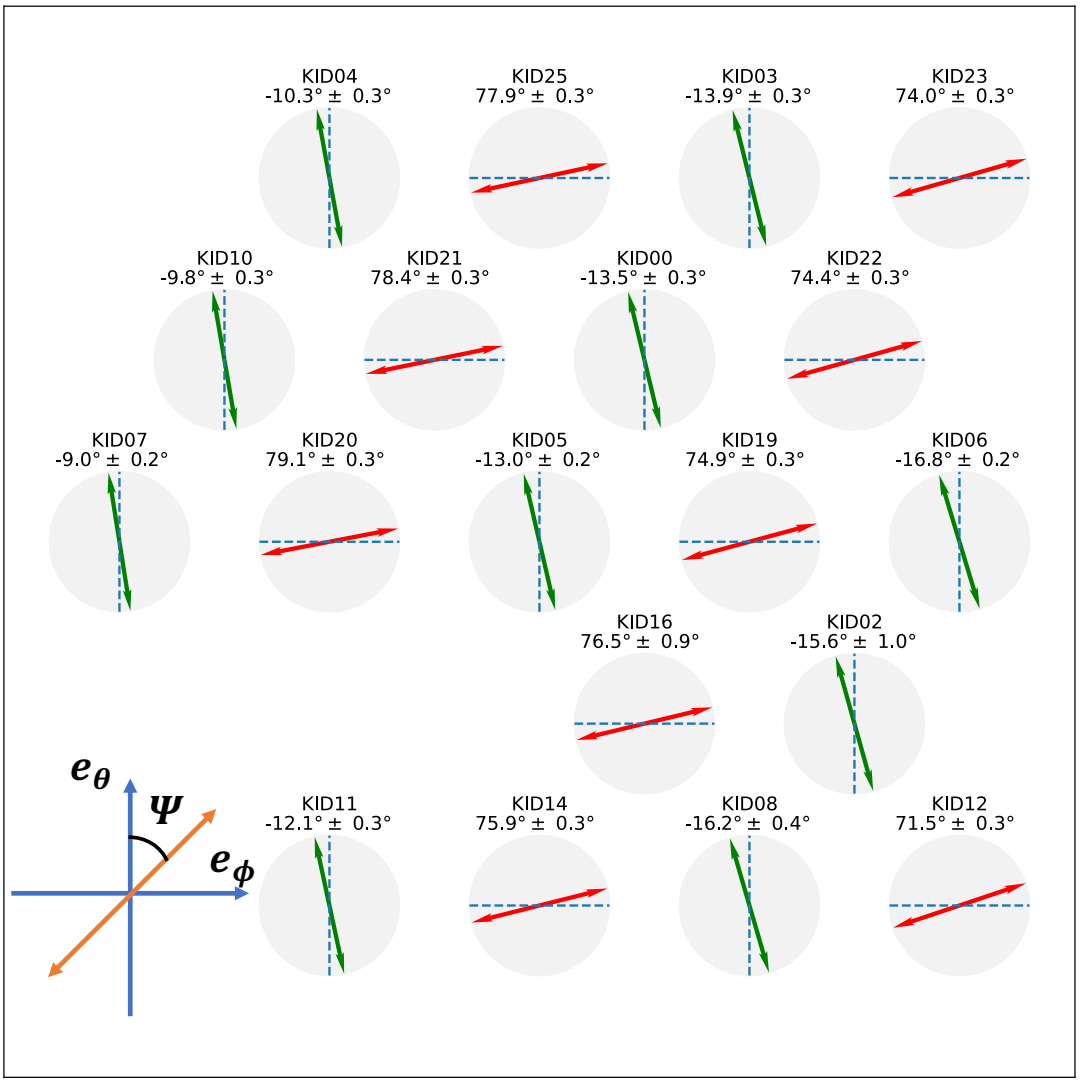

Figure 6.5: Obtained polarization angles in the horizontal coordinate system. Their values and uncertainties are written above each circle. The values are calculated by the obtained rotation angle (Ψ_r) and the antenna orientations in the wafer (i.e., 0° or 90°). The green or red colors correspond to each detector which has a parallel or perpendicular orientation of the antenna in the wafer, respectively. Each antenna orientation in the wafer is shown as a blue dashed line. The polarization angles follow the definition written in the left-bottom which is the same definition as Figure 6.2 (b). We evaluated the uncertainties due to the pointing uncertainty by using the Monte Carlo simulation written in the text.

We can numerically calculate the rotation angle offsets of the off-center detectors from that of the central detector based on the collimation offsets. By correcting with the calculated offsets, each detector angle can be converted to the wafer rotation angle. Figure 6.6 shows the wafer rotation angles from each detector. By taking the weighted average of them, we obtained a more precise angle than that from each detector: $\Psi_r = 13.11° \pm 0.07°$.

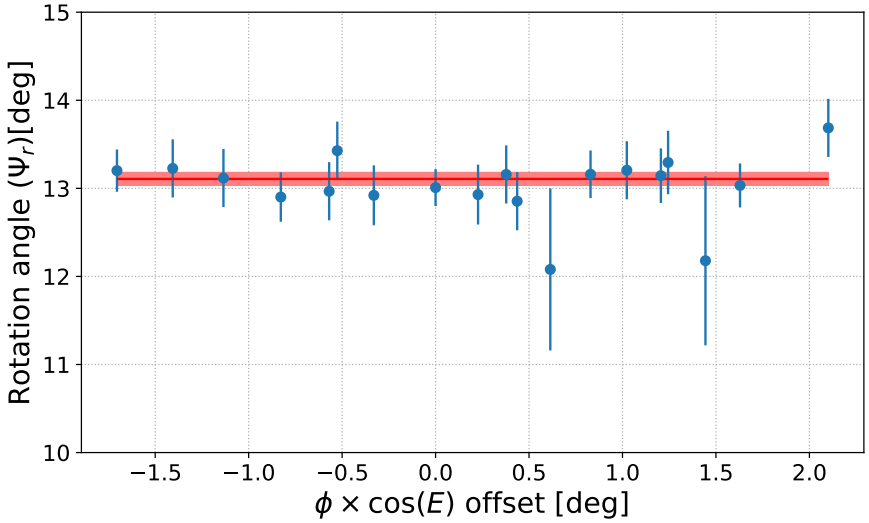

Figure 6.6: The rotation angles of the wafer after the correlation of the Ψ_r offset due to the collimation offsets. The errors were the same as in Figure 6.5. We obtained the weighted average of $\Psi_r = 13.11^\circ \pm 0.07^\circ$.

6.5 Translation from the horizontal coordinate system to the equatorial coordinate system

Both the pointing and the polarization angle in the horizontal coordinate system need to be translated to the coordinate system for the CMB analysis (e.g. equatorial coordinate). For the translation of the coordinate system, we have to take into account the precession, the nutation, polar motion, and aberration as explained in chapter 4.

The polarization angles in the equatorial coordinate system vary during the azimuthal scan unlike in the horizontal coordinate system as shown in Figure 6.7 (a). This is because the tangent plane in the equatorial system is changed during the azimuthal scan. For instance, if we scan at a constant elevation which is above the latitude of the telescope, the tangent plane in the equatorial system is rotated by 360° during one azimuthal scan. Figure 6.7 (b) shows an example of the polarization angles in the FK5 system for KID05. The polarization angle was changed from 0° to 360° because the fixed elevation (70°) was larger than the latitude ($\sim 23^\circ$) of the GroundBIRD telescope.

Astropy library can translate a pointing in the horizontal coordinate system (i.e., azimuth and elevation) to that in the FK5 system (i.e., right ascension and declination). For a translation angle between two coordinate systems (q), we also employ a translation method which is extended usage of the astropy. As shown in Figure 6.8, our translation method for the polarization angles, "Two-point translation", is composed of three steps:

1. In addition to the target pointing vector A_H, we define another pointing vector $A_H^{'}$ which is very close to A_H, $|A_H^{'} - A_H| \sim 10^{-4}$ degrees. We calculate an angle X as direction from A_H to $A_H^{'}$ as illustrated in Figure 6.8.

2. Translate both A_H and $A_H^{'}$ into the FK5 system by using astropy. Each point is named as A_E and $A_E^{'}$. In the FK5 system, we calculate an angle $X^{'}$ as a direction

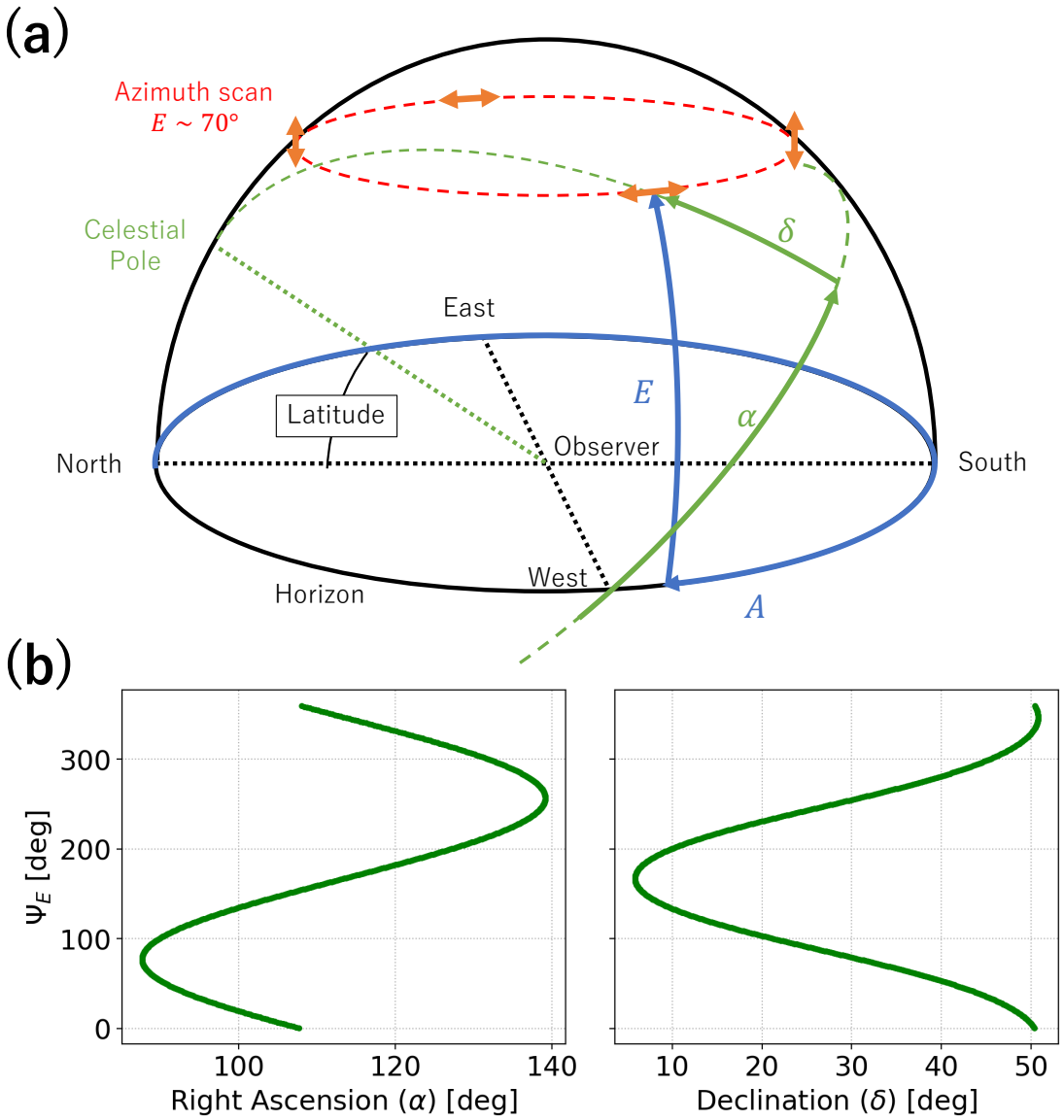

Figure 6.7: (a) Illustration of the constant elevation scan in the horizontal coordinate system. The polarization angle in the horizontal coordinate system is constant during the scan. On the other hand, the polarization angle in the equatorial coordinate system is not constant. This is because the tangent plane in the equatorial coordinate system is rotated during the scan. For instance, it is rotated by 360° for azimuth scan if the elevation is above the latitude of the telescope. (b) Estimated polarization angles in the equatorial coordinate (FK5) as a function of their right ascension and declination. We follow the angle definition as shown in Figure 6.2 (d). We found that the polarization angles in the equatorial coordinate were rotated by 360° for one azimuthal scan as expected.

from A_E to $A_E^{'}$ as well as the horizontal coordinate system.

3. We obtain the translation angle at each pointing : $q = X^{'} - X$.

Further details are described in appendix A.

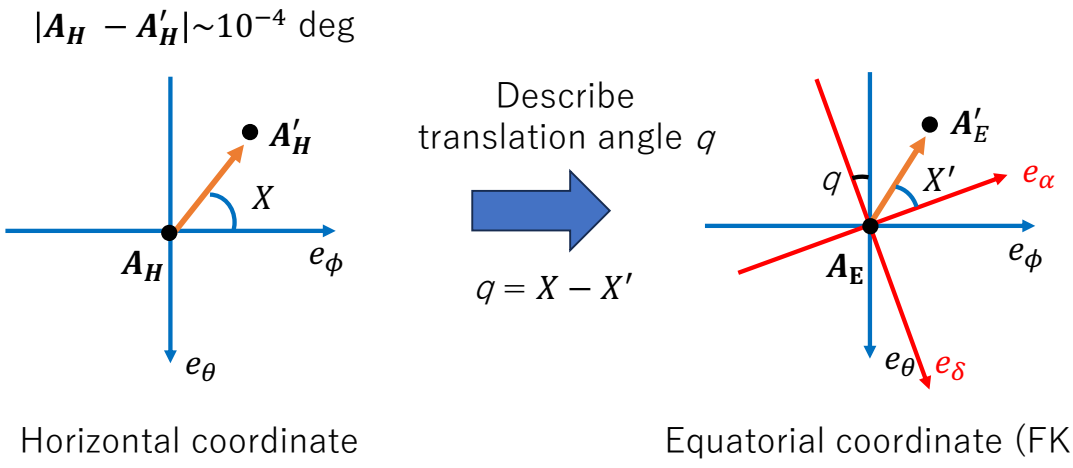

Figure 6.8: Overview of "two-points translation" method to determine a rotation angle q between horizontal coordinates and equatorial coordinates (FK5). We introduce new pointing (A'_H, A'_E) which are very close to the pointing (A_H, A_E). The angles (X, X') are calculated by using real pointing (A_H, A_E, A'_H, A'_E). The translation angle q is determined as angle difference between X and X'.

6.6 Systematic uncertainties

The systematic uncertainties of the pointing calibration were estimated as follows,

- Beam shape: This affects the pointing for each detector individually. The maximum angle difference 0.14° is estimated from the pointing uncertainty of 0.26′ when we use three detectors to estimate the rotation angle (Ψ_r).
- Moon position: This affects the pointing for each detector simultaneously and relative pointings are the same. Therefore, this effect is negligible to estimate the rotation angle.
- Elevation and azimuth encoders: This is negligible because of the same reason as the Moon position.
- Ambient temperature: This is the same as the beam shape. The maximum angle difference of 0.22° is estimated from the pointing uncertainty of 0.40′ with the three detectors.
- Mechanical variation: This is also negligible because of the same reason as the Moon position.
- Non-uniformity: This is also negligible because of the same reason as the Moon position.

The wafer was fabricated with 0.1 μm uncertainty. Based on this uncertainty, we estimate possible rotation of the antenna orientation from the design by 0.013°. "Two-points translation" also had an uncertainty of $1^\circ \times 10^{-6}$. This is the maximum difference between rotation angle as an input and obtained rotation angle based on this method. Details of this study are described in appendix A.

Table 6.2: Systematic Uncertainty for the polarization angle

Pointing	0.26°
Wafer fabrication	0.013°
Two-points translation	$\sim 1 \times 10^{-6}$
total	0.26°

We summarize the systematic uncertainties of the polarization angle in Table 6.2. In total, we assigned 0.26° as the systematic uncertainty due to the systematic uncertainties of the pointing calibration. We calculate the square root of the quadrature sum of statistical error (0.07°) and systematic error (0.26°). It was 0.27°, which is below the requirement (0.43°).

6.7 Summary and Discussions

We proposed the new calibration method for the polarization angle using pointing information. Achieved precision is 0.27° including the systematic uncertainties. This is lower than our requirement (0.43°).

In this method, we have not included any effect related to the mirrors, e.g., possible rotation of the polarization angle. We have to validate this method by using conventional methods, such as artificial polarized sources or Tau A. This is a future study.

In future CMB experiments, they could reduce the statistic uncertainty due to many detectors. In the case of many detectors, it needs a lot of time to calibrate each polarization angle by using Tau A. We need to accumulate data to calibrate the polarization angle precisely due to its faint signal. Our method is useful for such a case. Therefore, this method has the potential to achieve accurate calibration of the polarization angle in a short time for future CMB experiments.

Chapter 7

Noise Study

The raw data comprises various components: CMB, external radiations, instrumental noise, and so on. The strategy of the CMB analysis is keeping high efficiency for CMB whereas suppressing the effects of non-CMB components. For this purpose, we apply filters to TOD as pre-steps of the map making. To construct and/or choose good filtering methods, characterization of the noise (i.e., non-CMB components) is important. A goal of this study is that the transfer function is kept as high as possible whereas reducing the noise to be white noise level. The origin of the white noise for ground-based telescopes is mainly photon fluctuation of the atmospheric radiation, which is the minimum noise level we can achieve. In this chapter, we describe this analysis with real data taken by the GroundBIRD telescope. We also evaluate performances of considered filters including their impact to the power spectrum estimation.

7.1 Real data analysis

We show the analysis overview in Figure 7.1, again. We apply calibration results in the map making process. The pointing information is also used for filtering the raw data. The noise is characterized using the real TOD and the simulation. We consider the noise filtering methods according to this knowledge. Then, we evaluate the noise suppression based on the real data. For instance, we compare the noise spectra before and after each filtering. We calculate the transfer functions by using the simulation data which only contains CMB signal. The transfer function is obtained as the ratio of the power spectra between filtered data and unfiltered data.

7.1.1 Data selection

The dominant signal into the telescope is the atmospheric radiation. All detectors observed the same sky region in a short time scale. Thus, the TODs for each detector are highly correlated as shown in Figure 7.2 (a). Four of them do not correlate with others. We suspect the un-correlation is one of the evidence for failure of preprocessing such as the off–resonance subtraction. The Pearson correlation coefficient characterizes the correlation

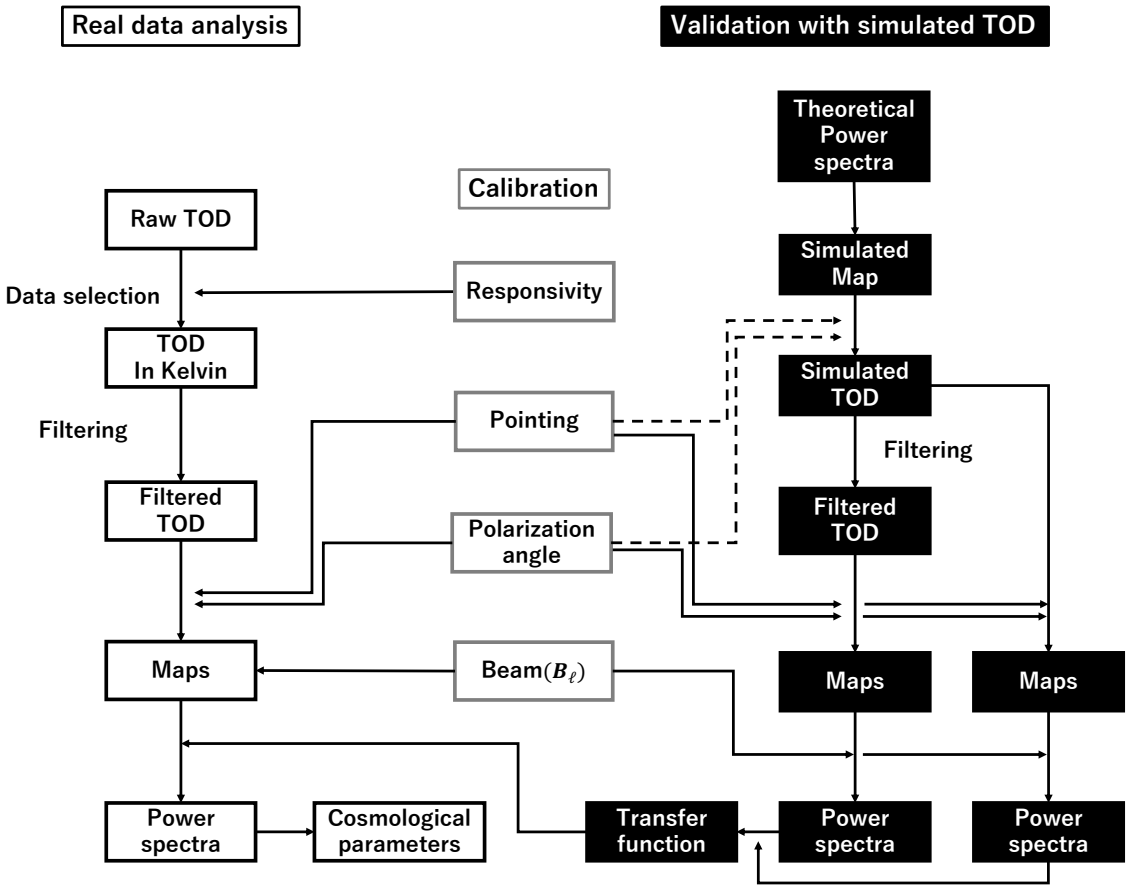

Figure 7.1: Overview of data analysis flow. This is the same as Figure 4.5. At first, we apply data selection to "Raw TOD" (raw data). Then, we calibrate the responsivity for each detector. In this process, we convert the units to Kelvin from MKID's phase. We apply filters to TOD for suppressing the noise effects. The I, Q, and U maps are obtained from the filtered TOD with the pointing and polarization angle information. To estimate power spectra from the maps, we need to validate a transfer function and a beam window function (B_ℓ). The beam window function is calculated from the calibrated beam information. We validate the transfer function by using simulated TOD which includes only CMB signal. In the simulation, we make simulated maps based on the theoretical power spectra. These maps are smeared by the beam. Using the same pointing and polarization angle information as real data analysis, we generate simulated TOD. We then apply the same analysis processes (filters, map-making, power spectrum estimation) as real data analysis. We also calculate power spectra without the filtering process. We evaluate the transfer function by comparing these two power spectra. We estimate the power spectra by using the transfer function and the beam window function (B_ℓ).

of two TODs as

$$r_{xy} = \frac{\sum_{i=1}^{n}(x_i - \bar{x})(y_i - \bar{y})}{\sqrt{\sum_{i=1}^{n}(x_i - \bar{x})^2}\sqrt{\sum_{i=1}^{n}(y_i - \bar{y})^2}}, \tag{7.1}$$

where x_i and y_i are the TODs which we want to compare, and n is the number of data samples in each observation. Before calculating the correlation coefficient, we down-sampled each TOD with a sampling rate of 10 Hz for reducing the effect of white noise. Then, we calculated the correlation coefficient for each detector combination as shown in Figure 7.2 (b). We selected detectors which had a median correlation coefficient larger than 0.95. This criterion eliminates 4% of data. Figure 7.3 shows the hitmap from the selected data. This selection does not make regions where the number of hits is significantly small.

7.1.2 Relative responsivity calibration

Selected TODs were highly correlated. We calibrated relative responsivities among them by minimizing their differences. Afterward, we convert the relative responses to absolute temperature based on the Moon observations.

7.1.3 Offset subtraction

The raw TODs (i.e., phase response) after the correction described in section 3.4 have individual offsets. We subtracted this individual offset by using the average of each TOD (i.e., 1 hour TOD). The offset subtraction does not reduce the transfer function because we measure the CMB anisotropy.

7.1.4 Common mode noise subtraction

As shown in Figure 6.4 (b), orthogonal antenna directions are assigned to detectors alternately. Because of the azimuthal scan with a fixed elevation, each detector on the same detector alignment observes the same sky region at different times. We can obtain polarization signals by subtracting the TODs taken by different detectors whose antenna directions are orthogonal. This subtraction removes unpolarized atmospheric radiation simultaneously. To subtract the unpolarized atmospheric radiation by using two TODs ($y_1(t)$ and $y_2(t)$) taken by different detectors, we need to consider the collimation offsets. For instance, neighbor detector pairs have approximately azimuth offset of 0.8° as described in chapter 6 (see Figure 6.4). To take it into account, we subtract y_2 from y_1 with timing offset (δt),

$$y_d(t, \delta t) = y_1(t) - y_2(t + \delta t). \tag{7.2}$$

The azimuth offset of 0.8° corresponds approximately $\delta t = 40$ ms. When we apply timing offset between two TODs, we can subtract the signal from the same sky (azimuth). Figure 7.4 (a) shows power spectrum densities (PSDs) calculated from subtracted TOD ($y_d(t, \delta t)$) with three timing offsets ($\delta t = 0, 50, 100$ ms). We found wave shapes at 10 Hz–100 Hz in the case of $\delta t = 50, 100$ ms. This suggest the existence for a common mode noise (i.e. time synchronous noise).

We reproduce the wave shapes by using simulated TOD which consists of common noise ($y_{\rm com}$) and individual noise ($y_{\rm ind}$). The noise spectrum is modeled as follows,

$$N(f) = \sigma_w \left[1 + \left(\frac{f}{f_{\rm knee}}\right)^{\alpha}\right], \tag{7.3}$$

where σ_w is the white noise level, α is an index of slope at a lower frequency, $f_{\rm knee}$ is a knee frequency. The knee frequency is defined as a frequency where the amplitude of the

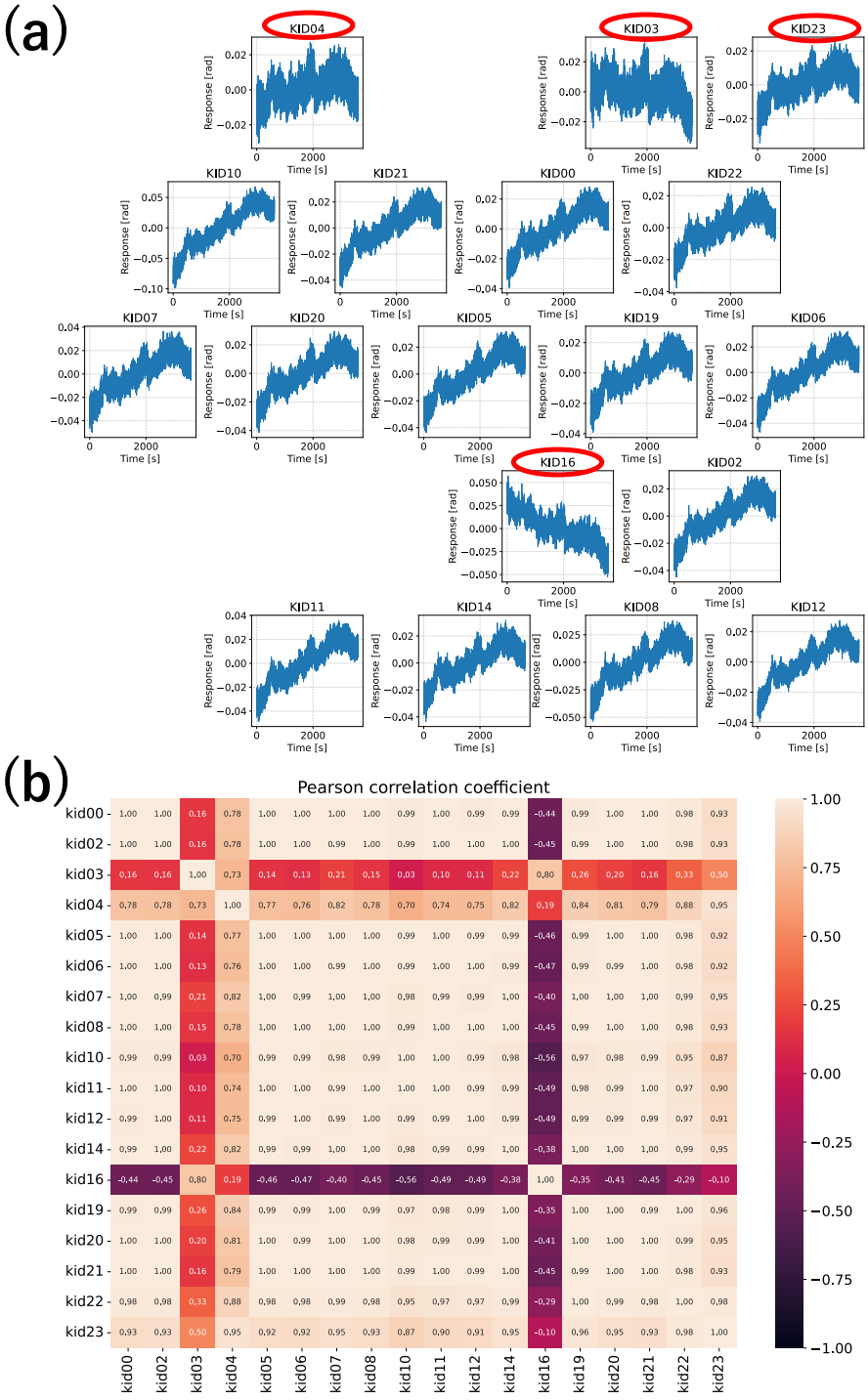

Figure 7.2: (a) Raw TODs of all detectors for 1 hour. We found that almost all detectors have the same trend (high correlation), but four detectors denoted by red circle (e.g., KID16) have different trend (low correlation). (b) Pearson correlation coefficients for all detector combinations calculated from down-sampled raw TODs at 10 Hz sampling rate. In this observation, we selected the detectors except for KID03, KID04, KID16, KID23 based on the criteria (median correlation coefficients > 0.95).

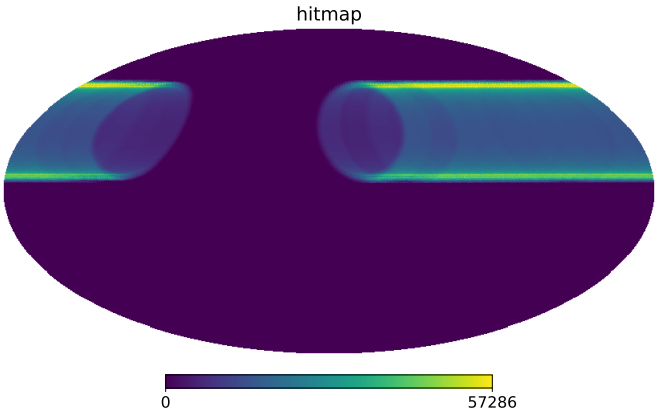

Figure 7.3: Hit map of selected data. Hit map is defined as the amount of data in each pixel. There are few hit regions at the edges of the observed region. Regions at the beginning and end of the right ascension (horizontal) direction also have few hits (oval-like regions). We did not use these regions to estimate the power spectrum as described in section 7.1.7. We made this map by healpy with $N_{\rm side} = 128$ in the FK5 system.

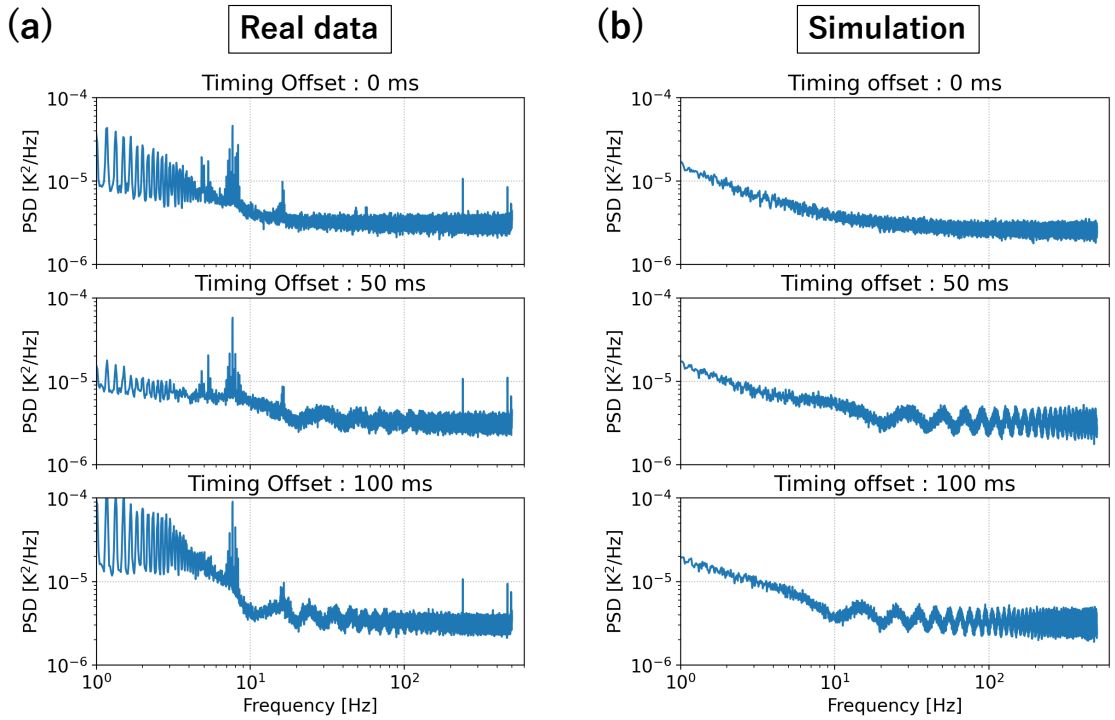

Figure 7.4: PSDs comparison with three timing offsets to confirm the existence of the common mode noise. (a) PSDs calculated from the subtracted TODs with timing offsets (0, 50, 100 ms) in real data analysis. (b) PSDs calculated from the subtracted TODs with timing offsets (0, 50, 100 ms) in the simulation. In this simulation, we assumed two components: common noise and individual noise. They are realized by using Eq. (7.3). We realized the individual noise with $\sigma_w = 800\ \mu\mathrm{K} \cdot \sqrt{s}$, $f_{\rm knee} = 5$ Hz, $\alpha = -2$. For the common mode noise, we used $\sigma_w = 400\ \mu\mathrm{K} \cdot \sqrt{s}$, $f_{\rm knee} = 5$ Hz, $\alpha = -1$. Both trends are the same. The wave periods correspond to $1/\delta t = 20, 10$ Hz.

white noise and 1/f noise are the same. The 1/f noise is frequency-dependent noise, and it is higher at the lower frequency region. We simulated two TODs ($y_1^{\rm sim}, y_2^{\rm sim}$) based on this model as follows,

$$y_i^{\rm sim}(t) = y_{\rm com}^{\rm sim}(t) + y_{\rm ind,i}^{\rm sim}(t), \tag{7.4}$$

where $i = 1, 2$. We assign the individual noise with $\sigma_w = 800\ \mu{\rm K}\cdot\sqrt{s}$, $f_{\rm knee} = 5$ Hz, $\alpha = -2$. We assign the common mode noise with $\sigma_w = 400\ \mu{\rm K}\cdot\sqrt{s}$, $f_{\rm knee} = 5$ Hz, $\alpha = -1$. Then, we subtracted $y_2^{\rm sim}$ from $y_1^{\rm sim}$ with the same timing offset ($\delta t = 0, 50, 100$ ms). Figure 7.4 (b) shows PSDs calculated from the subtracted TODs ($y_1^{\rm sim}(t) - y_2^{\rm sim}(t+\delta t)$) with three timing offsets (0, 50, 100 ms). They also have wave shapes at 10 Hz–100 Hz in the case of $\delta t = 50, 100$ ms. Their wave periods correspond to $1/\delta t$. This behavior is consistent with our expectations. Further details of this study are written in appendix B.

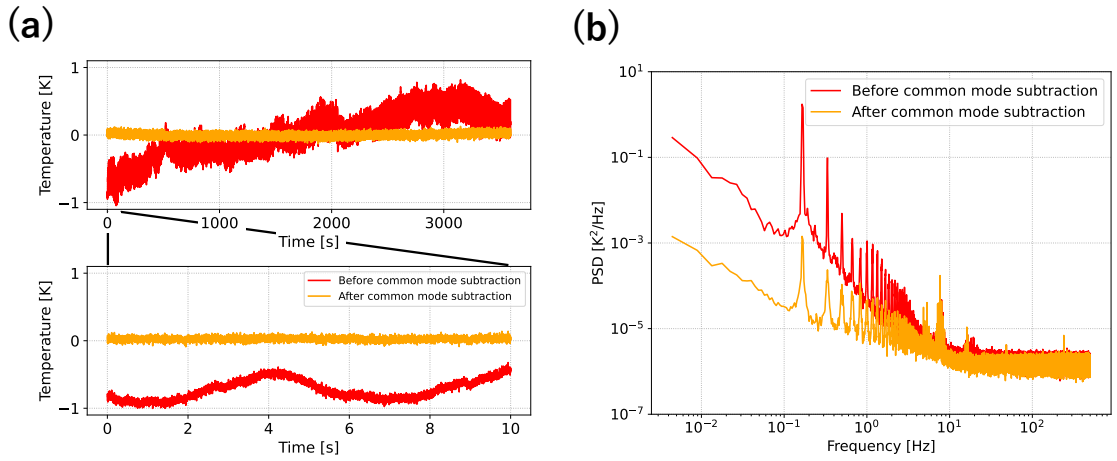

Figure 7.5: (a) TODs before and after the common mode subtraction for one observation (i.e., 1 hour) and for 10 seconds. The TOD before the common mode subtraction was periodic with respect to the azimuth scan (1 rotation per 6 seconds). It also had large drifts. Both are suppressed by the common mode subtraction. (b) PSDs calculated from (a). At a low frequency region, 1/f noise and scan synchronous were dominated in both PSDs. The common mode subtraction suppressed them by approximately two orders of magnitude at a lower frequency region.

We calculated the common mode noise by taking the average of TODs for all detectors. Then, we subtracted it from each detector's TOD. Figure 7.5 shows the comparison of TODs before and after the common mode subtraction. Unprocessed TOD has large drifts due to the fluctuation of atmospheric radiation in a long time scale. In a short time scale, the TOD before the common mode subtraction was periodical, which represented the sky structure. After the common mode subtraction, the large drifts as well as periodical fluctuation in a short time scale are highly suppressed. RMS of the TOD after the common mode subtraction was one order of magnitude lower than that before the subtraction. The comparison of PSDs is also shown in Figure 7.5. The 1/f noise and scan synchronous are dominated in a lower frequency region. Scan synchronous is a noise component that is synchronous to the scan. The atmospheric radiation remains almost the same after one azimuth scan because of our fast scanning. This is the origin of the scan synchronous. When the rotation speed is 10 RPM, the scan synchronous appears as a peak at 0.17 Hz

and its harmonics as shown in Figure 7.5 (b). The common mode subtraction reduced them by approximately two orders of magnitude at the sub–Hz region.

7.1.5 Each scan filter

After the common mode subtraction, baseline drifts in a long time scale still remained. We subtract baseline drifts at longer time scale than one azimuth scan as follows,

- divide the TODs into each azimuthal scan.
- fit each TOD with the linear function.
- subtract the fitted values from the TODs.

We call this filtering as "Each scan filter". Figure 7.6 shows the comparison of data before and after each scan filter. We reduced the noise at a longer time scale than one azimuth scan (i.e., at lower frequency than 0.17 Hz in the PSD). This correction reduced the RMS of the TOD by 10%.

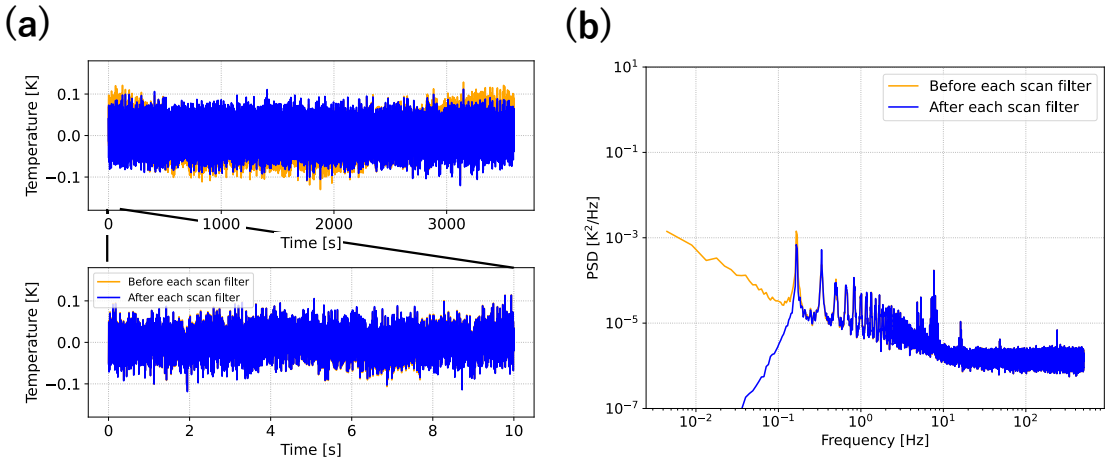

Figure 7.6: (a) TODs before and after each scan filter for one observation (i.e., 1 hour) and for 10 seconds. Each scan filter reduced the baseline drifts in a long time scale. (b) PSD calculated from (a). Each scan filter reduced noise components below the scanning frequency (0.17 Hz).

7.1.6 Map-making

Figure 7.7 shows binned Q and U maps in the FK5 system reconstructed from three TODs:

- TOD before the common mode subtraction.
- TOD after the common mode subtraction.
- TOD after each scan filter in addition to the common mode subtraction.

Each map has a striped shape along the right ascension direction because of a lack of variety for the polarization angle in these pixels. We designed only two antenna orientations in

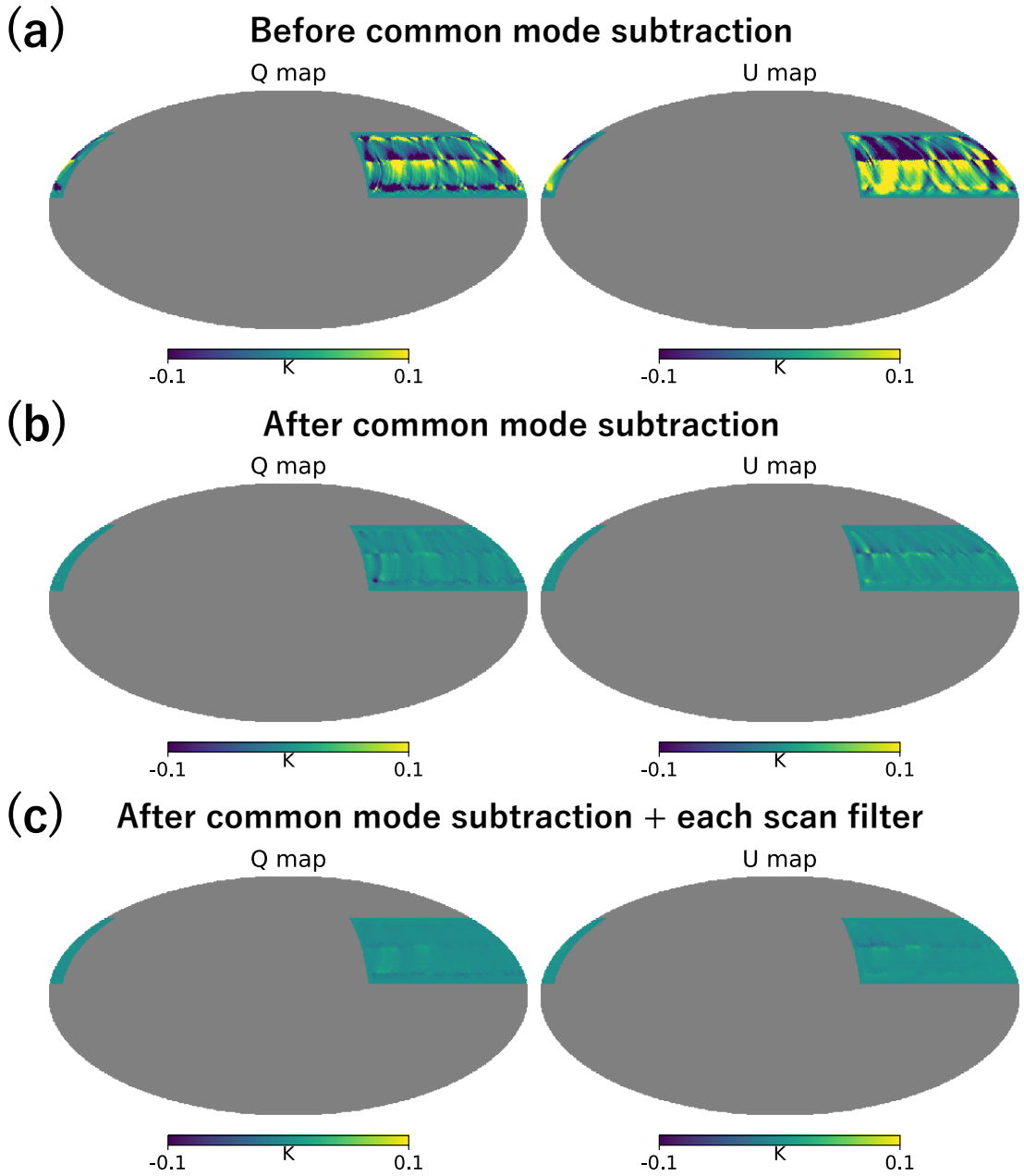

Figure 7.7: (a) Q and U maps reconstructed from TOD before the common mode subtraction. (b) Q and U maps reconstructed from TOD after the common mode subtraction. (c) Q and U maps reconstructed from TOD by applying each scan filter in addition to the common mode subtraction. These maps have been already applied by the mask which is described in section 7.1.7

the wafer as described in chapter 6. This is the reason for the lack of variety. RMSs of Q and U maps before the common mode subtractions were 83 mK and 118 mK, respectively. After the common mode subtractions, the RMSs were 8.5 mK and 9.5 mK which are one order of magnitude lower than that before the subtraction. When we applied each scan filter, the RMSs were 4.2 mK and 4.4 mK. We reduced the RMS by 50% with each scan filter.

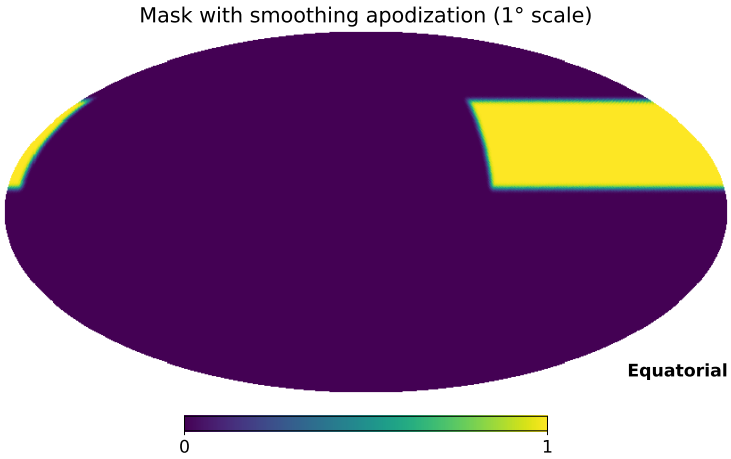

Figure 7.8: Mask map used in this study with apodization scale of 1°. We selected well observed region at $7^\circ \leq \delta \leq 50^\circ$ and $170^\circ \leq \alpha \leq 300^\circ$.

7.1.7 Power spectrum estimation

We estimated the noise power spectrum from their maps from Eq. (4.13) as described in section 4.4.6. As shown in Figure 7.3, we had a few hits (i.e., data samples) around the edge of the observed area. Regions at the beginning and end of the right ascension (horizontal) direction also had few hits (oval-like regions) because we scanned these regions once. To select well observed region, we made the mask at $7^\circ \leq \delta \leq 50^\circ$ and $170^\circ \leq \alpha \leq 300^\circ$ in the FK5 system. We applied a smoothing with 1° scale to the mask (this is known as apodization) as shown in Figure 7.8. We used an inverted covariance matrix of intensity for pixel weighting to estimate the power spectra. This matrix was calculated with respect to the weight for each TOD (i.e. inversed white noise level) and the number of hits in each pixel.

Figure 7.9 shows the noise power spectrum for each TOD. The noise spectrum after the common mode subtraction was two orders of magnitude lower than that before the subtraction. After applying each scan filter, we further reduced the noise spectrum by approximately 25%. We also show a white noise spectrum, which is calculated from white noise only TOD. We assumed the same white noise level as the real data. The noise spectrum after all filtering processes was still high compared to the white noise spectrum. Development of further filters is a future work.

7.1.8 Transfer function

We evaluated the transfer function for three filtering processes by using simulated TOD which only contains CMB signal. To evaluate their transfer function precisely, we performed the evaluation for 20 realizations of CMB maps. Figure 7.10 shows a comparison of the transfer functions. The transfer function of the offset subtraction is consistent with 1, which is no loss of the CMB anisotropy. After the common mode subtraction, the transfer function became small around $\ell \sim 250$. These multipoles correspond to the sub-degree scales, which is a similar scale to the collimation offsets (0.85°). The minimum value was 0.86 at $242 \leq \ell \leq 251$. Each scan filter slightly reduced the transfer function. It was

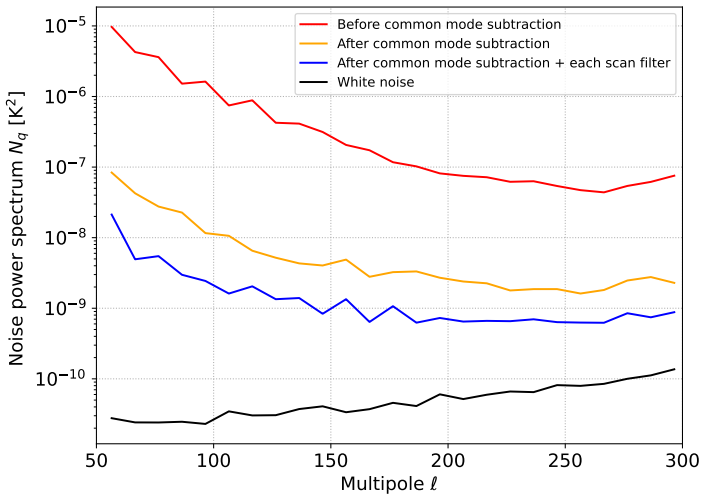

Figure 7.9: Noise power spectrum for each TOD. We also show a white noise spectrum, which is calculated from white noise only TOD. The beam window function increases the power at higher multipole regions. After the common mode subtraction and each scan filter, we reduced the noise spectrum by approximately three orders of magnitude. It was still higher than the white noise spectrum.

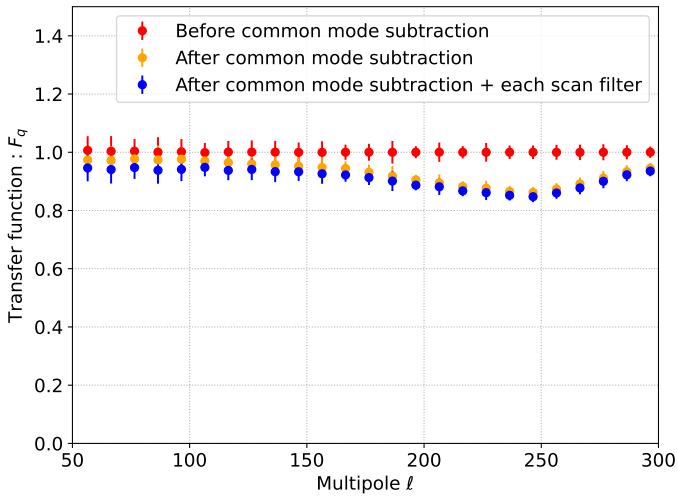

Figure 7.10: Transfer functions for each filtering process. When we applied the offset subtraction, the transfer function was consistent with 1. After the common mode subtraction, it became lower around $\ell \sim 250$ which is similar scale of the collimation offsets (0.85°). Each scan filter slightly reduced the transfer function (typically 2%).

typically 2%.

7.2 Summary and Discussions

We developed the analysis pipeline as well as the validation pipeline. By using these pipelines, we characterized the noise. To suppress the noise effects, we adopted three processes in sequence: the offset subtraction, the common mode subtraction, each scan filter. We reduced the noise by approximately three orders of magnitude at lower multipole regions by applying the common mode subtraction and each scan filter. We could not achieve to reduce the noise to be the white noise level in this thesis. We also evaluated the transfer function for each filtering process. We confirmed these processes maintain the transfer function ≥ 0.85. This is higher than that achieved in previous experiments [104, 110].

In other CMB experiments, the transfer functions of EE and BB power spectra are almost the same level [104, 110]. If we assume that we can obtain the same transfer function to BB, it is approximately 0.94 at the peak of primordial B-modes ($\ell \sim 100$). These filtering processes reduced the CMB anisotropy by only 6% while they suppressed noise by three orders of magnitude.

In this study, the knee frequency of the 1/f noise is above the scanning frequency (0.17 Hz) and the scan synchronous still remained. These are the reasons that the noise power spectrum is two–three orders of magnitude higher than the white noise spectrum. To reduce the scan synchronous, we also evaluated an azimuth filter. The azimuth filter consists of three steps:

- divide TODs into azimuth bins with the bin width of 4° every azimuthal scan.
- take a running average of every 10 azimuthal scans to make an azimuth template.
- subtract the azimuth template from the TODs.

We applied the azimuth filter after the common mode subtraction. Figure 7.11 shows the comparison of the data before and after the azimuth filter. As shown in Figure 7.11 (b), this filter reduced the scan synchronous. The noise power spectrum in Figure 7.11 (c) was reduced by one–two orders of magnitude. In particular, the noise reduction is significant at a lower multipole region. The 1/f shape in the noise spectrum was successfully suppressed. On the other hand, the azimuth filter reduced the transfer function drastically as shown in Figure 7.11 (d). For instance, the transfer function is 0.1 at $\ell \sim 100$. We need to develop a better appropriate filter which keeps a high transfer function. We plan to develop a filtering considering time and space variation of the atmosphere conditions to reduce the scan synchorous. We also plan to develop a map making algorithm based on Likelihood method to reduce the 1/f noise (e.g., destriping technique [83, 84]). Even though we cannot achieve to reduce the noise to be the white noise level, we can estimate the unbiased power spectra by using cross-correlation between different day map. In the cross-correlation, the noise bias in Eq. (4.13) is dropped because the noise at different day is not correlated [111]. To reduce uncertainty of the unbiased power spectra estimated by the cross-correlation, it is also important to reduce the noise.

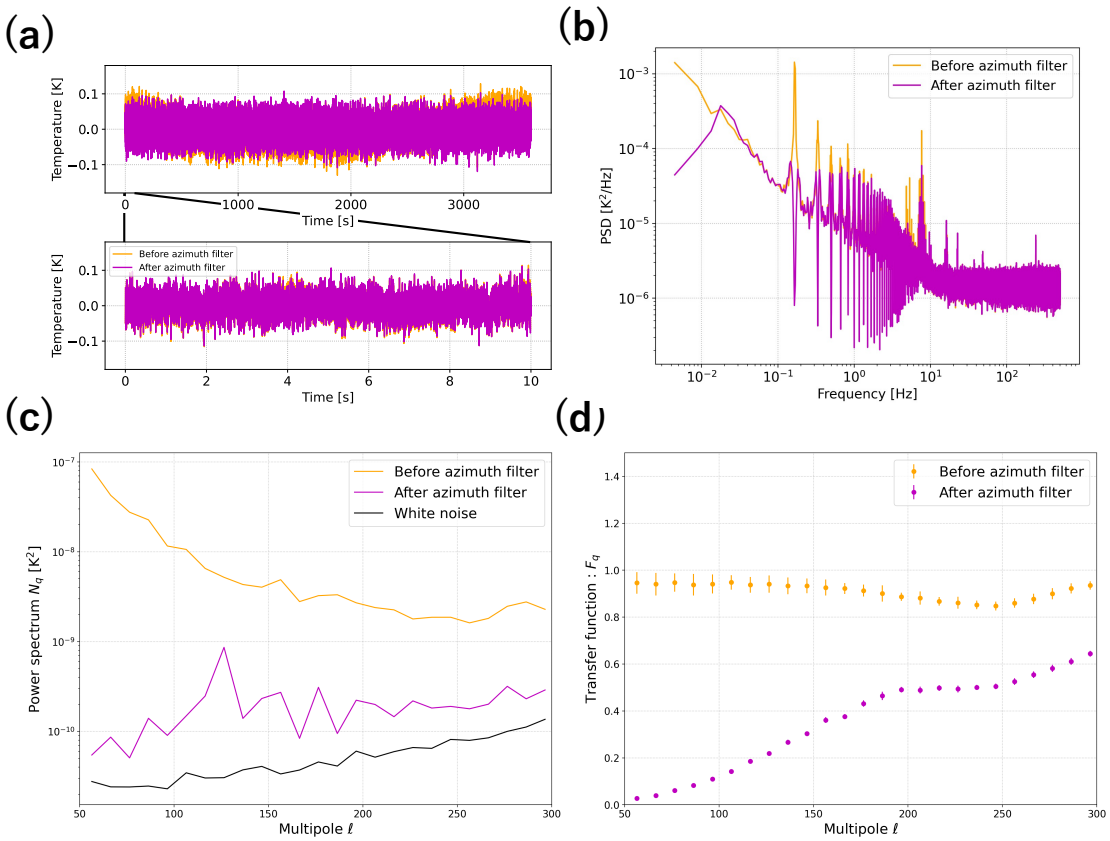

Figure 7.11: The comparison of the data before and after the azimuth filter. We applied the azimuth filter after the common mode subtraction. (a) TOD comparison. Long drifts was reduced because the azimuth template was made and subtracted for every azimuth scan. (b) PSD comparison. The azimuth filter reduced the scan synchronous. (c) Noise power spectrum comparison. The noise level after the azimuth filter was one–two orders of magnitude lower than that before the filter. In particular, the multipole dependence of it was similar to the white noise. We reduced the 1/f type component in the power spectrum. (d) Transfer function comparison. The azimuth filter reduced the transfer function drastically as well. We need to develop better filtering which can keep high transfer function.

Chapter 8

Discussions and Future Prospects

In previous chapters, we calibrated the pointing and the polarization angle. We summarize their requirements and achieved uncertainties in Table 8.1. In this chapter, we evaluate the impacts of each achieved uncertainty to science targets (i.e., optical depth and primordial gravitational waves) quantitatively. We use the developed analysis pipeline to evaluate them. We also summarize the remained issues of our study and discuss the future prospects.

Table 8.1: Requirements and achieved uncertainties of the calibration for the pointing and polarization angle.

Calibration	Requirement	Achievement
Pointing	$4.7'$	$3.3'$
Polarization angle	0.43°	0.27°

8.1 Pointing calibration

For the pointing calibration, we set the requirement of $4.7'$ to suppress its impact to a sufficiently small level for the B-modes and E-modes measurements. It corresponds to the tensor-to-scalar ratio (r) of 0.001. For E-modes measurement, it was two orders of magnitude lower than the E-modes signal calculated from ΛCDM. In this thesis, we performed the pointing calibration by using the Moon observation data. We successfully achieved the uncertainty of $3.3'$ which is lower than our requirement.

The pointing uncertainty effectively makes an effect of losing the beam resolution. We estimate its impact with respect to the beam window function (B_ℓ) as [112],

$$B_\ell^{\rm eff} = B_\ell e^{\frac{-\ell(\ell+1)}{2}\sigma^2}, \tag{8.1}$$

where σ is the uncertainty of the pointing calibration. Figure 8.1 (a) shows the effective beam window function for $3.3'$ uncertainty. As described in section 4.4, the beam window function is used to estimate the true power spectrum. Considering its dependence ($\widetilde{C_\ell} \propto B_\ell^2 C_\ell$), this uncertainty introduces uncertainty of the unbiased power spectrum (C_ℓ) based on the MASTER technique, which is less than 8% at $\ell \leq 300$ as shown in Figure 8.1 (b).

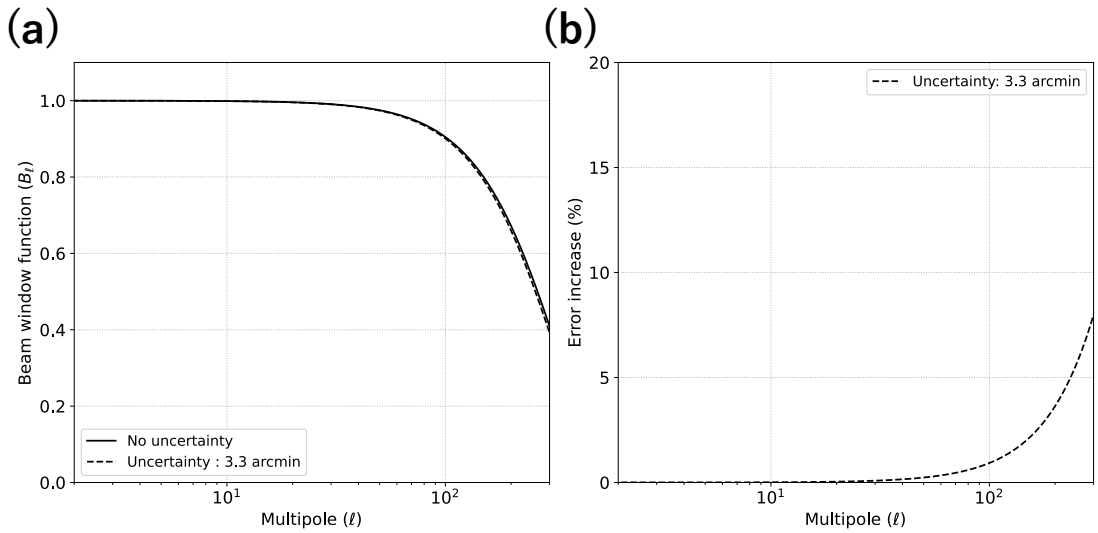

Figure 8.1: (a) Effective beam window function ($B_\ell^{\rm eff}$) for uncertainty of $3.3'$ and the beam width with no uncertainty (B_ℓ) as a function of multipole. (b) Uncertainties in the power spectrum based on the beam window function dependency of the power spectrum ($\widetilde{C_\ell} \propto B_\ell^2 C_\ell$).

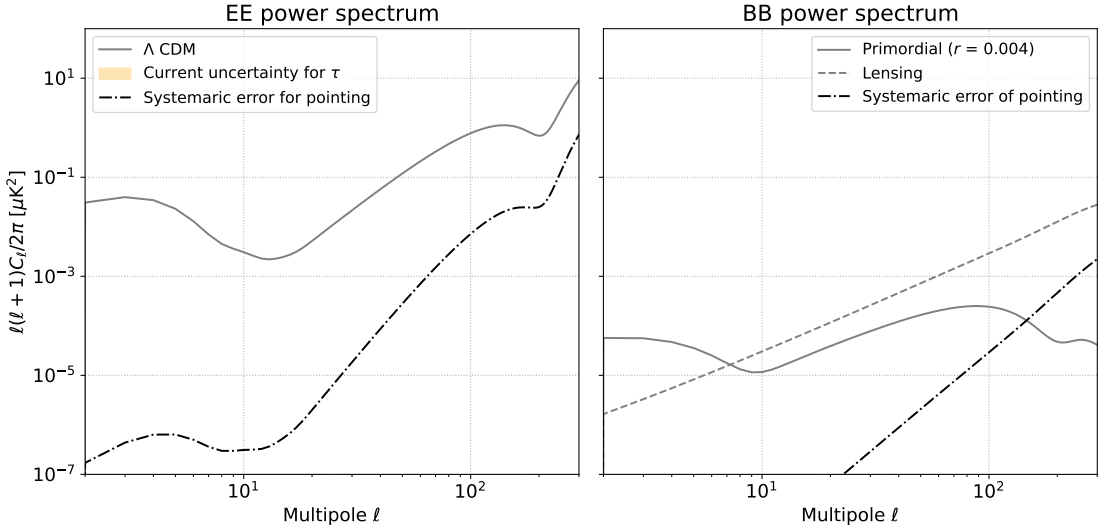

Figure 8.2: Systematic uncertainties of the EE and BB power spectra from the pointing calibration. We also plot the theoretical power spectrum (gray line) based on the best-fit values determined by Planck in the EE power spectrum. The systematic uncertainty of EE is four orders of magnitude smaller than the CMB power spectrum. It is two orders of magnitude smaller than the current uncertainty for τ based on $C_\ell^{EE} \propto \tau^2$. For the BB power spectrum, we also plot the primordial BB of $r = 0.0005$ (gray line) and the lensing BB (gray dashed line). The systematic uncertainty of BB corresponds to the level of the primordial BB of $r = 0.0005$ at its peak ($\ell \sim 100$).

Based on the uncertainty in the power spectrum, we evaluated the systematic uncertainty of the EE and BB power spectra as shown in Figure 8.2.

Optical depth As described in section 1.4.1, EE power spectrum at $\ell \leq 10$ depends on τ^2. The uncertainty of the EE power spectrum is approximately four orders of magnitude lower than the EE power spectrum from ΛCDM. Therefore, the systematic uncertainty from the pointing introduces 1% uncertainty to the optical depth. This is one order of magnitude lower than the current uncertainty [44].

Primordial gravitational waves The primordial BB power spectrum is proportional to the tensor-to-scalar ratio r. It has a peak around $\ell \sim 100$. Around the peak, the uncertainty of the BB power spectrum corresponds to the primordial BB power spectrum of $r = 0.0005$. This is two orders of magnitude lower than the current upper limit ($r < 0.032$).

We summarize impact of the pointing calibration to the optical depth and the primordial gravitational waves in Table 8.2.

Table 8.2: Systematic uncertainties of the pointing and polarization angle calibration to the optical depth and the primordial gravitational waves.

Calibration	optical depth "τ"	Primordial gravitational waves "r"
Pointing	$\sim 1\%$	$r = 0.0005$ ($\ell = 100$)
Polarization angle	$\sim 1\%$	$r = 0.001$ ($\ell = 100$)

8.2 Polarization angle

For the polarization angle calibration, we set the requirement of 0.43° to suppress its impact to a sufficiently small level for the B-modes measurement. It causes sufficiently small leakage from E-modes, which is one order magnitude lower than the primordial B-modes ($r = 0.03$) at multipole (ℓ) of 100. In this thesis, we calibrated the polarization angle by using the calibrated pointing information. We achieved the uncertainty of 0.27° under the assumption each antenna alignment is consistent with the design. This is lower than our requirement.

As described in section 6.1, mis-calibration of the polarization angle ($\delta\Psi$) introduces mixing between E-modes and B-modes. It is written as follows,

$$\begin{cases} C_{\ell,\mathrm{mis}}^{EE} = C_\ell^{EE}\cos^2(2\delta\Psi) + C_\ell^{BB}\sin^2(2\delta\Psi), & \text{(8.2a)} \\ C_{\ell,\mathrm{mis}}^{BB} = C_\ell^{BB}\cos^2(2\delta\Psi) + C_\ell^{EE}\sin^2(2\delta\Psi), & \text{(8.2b)} \end{cases}$$

where $C_{\ell,\mathrm{mis}}^{EE}$ and $C_{\ell,\mathrm{mis}}^{BB}$ are power spectra when we mis-calibrate the polarization angle by $\delta\Psi$, C_ℓ^{EE} and C_ℓ^{BB} are power spectra without the mis-calibration. Because $C_\ell^{BB} \ll C_\ell^{EE}$ and $\sin^2(2\delta\Psi) \ll \cos^2(2\delta\Psi)$, these equations are approximated as follows,

$$\begin{cases} C_{\ell,\mathrm{mis}}^{EE} \sim C_\ell^{EE}\cos^2(2\delta\Psi), & \text{(8.3a)} \\ C_{\ell,\mathrm{mis}}^{BB} \sim C_\ell^{BB} + C_\ell^{EE}\sin^2(2\delta\Psi), & \text{(8.3b)} \end{cases}$$

Based on these relations, we evaluate the systematic uncertainties of the EE and BB power spectra as shown in Figure 8.3.

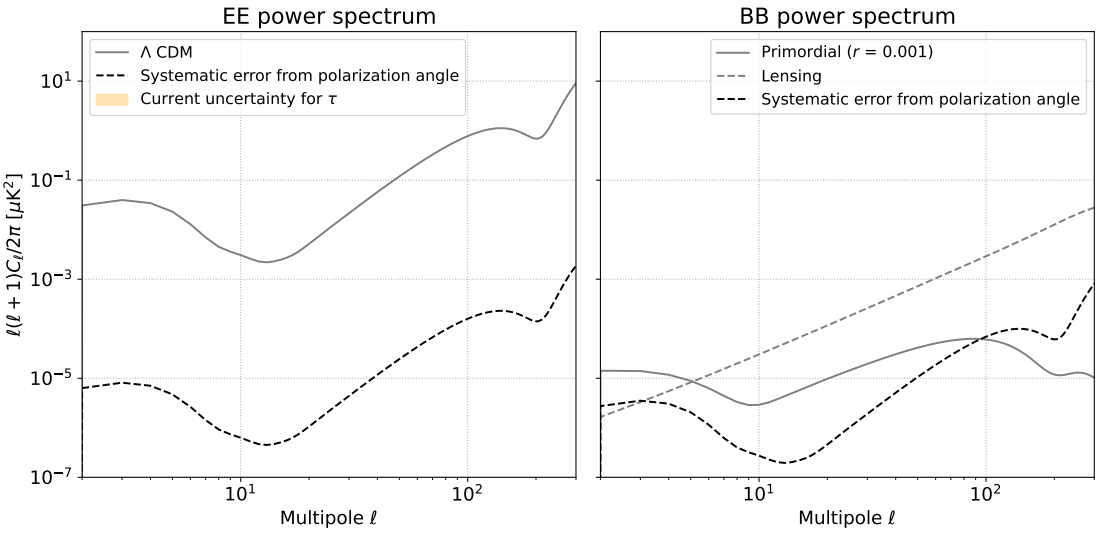

Figure 8.3: Systematic uncertainties of the EE and BB power spectra from the polarization angle calibration. We also plot the theoretical power spectrum (gray line) based on the best-fit values determined by Planck in the EE power spectrum. The systematic uncertainty of EE is four orders of magnitude smaller than the CMB power spectrum. It is two orders of magnitude smaller than the current uncertainty for τ based on $C_\ell^{EE} \propto \tau^2$. For the BB power spectrum, we also plot the primordial BB of $r = 0.001$ (gray line) and the lensing BB (gray dashed line). The systematic uncertainty of BB corresponds to the level of the primordial BB of $r = 0.001$ at its peak ($\ell \sim 100$).

Optical depth The uncertainty of the EE power spectrum is approximately four orders of magnitude lower than the EE power spectrum from ΛCDM. Therefore, the systematic uncertainty from the polarization angle calibration introduces 1% uncertainty to the optical depth. This is one order of magnitude lower than the current uncertainty [44].

Primordial gravitation waves Around the peak of the primordial BB power spectrum, the uncertainty from the polarization angle calibration corresponds to the primordial BB power spectrum of $r = 0.001$. This is 1/30 of the current upper limit ($r < 0.032$).

We summarize impact of the polarization angle calibration to the optical depth and the primordial gravitational waves in Table 8.2.

8.3 Noise study

In this study, we suppressed the noise by adopting three filter processes. The knee frequency of the 1/f noise is above the scanning frequency (0.17 Hz) and the scan synchronous still remained. We need to develop additional filtering which maintains high transfer function whereas suppressing them sufficiently. This is a future work. We give future prospects for science observations under the assumption that TOD includes only white noise in section 8.4.

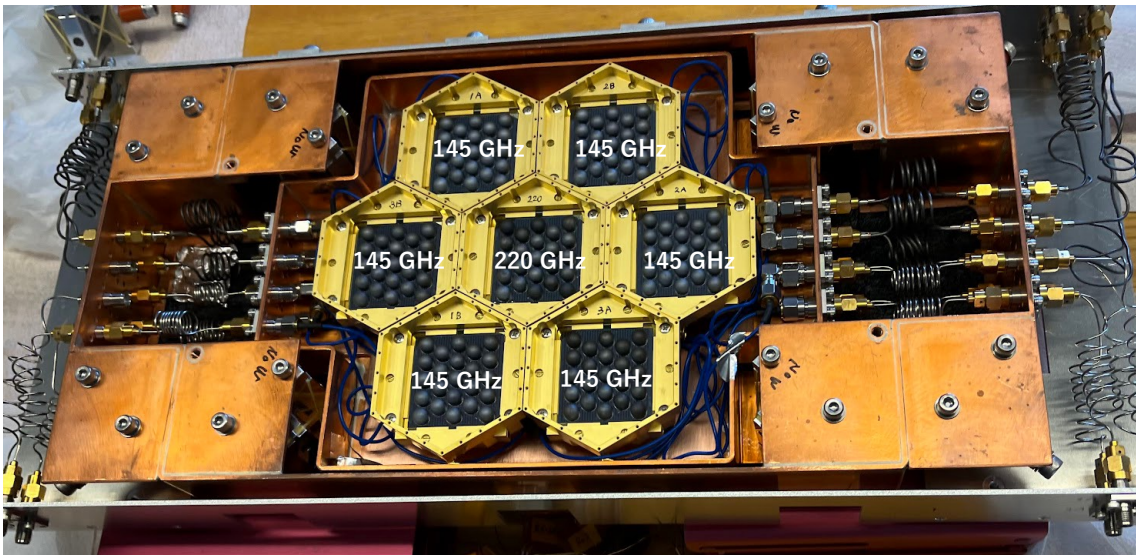

Figure 8.4: Photo of the focal plane with full arrays. There are 6 arrays and 1 array for the frequency bands of 145 GHz and 220 GHz, respectively. Each wafer has 23 MKIDs with Si lenslets.

8.4 Future prospects

In this thesis, we used the one detector array for the commissioning observations. We successfully installed the seven detector arrays for science observations in May 2023. Figure 8.4 shows the seven detector arrays installed in the focal plane. Six arrays of them are for the frequency band of 145 GHz. One array of them is for the frequency band of 220 GHz. We read out these arrays with the flexible cables which were tested in the commissioning observations. The new detectors were optimized based on knowledge from the commissioning data.

The design of 145 GHz array is almost the same as that used in this thesis. The main different point is the number of antenna orientations. As shown in Figure 8.5, we designed four types of antenna orientations. It allows us to reconstruct Q and U maps equivalently and to reduce the stripe noise as described in section 7.1.6. The 220 GHz array has the same configuration for the antenna orientation as 145 GHz band. We optimized the antenna geometry for 220 GHz band while we use the same Silicon lenslets for 220 GHz array. We performed Moon observation with full arrays. Their images are shown in Figure 8.6. We confirmed almost all detectors worked well. Our established calibration methods in this thesis can be applied to the new detectors too.

We have prospects to achieve the sensitivity of $\sim 20\%$ uncertaintiy using three years observation data with the QUIJOTE experiment [48]. Our forecast for the τ measurement is also based on the commissioning data. We expected the statistical uncertainty with the full arrays for three years when we assume sensitivity (NET $= 820\mu\mathrm{K} \cdot \sqrt{s}$) for 145 GHz band in Figure 8.7 [1]. This expectation is under the assumption that TOD has only white noise (i.e., we successfully reduce the 1/f noise and scan synchronous). For the measurement of the optical depth, we can achieve that the statistical uncertainty is lower than the EE power spectrum from ΛCDM. For searching for the primordial gravitational

[1] we assume the same 70% efficiency with respect to observation time as ref [48].

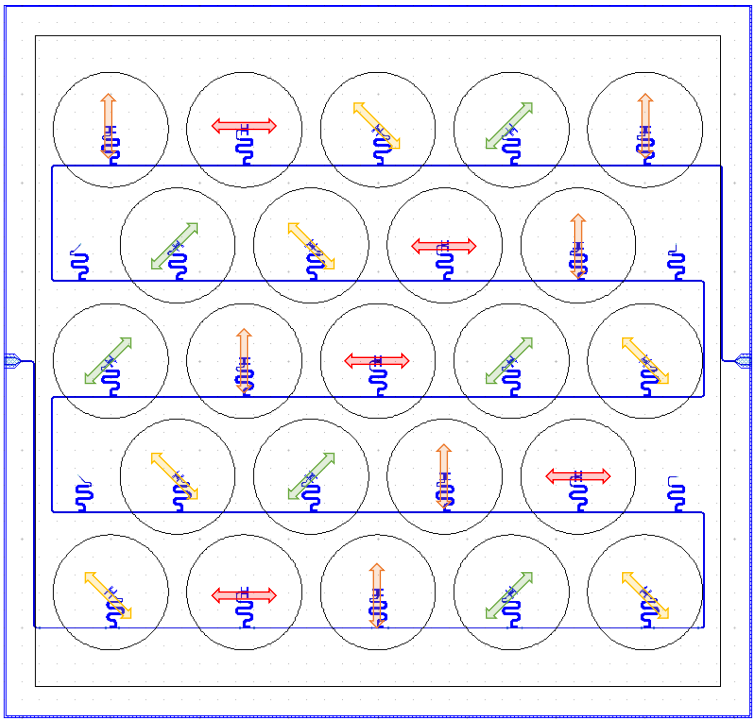

Figure 8.5: Detector wafer design of 145 GHz band for science observations. There are 27 MKIDs. 23 of them have antennas and Si lenslets to focus signals. 4 of them have neither the antenna nor the Si lenslet. They are used to check responses unrelated to incident photons.

waves, our statistical uncertainty is $r \sim 0.2$. These signal amplitudes could be reduced due to the filters. Development of the appropriate filters is a future work.

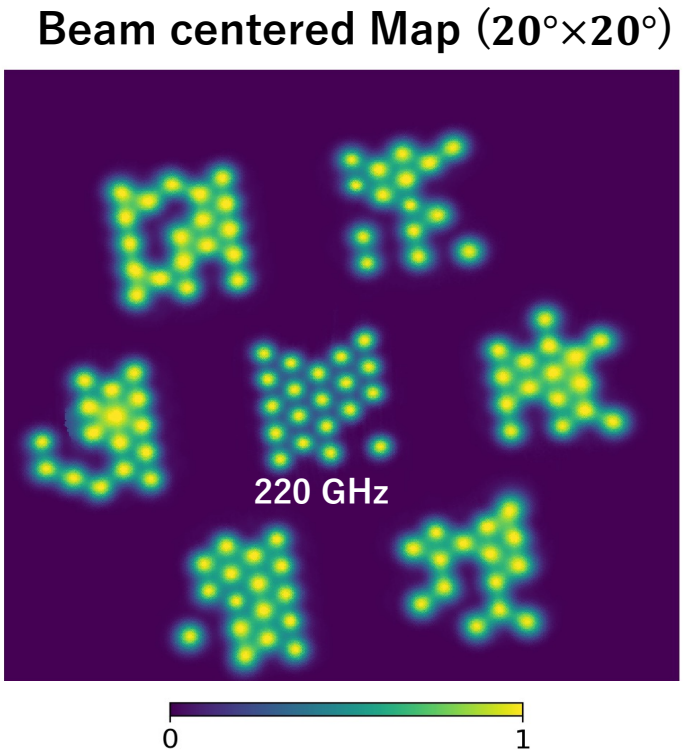

Figure 8.6: Moon images taken by full arrays in a beam-centered coordinate. In the beam-centered coordinate, pointing is invariable and the center of the coordinate is the boresight pointing of the telescope. The center images are taken by the detectors for 220 GHz band. Their Moon sizes were smaller than others (i.e. 145 GHz band) because the beam width of 220 GHz band is smaller than that of 145 GHz.

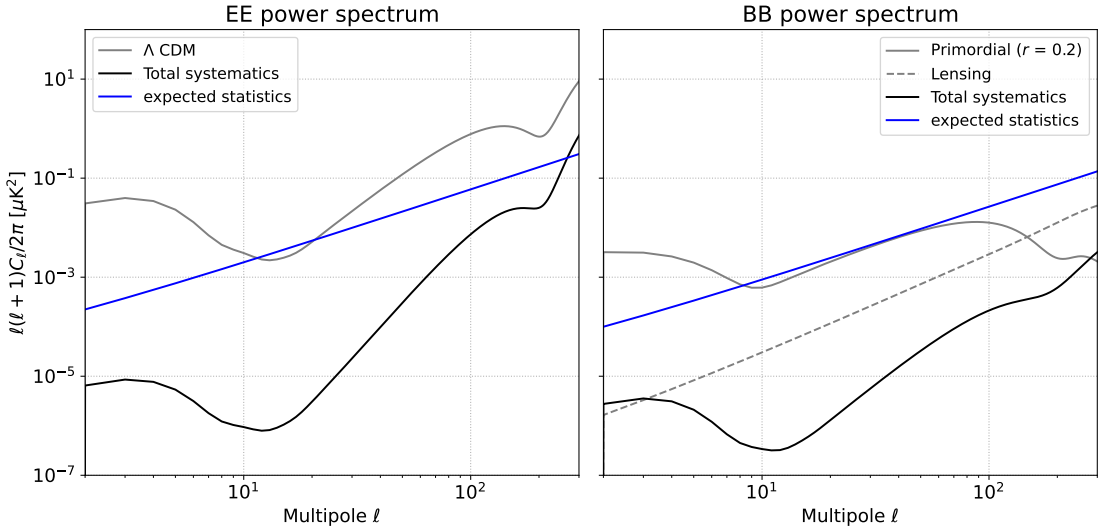

Figure 8.7: Expected statistical uncertainty with full arrays for three years. We considered the observation time efficiency of 70%. We assume that multipole bin widths of the EE and BB are 10 and 50, respectively. Here, we did not consider the foregrounds.

Chapter 9

Summary

CMB is a promising probe for understanding the history of the universe. Precise measurements of the anisotropy in the CMB polarization (E-modes and B-modes) at larger than degree-scale provide information about the primordial gravitational waves which are evidence for the cosmic inflation. The CMB polarization more than 10° scale also contains about the optical depth (τ) at the reionization era. The optical depth is important for determining the sum of the neutrino masses precisely. However, its measurement results have been systematically decreased. Its additional measurements are strongly suggested.

GroundBIRD experiment is a ground-based CMB experiment. The GroundBIRD telescope rotates continuously in the azimuth direction. The maximum speed of the azimuth rotation is 20 revolutions per minute. This rapid scan modulation mitigates effects of atmospheric fluctuation. These unique technology and unique scan strategy allow us to reach the large angular scale. We observe about 40% of the full sky area. Such an observation allows us to measure the primordial gravitational waves and the optical depth.

In the data analysis, we reconstruct the maps from time-ordered data (TOD) which are responses of each focal plane detector as a function of time. Information about the pointing and the polarization angle is necessary for the map making. The calibrations are important as the initial steps of the data analysis. The data contains various noises (e.g. the atmospheric fluctuation) as well as the CMB. To suppress the noise effects, we apply filters to TOD prior to the map making. The filter tends to smear the anisotropy of the CMB in general. It is important to develop good filtering methods which maintain efficiency for the CMB whereas significantly suppressing the noise effects. We developed calibration and filtering methods based on our commissioning observation data. The data was taken from February to April 2022. We used a prototype detector array at this moment.

We used the Moon observation data for the pointing calibration. Comparing to the planets such as Jupiter, frequent chance of observation every month with high signal-to-noise ratio is the biggest advantage of the Moon. However, we have not had sufficient knowledge about systematic uncertainties related to the Moon yet. In this thesis, we obtained knowledge about the systematic uncertainties in addition to the development of the calibration method. We model the pointing by considering the tilts of the telescope axes and the offsets. The optimized pointing model was obtained by using 345 Moon observation samples. We also evaluated systematic uncertainty related to the Moon. We

successfully achieved an uncertainty of $3.3'$, which is lower than our requirement ($4.7'$).

For the polarization angle calibration, we proposed the new calibration method based on the pointing information. We set the requirement of 0.43° to have a sufficiently small impact on the primordial gravitational waves (i.e. B-modes measurement). We obtained a rotation angle of the detector wafer from the calibrated pointing. Using this angle, we calibrate the polarization angles of each detector on the wafer. The achieved precision is 0.27°, which is lower than our requirement.

We developed the data analysis pipeline, and characterized the noise in real data. To suppress the noise effects, we adopted three processes: offset subtraction, common mode subtraction, and each scan filter. Using the analysis pipeline, we also evaluated the transfer functions for each process. We confirmed the offset subtraction did not reduce the transfer function. It only suppresses the noise. Then, we applied the common mode subtraction and the each scan filter. The noise power spectrum at lower multipole regions after applying these filters was approximately three orders of magnitude lower than that before applying the filters. The common mode subtraction reduced the transfer function around $\ell \sim 250$ by at most 14%. The each scan filter slightly reduced it; $\sim 2\%$. In total, we confirmed these processes maintain the transfer function ≥ 0.85 at $52 \leq \ell \leq 301$. Thus far we have not achieved sufficient noise suppression yet. Additional development for the filtering is necessary, which is future work.

Based on our calibration achievements, we evaluated impacts to our science targets by using the developed analysis pipeline. The achieved uncertainties of pointing and polarization angle correspond to 1% uncertainty for the optical depth. For the gravitational waves, the uncertainties of pointing and polarization angle correspond to 1/100 and 1/30 of the current upper limit of the tensor-to-scalar ratio ($r < 0.032$), respectively. We confirmed sufficient achievements for the pointing and the polarization angle calibrations.

In 2023 May, we upgraded our focal plane detectors, and started the scientific observations. The new detectors were optimized based on knowledge from the commissioning data. The new detectors consist of six arrays for the 145 GHz band and one array for the 220 GHz band. Each array has 23 detectors. We plan to observe the CMB for three years and to perform joint analysis for the optical depth with the QUIJOTE experiment. Our forecast for the τ measurement is also based on the commissioning data. In this thesis, we established the calibration methods which can be applied to the new detectors. We confirmed our prospects to achieve the sensitivity of $\sim 20\%$ uncertainty.

Appendix A

Two-Points Translation

As described in section 6.5, we used "Two-points translation" to convert the polarization angle in the horizontal coordinate system to that in the equatorial coordinate system. We used a distance of 10^{-4} degrees between the original point and additional point $(A_H^{'} - A_H)$. In this appendix, we describe how to validate and optimize this distance.

The further distance increases the uncertainty of the obtained translation angle (q). This is because the polarization angle is defined in the tangent plane while the point is represented in the spherical coordinate system. The shorter distance is better. On the other hand, too short a distance is affected by loss of digits. We used double-precision floating-point numbers. We optimized the distance with respect to these two aspects.

We validated two-points translation based on a simulation study. The concept of this simulation is shown in Figure A.1. We prepare an additional point $(rmP^{'})$ at the distance (d) very close to the original point (rmP) at first. We calculate vector $(\vec{X})$ between two points. Then, we rotate the two points by angles (θ). We calculate the vector $(\vec{X}')$ between two points after the rotation. We calculate translation angle $(\theta_{\rm two})$ by using both vectors $(\vec{X}, \vec{X}')$. This angle is an angle obtained from "two-points translation". Finally, we compare θ and $\theta_{\rm two}$ to validate its precision. Figure A.1 is the illustration in the case of 2 Dimensions. In real validation, we applied this validation to 3 Dimensions.

We performed this validation for distances from 10^{-9} degrees to 1 degree. we performed 100,000 validations for each distance with random original points and random rotation angles. Figure A.2 shows the validation result. The maximum angle difference $(\theta - \theta_{\rm two})$ in 100,000 validations as a function of the distance. Its relation was the same as expected due to the loss of digits and the projection effects. We found that 10^{-4} degrees achieved the lowest difference which is the level of 10^{-6} degrees. Based on this simulation, we decided to use the distance of 10^{-4} degrees and assigned the systematic uncertainty of 10^{-6} degrees.

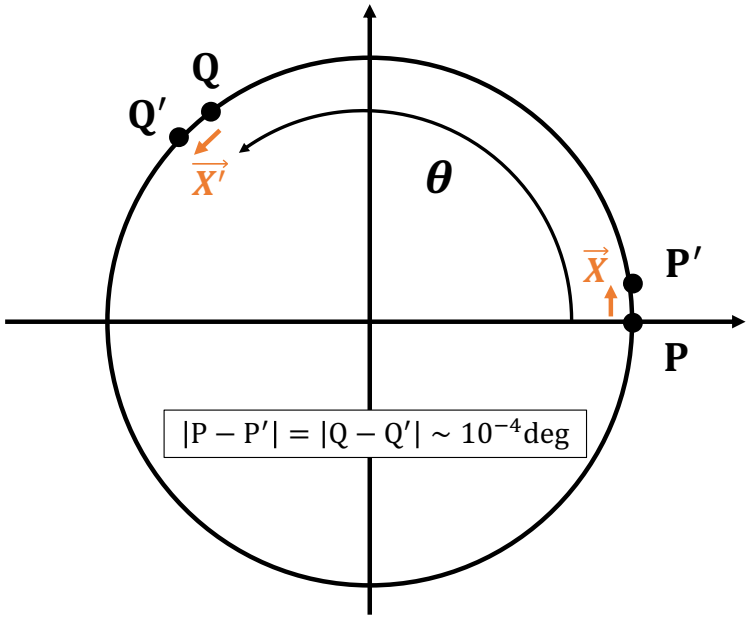

Figure A.1: Validation concept of "Two-points translation" in the case of 2 dimensions. We prepare additional point ($P^{'}$) at the distance (d) very close to the original point (rmP). We rotate them by an arbitrary rotation angle (θ). We calculate vector for each two points ($P, P^{'}$ and $Q, Q^{'}$). Then, we obtain translation angle (θ_{two}) by using these vectors ($\vec{X}, \vec{X'}$). This angle is an angle obtained from the two-points translation. To validate the two-points translation, we compare θ and θ_{two}. For real validation, we apply this procedure to 3 dimensions.

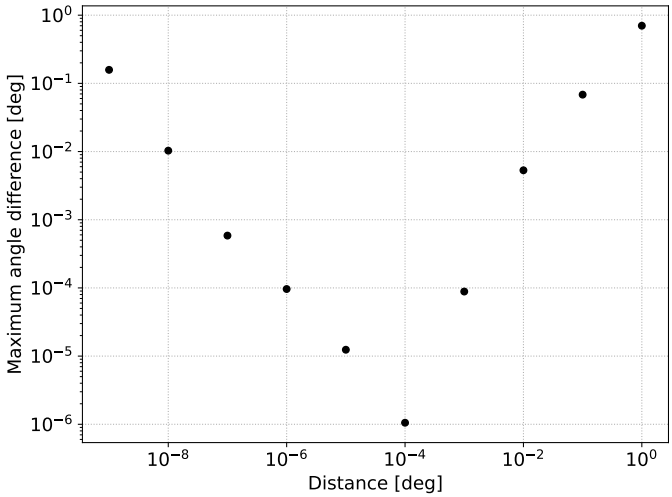

Figure A.2: Maximum angle difference as a function of the distance between the original point and additional point. The difference is increased when we take longer length at length $\geq 10^{-4}$ degree. This is because the polarization angle is defined in the tangent plane while the point is represented spherically. On the other hand, the difference is also increased when we take too short at length ($\leq 10^{-4}$ degree) because of a loss of digits.

Appendix B

TOD subtraction with timing offset

In section 7.1.4, we described the simulation study to validate the common mode noise in real data. In this thesis, we did not reconstruct CMB maps from a subtracted TOD which is the difference between two TODs taken by different detectors. The subtracted TOD ideally only includes the polarization signal. Thus, other CMB experiments reconstructed the CMB maps from the subtracted TOD. In this appendix, we describe a study about TOD subtraction as well as the common mode subtraction step by step. We also show further study for the subtraction method of TOD when we consider azimuth structure.

B.1 Case 1: Common mode noise only

First of all, we simulate TOD which includes the common mode noise only. We simulate two TODs ($y_1^{\rm sim} = y_2^{\rm sim} = y_{\rm com}^{\rm sim}$) by using the noise spectrum model (Eq. (7.3)). We assign the common mode noise ($y_{\rm com}^{\rm sim}$) with $\sigma_w = 400\ \mu{\rm K}\cdot\sqrt{s}$, $f_{\rm knee} = 5$ Hz, $\alpha = -1$. Figure B.1 shows a power spectrum density (PSD) of the common mode noise. We subtract $y_2^{\rm sim}$ from $y_1^{\rm sim}$ with two timing offsets ($\delta t = 50, 100$ ms) as follows,

$$y_d^{\rm sim}(t, \delta t) = y_1^{\rm sim}(t) - y_2^{\rm sim}(t + \delta t), \tag{B.1}$$

where $i = 1, 2$. Figure B.2 shows PSDs calculated from subtacted TODs ($y_d^{\rm sim}$) for $\delta t = 50, 100$ ms. Wave shapes of PSDs are synchronized to $1/\delta t$. This is the reason for making additional noise (wave shape) as described in section 7.1.4.

B.2 Case 2: Common mode noise + Individual noise

For the second case, we simulate TOD which includes the common mode noise and the individual noise. This situation is the same as section 7.1.4. We assign the indivisual noise ($y_{\rm ind}^{\rm sim}$) with $\sigma_w = 800\ \mu{\rm K}\cdot\sqrt{s}$, $f_{\rm knee} = 5$ Hz, $\alpha = -2$. The simulated TOD ($y_i^{\rm sim}$) is written as follows,

$$y_i^{\rm sim} = y_{\rm com}^{\rm sim} + y_{{\rm ind},i}^{\rm sim}. \tag{B.2}$$

Figure B.3 shows the PSD of $y_i^{\rm sim}$. Subtracted TODs ($y_d^{\rm sim}$) with $\delta t = 0, 50, 100$ are

calculated by using Eq. (B.1). We also applied Eq. (B.1) to real data. These PSDs are shown in Figure B.4, again. As described in 7.1.4, the wave shape at 1 Hz – 10 Hz in real data can be reproduced in the simulation. The wave periods corresponds to $1/\delta t = 20, 10$ Hz. This is the same as our expectation.

B.3 Case 3: Common mode noise + Individual noise + Azimuth structure

For more realistic simulation, we also consider azimuth structure. In this study, we model the azimuth structure as a triangle wave as shown in Figure B.5. We assume that it depends only on the azimuth (A) and is invariant in time. We assign 2 K amplitude to simulate the scan synchronous clearly. We simulate 20 TODs with collimation offset (dA_i) reflected in real scanning as follows,

$$y_i^{\rm sim}(A,t) = y_{{\rm az},i}^{\rm sim}(A + dA_i) + y_{\rm com}^{\rm sim} + y_{{\rm ind},i}^{\rm sim}, \tag{B.3}$$

where $i = 1 - 20$, $y_{{\rm az},i}^{\rm sim}(A)$ is azimuth strcuture. We used $dA_i = 3^\circ \times i$. 3° corresponds to the timing difference of 50 ms. Figure B.6 shows the PSD of the simulated TOD ($y_i^{\rm sim}$). We show PSDs from subtracted TODs ($y_d^{\rm sim}$) which is calculated by using two of 20 TODs with optimized timing offset (i.e., 50 ms) in Figure B.7 (a). There is the additional noise (wave shape) while we can reduce the scan synchorous. We also show the PSD calculated from the real data in Figure B.7 (a).

To avoid the additional noise, we subtract the average of TODs at first.

$$y_i^{\rm sim,ave}(A,t) = y_i^{\rm sim}(A,t) - \overline{y_i^{\rm sim}(A,t)}. \tag{B.4}$$

Then, we subtracte $y_2^{\rm sim,ave}(A,t)$ from $y_1^{\rm sim,ave}(A,t)$.

$$\begin{aligned} y_d^{\rm sim,ave}(t,\delta t) &= y_1^{\rm sim,ave}(A,t) - y_2^{\rm sim,ave}(A,t+\delta t), \\ &= y_1^{\rm sim}(A,t) - \overline{y_i^{\rm sim}(A,t)} - (y_2^{\rm sim}(A,t+\delta t) - \overline{y_i^{\rm sim}(A,t+\delta t)}). \end{aligned} \tag{B.5}$$

PSDs of $y_d^{\rm sim,ave}$ with the optimized timing offset as shown in Figure B.7 (b). We successfully reduced the wave shape in the real data as well as the simulation. On the

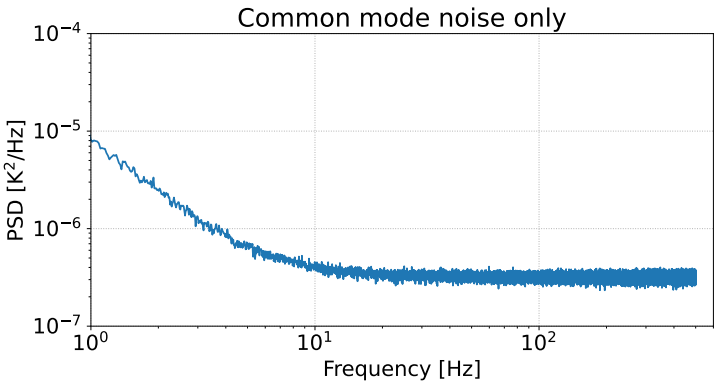

Figure B.1: PSD for the common mode noise TOD.

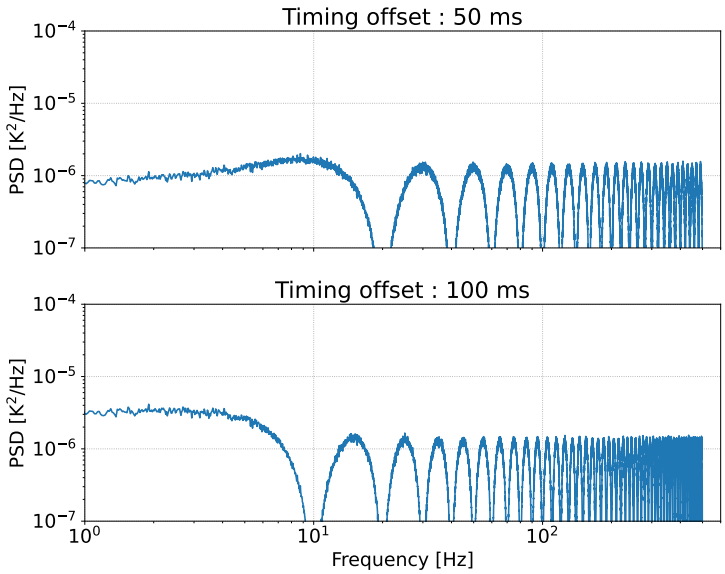

Figure B.2: PSDs calculated from subtracted TOD ($y_d^{\rm sim}$) with two timing offsets ($\delta t = 50, 100$ ms) in the case of the common mode noise only. There are wave shapes which are synchronized to frequencies ($1/\delta t = 20, 10$ Hz).

other hand, the scan synchronous happens again. Difference of average with timing offset ($\overline{y_d^{\rm sim}} = \overline{y_i^{\rm sim}(A,t)} - \overline{y_i^{\rm sim}(A,t+\delta t)}$) is the origin of it.

To suppress the scan synchronous to the same level of Figure B.7 (a), we add the running average of $\overline{y_d^{\rm sim}}$ to $y_d^{\rm sim,ave}$ in order to compensate for the scan synchronous. We define the running average of $y_d^{\rm sim}$ as average template. The running average leave low frequency component (e.g., scan synchorous and 1/f noise). Figure B.7 (c) shows PSDs after the common mode subtraction and the average template. In these PSDs, we successfully suppress the scan synchronous as well as the additional noise due to the common mode noise. These subtraction methods are useful for reconstructing the CMB maps from the subtracted TOD.

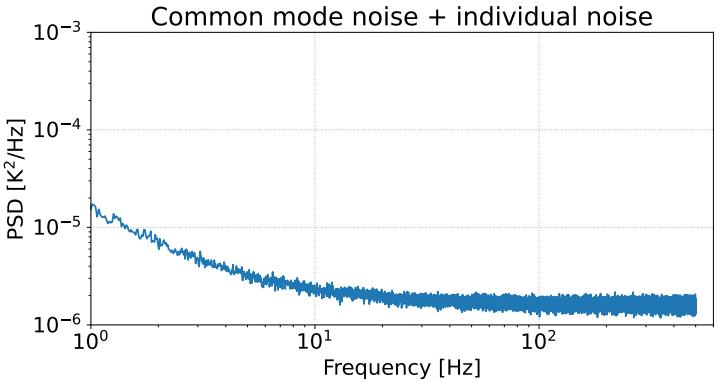

Figure B.3: PSD for the simulated TOD including the common mode noise and individual noise. We assign the individual noise level to be twice the common mode noise level. This PSD is dominated by the individual noise.

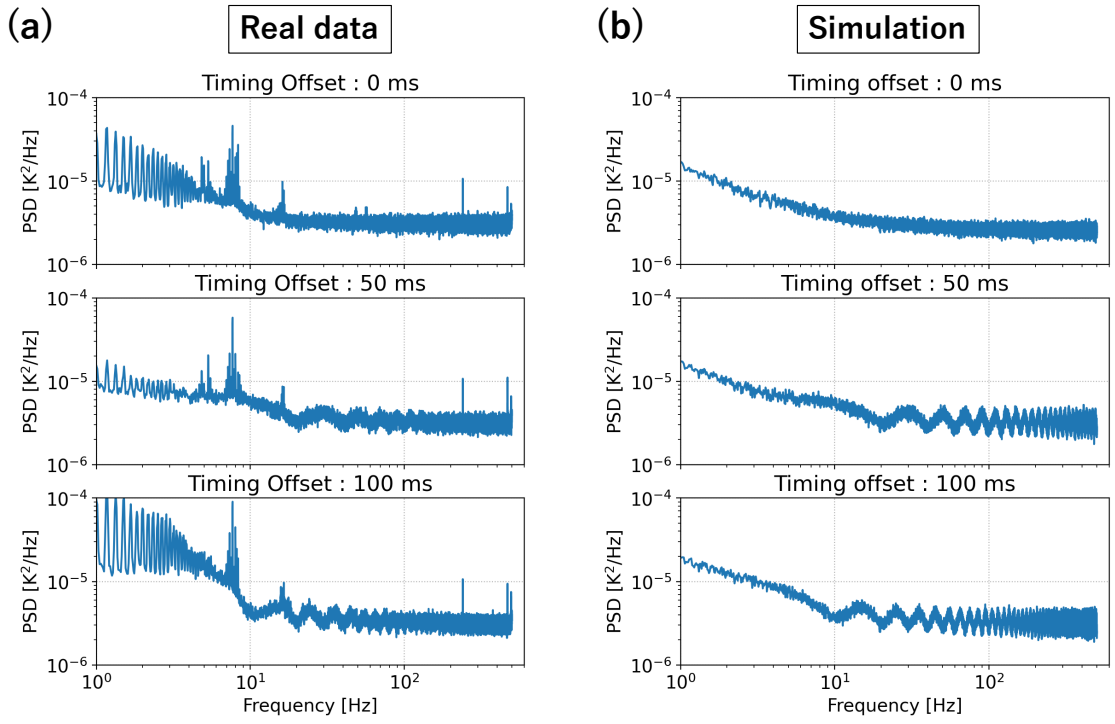

Figure B.4: PSDs comparison with three timing offsets to confirm the existence of the common mode noise. These are the same plots in section 7.1.4. (a) PSDs calculated from the subtracted TODs with timing offsets (0, 50, 100 ms) in real data analysis. (b) PSDs calculated from the subtracted TODs with timing offsets (0, 50, 100 ms) in the simulation. Both trends are the same. The wave periods corresponds to $1/\delta t = 20, 10$ Hz as expected.

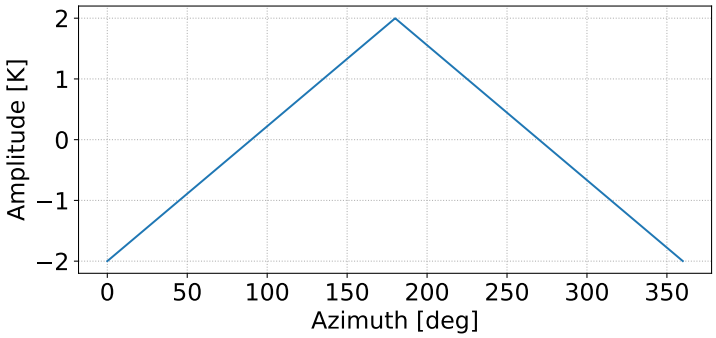

Figure B.5: Assumed azimuth structure in this study. Its amplitude is -2–2 K. It depends on only the azimuth direction and is invariant in time.

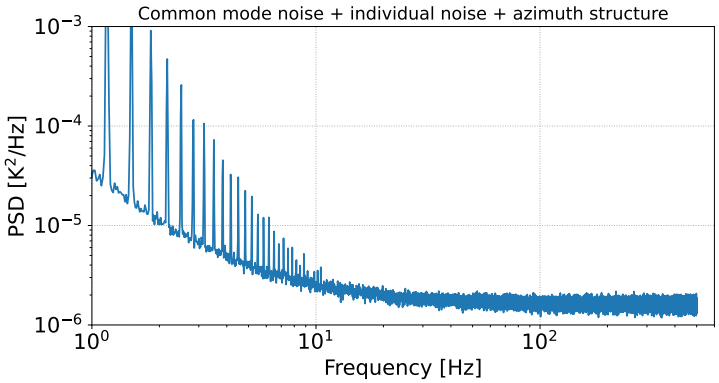

Figure B.6: PSD for the simulated TOD including the common mode noise, individual noise, and azimuth structure. The azimuth structure makes the scan synchronous at a lower frequency region.

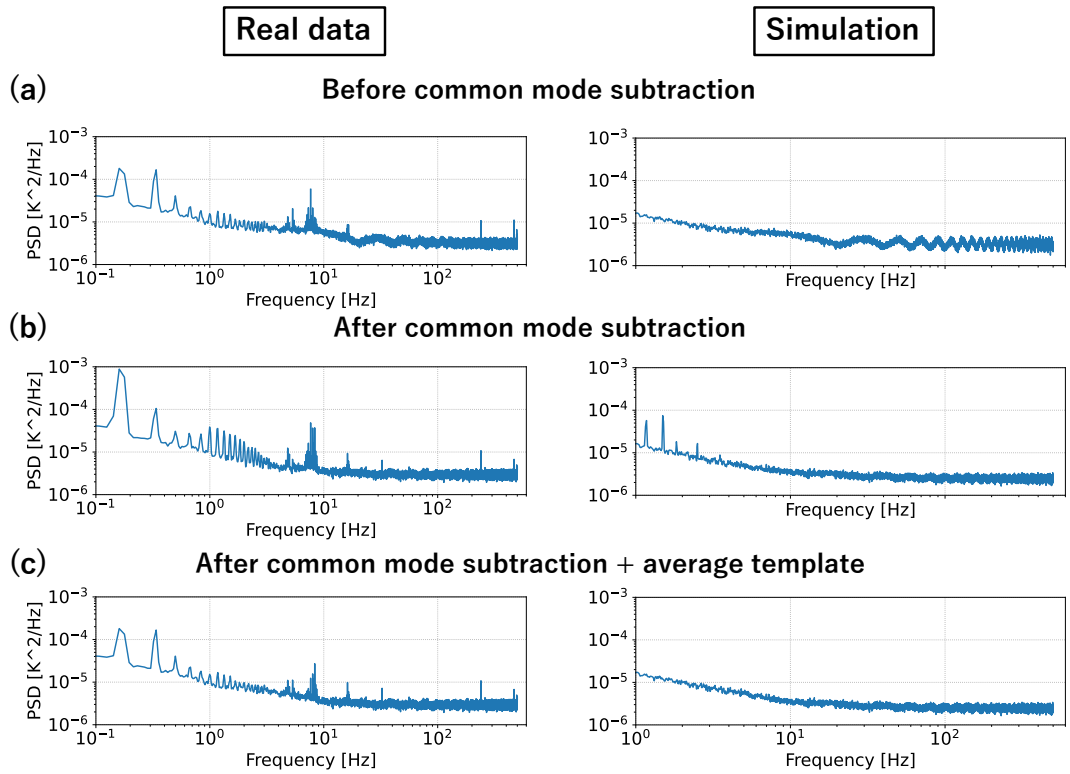

Figure B.7: Comparison of PSDs between real data and simulated data for each subtraction process. In these plots, we set the optimized timing offset (i.e., 50 ms). (a) Subtracted PSDs before the common mode subtraction. In real data, the azimuth structure changes in time. We cannot suppress the scan synchronous completely. (b) Subtracted PSDs after the common mode subtraction. We reduce the additional noise while the scan synchronous happens again. (c) Subtracted PSDs after the common mode subtraction and the average template. We successfully reduced the scan synchronous as well as the additional noise to the level of (a).

references

[1] Lemaitre, G., Publications du Laboratoire d'Astronomie et de Geodesie de l'Universite de Louvain, vol. 12, pp.D1-D19

[2] Edwin Hubble, Proc Natl Acad Sci U S A. 1929 Mar 15; 15(3): 168-173. https://doi.org/10.1073/pnas.15.3.168

[3] Wagoner, Robert V. ; Fowler, William A. ; Hoyle, F., Astrophysical Journal, vol. 148, p.3 (1967) https://doi.org/10.1086/149126

[4] Patrignani, C.; et al. (Particle Data Group) (2016).

[5] Penzias, A. A. ; Wilson, R. W., Astrophysical Journal, vol. 142, p.419-421 (1965)

[6] J. C. Mather et al 1999 ApJ 512 511, https://doi.org/10.1086/306805

[7] de Bernardis, P., Ade, P., Bock, J. et al. A flat Universe from high-resolution maps of the cosmic microwave background radiation. Nature 404, 955–959 (2000) https://doi.org/10.1038/35010035

[8] Planck Collaboration, A&A 641, A1 (2020), https://doi.org/10.1051/0004-6361/201833880

[9] QUIET Collaboration et al 2012 ApJ 760 145 https://doi.org/10.1088/0004-637X/760/2/145

[10] BICEP/Keck Collaboration, Phys. Rev. Lett. 127, 151301, https://doi.org/10.1103/PhysRevLett.127.151301

[11] The POLARBEAR Collaboration, et al., 2017 ApJ 848 121 https://doi.org/10.3847/1538-4357/aa8e9f

[12] Monthly Notices of the Royal Astronomical Society, Volume 519, Issue 3, March 2023, Pages 3383—3431 https://doi.org/10.1093/mnras/stac3439

[13] arXiv:2309.00675 [astro-ph.CO] https://doi.org/10.48550/arXiv.2309.00675

[14] J. T. Sayre et al. (SPTpol Collaboration), Phys. Rev. D 101, 122003, (2020) https://doi.org/10.1103/PhysRevD.101.122003

[15] Sigurd Naess, et al., JCAP10(2014)007 https://doi.org/10.1088/1475-7516/2014/10/007

[16] Howard Hui, et al., Proc. SPIE 10708, Millimeter, Submillimeter, and Far-Infrared Detectors and Instrumentation for Astronomy IX, 1070807 (9 July 2018) https://doi.org/10.1117/12.2311725

[17] Peter Ade, et al., JCAP02(2019)056 https://doi.org/10.1088/1475-7516/2019/02/056

[18] Kevork N. Abazajian, et al., arXiv:1610.02743 [astro-ph.CO] https://doi.org/10.48550/arXiv.1610.02743

[19] Hazumi, M., Ade, P.A.R., Akiba, Y. et al. LiteBIRD: A Satellite for the Studies of B-Mode Polarization and Inflation from Cosmic Background Radiation Detection. J Low Temp Phys 194, 443–452 (2019) https://doi.org/10.1007/s10909-019-02150-5

[20] Antony Lewis et al 2000 ApJ 538 473, https://doi.org/10.1086/309179

[21] Planck Collaboration, A&A 641, A6 (2020), https://doi.org/10.1051/0004-6361/201833910

[22] Y. Sueno, Master thesis, Kyoto University (2021).

[23] W. Hu and M. White, New Astron, 2:323–344, October 1997. https://doi.org/10.1016/S1384-1076%2897%2900022-5

[24] M. Kamionkowski, A. Kosowsky, and A. Stebbins Phys. Rev. Lett. 78, 2058 (1997) https://doi.org/10.1103/PhysRevLett.78.2058

[25] M. Zaldarriaga and U. Seljak, Phys. Rev. D 55, 1830 (1997) https://doi.org/10.1103/PhysRevD.55.1830

[26] A. A. Starobinsky, JETP Lett. 30, 682-685 (1979)

[27] R. Brout, F. Englert, E. Gunzig, Annals of Physics 115, 78 (1978) https://doi.org/10.1016/0003-4916(78)90176-8

[28] A. Staroninsky Phys. Lett. B 91, 990102 (1980) https://doi.org/10.1016/0370-2693(80)90670-X

[29] D. Kazanas, Astrophysical Journal, Part 2 - Letters to the Editor, vol. 241 (1980) https://doi.org/10.1086/183361

[30] K. Sato, Monthly Notices of the Royal Astronomical Society, 195, 467 (1981) https://doi.org/10.1093/mnras/195.3.467

[31] A. Guth, S. Pi, Phys. Rev. Lett, 49, 1110, (1982) https://doi.org/10.1103/PhysRevLett.49.1110

[32] A. Linde, Phys. Lett. B, 108, 389, (1982) https://doi.org/10.1016/0370-2693(82)91219-9

[33] A. Albrecht, P. Steinhardt, Phys. Rev. Lett. 48, 1220 (1982) https://doi.org/10.1103/PhysRevLett.48.1220

[34] R.L. Workman et al. (Particle Data Group), Prog. Theor. Exp. Phys. 2022, 083C01 (2022) and 2023 update

[35] G. Hinshaw, et al., 2013 ApJS 208 19, https://doi.org/10.1088/0067-0049/208/2/19

[36] Keck Array and bicep2 Collaborations, Phys. Rev. Lett. 121, 221301, https://doi.org/10.1103/PhysRevLett.121.221301

[37] M. Tristram, et al., A&A 647, A128 (2021), https://doi.org/10.1051/0004-6361/202039585

[38] M. Tristram, et al., Phys. Rev. D 105, 083524, https://doi.org/10.1103/PhysRevD.105.083524

[39] Komatsu Eiichiro, New astronomy library # 6, "Cosmic Microwave Background Radiation"

[40] Byeonghee Yu, Robert Z. Knight, Blake D. Sherwin, Simone Ferraro, Lloyd Knox, and Marcel Schmittfull Phys. Rev. D 107, 123522 - Published 16 June 2023 https://doi.org/10.1103/PhysRevD.107.123522

[41] C. L. Bennett et al 2003 ApJS 148 1, https://doi.org/10.1086/377253

[42] Planck Collaboration, A&A 594, A13 (2016) https://doi.org/10.1051/0004-6361/201525830

[43] Planck Collaboration, A&A 596, A107 (2016) https://doi.org/10.1051/0004-6361/201628890

[44] Planck Collaboration, A&A 643, A42 (2020) https://doi.org/10.1051/0004-6361/202038073

[45] O. Tajima, J Choi, M. Hazumi, H. Ishitsuka, M Kawai, M. Yoshida, Proc. SPIE 8452, Millimeter, Submillimeter, and Far-Infrared Detectors and Instrumentation for Astronomy VI, 84521M (2012) https://doi.org/10.1117/12.925816

[46] R. Gualtieri, et al., Journal of Low Temperature Physics volume 193, pages1112–1121 (2018) https://doi.org/10.1007/s10909-018-2078-x

[47] Planck Collaboration, A&A 641, A4 (2020) https://doi.org/10.1051/0004-6361/201833881

[48] K. Lee et al 2021 ApJ 915 88 https://doi.org/10.3847/1538-4357/ac024b

[49] Y Sueno, et al., Progress of Theoretical and Experimental Physics, ptae011, https://doi.org/10.1093/ptep/ptae011

[50] Julio A. Castro-Almazán, Casiana Muñoz-Tuñón, Begoña García-Lorenzo, Gabriel Pérez-Jordán, Antonia M. Varela, and Ignacio Romero "Precipitable Water Vapour at the Canarian Observatories (Teide and Roque de los Muchachos) from routine GPS", Proc. SPIE 9910, Observatory Operations: Strategies, Processes, and Systems VI, 99100P (18 July 2016) https://doi.org/10.1117/12.2232646

[51] Zonca et al., (2019). healpy: equal area pixelization and spherical harmonics transforms for data on the sphere in Python. Journal of Open Source Software, 4(35), 1298, https://doi.org/10.21105/joss.01298

[52] K.M. Gorski, et al., arXiv:astro-ph/0409513 (2004) https://doi.org/10.48550/arXiv.astro-ph/0409513

[53] J. Komine, master thesis, Kyoto University (2019).

[54] J. Choi, et at., Rev. Sci. Instrum. 84, 114502 (2013) https://doi.org/10.1063/1.4827081

[55] J. Yonggil et al.,Vol. 62, Issue 20, pp. 5369-5378 (2023) https://doi.org/10.1364/AO.488636

[56] Y. Mizugutch, M. Akagawa, H. Yokoi, IEEE Antennas and Propagation Society International Symposium (1976) https://doi.org/10.1109/aps.1976.1147539

[57] C. Dragone, The Bell System Technical Journal (Volume: 57, Issue: 7, September 1978) https://doi.org/10.1002/j.1538-7305.1978.tb02171.x

[58] H. Tran, A. Lee, S. Hanany, M. Milligan, T. Renbarger, Appl Opt. 2008 Jan 10;47(2):103-9. https://doi.org/10.1364/ao.47.000103

[59] J. Choi, GroundBIRD: A Telescope for the Cosmic Microwave Background Polarization Measurement, ph.D thesis, Korea University (2015).

[60] S. Oguri, et al., Rev. Sci. Instrum. 84, 055116 (2013) https://doi.org/10.1063/1.4807750

[61] Y. Inoue, et al., "POLARBEAR-2: an instrument for CMB polarization measurements", Proc. SPIE 9914, Millimeter, Submillimeter, and Far-Infrared Detectors and Instrumentation for Astronomy VIII, 99141I (8 August 2016) https://doi.org/10.1117/12.2231961

[62] P. A. R. Ade et al 2015 ApJ 812 176 https://doi.org/10.1088/0004-637X/812/2/176

[63] P. K. Day, H. G. LeDuc, B. A. Mazin, A. Vayonakis, J. Zmuidzinas, Nature 425, 817–821 (2003) https://doi.org/10.1038/nature02037

[64] S. J. C. Yates, J. J. A. Baselmans, A. Endo, R. M. J. Janssen, L. Ferrari, P. Diener, A. M. Baryshev Appl. Phys. Lett. 99, 073505 (2011) https://doi.org/10.1063/1.3624846

[65] D. F. Filipovic, S. S. Gearhart, and G. M. Rebeiz, IEEE Trans. Microwave Theory Tech. 41, 1738 (1993). https://doi.org/10.1109/22.247919

[66] Proc. SPIE 11445, Ground-based and Airborne Telescopes VIII, 114457Q (13 December 2020) https://doi.org/10.1117/12.2560918

[67] H. Ishitsuka, M. Ikeno, S. Oguri, O. Tajima, N. Tomita, T. Uchida, Journal of Low Temperature Physics volume 184, pages424–430 (2016) https://doi.org/10.1007/s10909-015-1467-7

[68] J. Suzuki, H. Ishitsuka, K. Lee, S. Oguri, O. Tajima, N. Tomita, E. Won Journal of Low Temperature Physics volume 193, pages562—569 (2018) https://doi.org/10.1007/s10909-018-2033-x

[69] T. Ikemitsu, master thesis, Kyoto University (2020).

[70] R. Barends, et al., IEEE Transactions on Applied Superconductivity (Volume: 19, Issue: 3, June 2009) https://doi.org/10.1109/TASC.2009.2018086

[71] Y. Sueno, et al., Progress of Theoretical and Experimental Physics, Volume 2022, Issue 3, March 2022, https://doi.org/10.1093/ptep/ptac023

[72] IEEE Transactions on Microwave Theory and Techniques (Volume: 41, Issue: 10, October 1993) https://doi.org/10.1109/22.247919

[73] H. Kutsuma, Master thesis, Tohoku University.

[74] J. Gao, "The Physics of Superconducting Microwave Resonators", ph.D thesis, California Institute of Technology (2008)

[75] H. Kutsuma, M. Hattori, R. Koyano, S. Mima, S. Oguri, C. Otani, T. Taino, O. Tajima, Appl. Phys. Lett. 115, 032603 (2019) https://doi.org/10.1063/1.5110692

[76] Toshio Fukushima, Observation of The Universe < 2 > Radio Astronomy [Astronomy of The Series Modern] (2017)

[77] A&A 536, A102 (2011) https://doi.org/10.1051/0004-6361/201116947

[78] Fricke, W, et al., Veroeff. Astron. Rechen-Inst., Vol. 32, p. 1-106 (1988)

[79] C. Ma et al 1998 AJ 116 516 https://doi.org/10.1086/300408

[80] Arias, E. F.,Charlot, P., Feissel, M., and Lestrade, J.-F., A&A, 303, 604A (1995)

[81] D. Denis Tramonte, Using CMB, LSS and Galaxy Clusters as Cosmological Probes ph.D thesis, Instituto de Astrofisica de Canarias (2010).

[82] Jeong, H., Ahn, Y., Won, E. et al. Development of cloud monitoring system for cosmic microwave background observations. J. Korean Phys. Soc. 80, 88-93 (2022). https://doi.org/10.1007/s40042-021-00338-1

[83] E. Keihänen, et al., Monthly Notices of the Royal Astronomical Society, Volume 360, Issue 1, June 2005, Pages 390–400, https://doi.org/10.1111/j.1365-2966.2005.09055.x

[84] E. Keihänen, et al., A&A 510, A57 (2010), https://doi.org/10.1051/0004-6361/200912813

[85] Eric Hivon et al 2002 ApJ 567 2, https://doi.org/10.1086/338126

[86] David Alonso, et al., Monthly Notices of the Royal Astronomical Society, Volume 484, Issue 3, April 2019, Pages 4127–4151, https://doi.org/10.1093/mnras/stz093

[87] L. Page et al 2003 ApJS 148 39, https://doi.org/10.1086/377223

[88] The POLARBEAR Collaboration et al 2019 arXiv e-prints https://arxiv.org/abs/1910.02608

[89] C. Bischoff et al., ApJ 768 9 (2013) https://doi.org/10.1088/0004-637X/768/1/9

[90] p. Ade et al., [Planck Collaboration] A&A 571, A1 (2014) https://doi.org/10.1051/0004-6361/201321529

[91] R. Thomas et al., A&A 558, A33 (2013) https://doi.org/10.1051/0004-6361/201322068

[92] A. Price-Whelan et al., [The Astropy Collaboration] AJ 156 123 (2018) https://doi.org/10.3847/1538-3881/aabc4f

[93] The POLARBEAR Collaboration et al 2017 ApJ 848 121 https://doi.org/10.3847/1538-4357/aa8e9f

[94] Planck Collaboration, A&A 594, A26 (2016) https://doi.org/10.1051/0004-6361/201526914

[95] Z. Xu et al., ApJ 891 134 (2020) https://doi.org/10.3847/1538-4357/ab76c2

[96] QUIET Collaboration et al 2011 ApJ 741 111 https://doi.org/10.1088/0004-637X/741/2/111

[97] C. A. Bischoff, OBSERVING THE COSMIC MICROWAVE BACKGROUND POLARIZATION ANISOTROPY AT 40 GHZ WITH QUIET, ph.D thesis, The University of Chicago (2010).

[98] N. Nakai, M. Tsuboi, Y. Fukui, Observation of The Universe < 2 > Radio Astronomy [Astronomy of The Series Modern] (2020)

[99] J. Mangum, ALMA Memo Ser., 366 (2001) (available online at http://legacy.nrao.edu/alma/memos/html-memos/alma366/memo366.pdf)

[100] PyERFA:documents https://pyerfa.readthedocs.io/en/latest/api/erfa.moon98.html#erfa.moon98

[101] J. S. V. Lagerros, Astronomy and Astrophysics, v.332, p.1123-1132 (1998)

[102] J. P. Kaufman et al. Phys. Rev. D 89, 062006 (2014) https://doi.org/10.1103/PhysRevD.89.062006

[103] Yuki D. Takahashi, Denis Barkats, John O. Battle, Evan M. Bierman, James J. Bock, H. Cynthia Chiang, C. Darren Dowell, Eric F. Hivon, William L. Holzapfel, Viktor V. Hristov, William C. Jones, J. P. Kaufman, Brian G. Keating, John M. Kovac, Chao-Lin Kuo, Andrew E. Lange, Erik M. Leitch, Peter V. Mason, Tomotake Matsumura, Hien T. Nguyen, Nicolas Ponthieu, Graca M. Rocha, Ki Won Yoon, P. Ade, and L. Duband "CMB polarimetry with BICEP: instrument characterization, calibration, and performance", Proc. SPIE 7020, Millimeter and Submillimeter Detectors and Instrumentation for Astronomy IV, 70201D (19 July 2008) https://doi.org/10.1117/12.790306

[104] The Polarbear Collaboration: P. A. R. Ade et al 2014 ApJ 794 171 https://doi.org/10.1088/0004-637X/794/2/171

[105] D. Hanson et al. (SPTpol Collaboration), Phys. Rev. Lett. 111, 141301 https://doi.org/10.1103/PhysRevLett.111.141301

[106] A. Ritacco, et al., A&A 616, A35 (2018) https://doi.org/10.1051/0004-6361/201731551

[107] Tajima, O., Nguyen, H., Bischoff, C. et al. Novel Calibration System with Sparse Wires for CMB Polarization Receivers. J Low Temp Phys 167, 936–942 (2012) https://doi.org/10.1007/s10909-012-0545-3

[108] M. Murata, et al., arXiv:2309.02035 [astro-ph.IM] https://doi.org/10.48550/arXiv.2309.02035

[109] P. Diego-Palazuelos, et. al., Phys. Rev. Lett. 128, 091302 (2022) https://doi.org/10.1103/PhysRevLett.128.091302

[110] H. C. Chiang et al 2010 ApJ 711 1123 https://doi.org/10.1088/0004-637X/711/2/1123

[111] Y. Chinone, Measurement of Cosmic Microwave Background Polarization Power Spectra at 43 GHz with Q/U Imaging ExperimenT, ph.D thesis, The Tohoku University (2010).

[112] Patricio A. Gallardo, Jon Gudmundsson, Brian J. Koopman, Frederick T. Matsuda, Sara M. Simon, Aamir Ali, Sean Bryan, Yuji Chinone, Gabriele Coppi, Nicholas Cothard, Mark J. Devlin, Simon Dicker, Giulio Fabbian, Nicholas Galitzki, Charles A. Hill, Brian Keating, Akito Kusaka, Jacob Lashner, Adrian T. Lee , Michele Limon, Philip D. Mauskopf, Jeff McMahon, Federico Nati , Michael D. Niemack, John L. Orlowski-Scherer, Stephen C. Parshley, Giuseppe Puglisi, Christian L. Reichardt , Maria Salatino, Suzanne Staggs, Aritoki Suzuki, Eve M. Vavagiakis, Edward J. Wollack, Zhilei Xu, and Ningfeng Zhu "Systematic uncertainties in the Simons Observatory: optical effects and sensitivity considerations", Proc. SPIE 10708, Millimeter, Submillimeter, and Far-Infrared Detectors and Instrumentation for Astronomy IX, 107083Y (6 August 2018) https://doi.org/10.1117/12.2312971

List of Figures

List of Tables